

NASA TECHNICAL NOTE



NASA TN D-8320

NASA TN D-8320

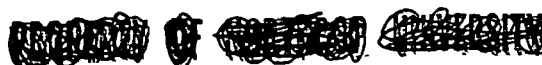
THERMAL PERFORMANCE OF AN INTEGRATED
THERMAL PROTECTION SYSTEM FOR LONG-TERM
STORAGE OF CRYOGENIC PROPELLANTS IN SPACE

Richard L. DeWitt and Robert J. Boyle

Lewis Research Center

Cleveland, Ohio 44135

NATIONAL AERONAUTICS AND SPACE ADMINISTRATION • WASHINGTON, D. C. • MAY 1977



1 Report No NASA TN D-8320		2 Government Accession No		3 Recipient's Catalog No	
4 Title and Subtitle THERMAL PERFORMANCE OF AN INTEGRATED THERMAL PROTECTION SYSTEM FOR LONG-TERM STORAGE OF CRYOGENIC PROPELLANTS IN SPACE				5 Report Date May 1977	
				6 Performing Organization Code	
7 Author(s) Richard L. DeWitt and Robert J. Boyle				8 Performing Organization Report No E-8881	
				10 Work Unit No 506-21	
9 Performing Organization Name and Address Lewis Research Center National Aeronautics and Space Administration Cleveland, Ohio 44135				11 Contract or Grant No	
				13 Type of Report and Period Covered Technical Note	
				14 Sponsoring Agency Code	
12 Sponsoring Agency Name and Address National Aeronautics and Space Administration Washington, D. C. 20546					
15 Supplementary Notes					
16 Abstract <p>It was demonstrated that cryogenic propellants can be stored unvented in space long enough to accomplish a Saturn orbiter mission after a 1200-day coast. The thermal design of a hydrogen-fluorine rocket stage was carried out and the hydrogen tank, its support structure, and thermal protection system were tested in a vacuum chamber. Heat transfer rates of approximately 23 W were measured in tests to simulate the near-Earth portion of the mission. Tests to simulate the majority of the time the vehicle would be in deep space and sun-oriented resulted in a heat transfer rate of 0.11 W.</p>					
17 Key Words (Suggested by Author(s)) Multilayer insulation, Shadow shields, Thermal protection; Space storage, Spacecraft models, Technology feasibility spacecraft Thermal vacuum tests, Liquid hydrogen, Cryogenic fluid storage; Thermal insulation				18 Distribution Statement Unclassified - unlimited STAR Category 18	
19 Security Classif (of this report) Unclassified		20 Security Classif (of this page) Unclassified		21 No of Pages 107	22 Price* A06

* For sale by the National Technical Information Service, Springfield, Virginia 22161

Page intentionally left blank

Page intentionally left blank

CONTENTS

	Page
SUMMARY	1
INTRODUCTION	2
MISSION REQUIREMENTS	3
VEHICLE DESIGN	3
THERMAL ANALYSIS	5
TEST PACKAGE AND TEMPERATURE CONDITIONING SHROUD	7
Test Tank	8
Fiberglass Struts	8
Tank-Mounted Insulation System	8
Shadow Shields	10
Vehicle Structure	10
Payload Simulator	11
Tank Pressurization Hardware	11
Shroud	12
Thermal Isolation of Test Tank	13
TEST FACILITY	14
INSTRUMENTATION	14
TEST CONDITIONS AND PROCEDURE	17
DATA REDUCTION	18
QBOILOFF	19
Energy Content Changes	20
QSTRUTS, QWIRES, QPLUMBING, QPINS, and QDUCT	21
QSEAM	22
QPEN. EFFECTS	23
CORRELATION OF EXPERIMENTAL RESULTS	24
Space Simulation Results	25
Near Earth tests	22
Heat transfer rate	25
Temperature comparisons	27
Deep Space tests	28
Temperature comparisons	28

Temperature differences across shadow shield sheet thickness	30
Heat transfer rate	30
Environmental Chamber Pressure Effects	31
Near Earth tests	31
Heat transfer rates	31
Temperature comparisons	32
Null tests	32
Deep Space tests	33
Temperature comparisons	33
Heat transfer rate	34
SUMMARY OF RESULTS	35
CONCLUDING REMARKS	36
APPENDIXES	
A - SYMBOLS	38
B - ICE BATH CONSIDERATIONS	40
C - DEVELOPMENT OF TUBULATION TEMPERATURE CORRECTION FOR IONIZATION GAGE READINGS	42
D - SHADOW SHIELD SMALL SCALE TEST RESULTS	45
REFERENCES	48

THERMAL PERFORMANCE OF AN INTEGRATED THERMAL PROTECTION SYSTEM FOR LONG-TERM STORAGE OF CRYOGENIC PROPELLANTS IN SPACE

by Richard L. DeWitt and Robert J. Boyle

Lewis Research Center

SUMMARY

To fully demonstrate the technology needed to design a long-term cryogenic storage system for a nonvented hydrogen fueled rocket stage, the following steps were accomplished: (1) a mission of 1200 days to the planet Saturn was considered as the propellant storage period prior to use of a hydrogen-fluorine vehicle during Saturn orbit, (2) a thermal design of the stage was completed, (3) the thermal behavior of the design was predicted during all phases of the mission, (4) the vehicle hydrogen tank, along with its support structure and thermal protection system were tested under realistic space conditions, and (5) the experimental thermal results were correlated with the analytical predictions to show that the analysis is of general utility and applicable to other stages typical of a general class of vehicles envisioned for future deep space mission applications.

The thermal protection system of the vehicle hydrogen tank consisted of multilayer insulation, shadow shields, an open truss structure, low conductivity tank supports, and low thermal conductivity electrical leads. The vehicle fuel tank, along with its support structure and thermal protection system, was tested in environments simulating both near Earth and deep space conditions. The bulk of the simulated deep space tests were conducted for a sun-oriented vehicle; however, an additional test for the vehicle without shadow shields was also accomplished.

The tests to simulate the near Earth phase of the mission had measured steady-state boiloff heat transfer rates increasing from 22.5 to 25.7 watts (76.9 to 87.6 Btu/hr). The initial test had the lowest heat transfer rate. For this test the heat transfer rate through the undisturbed multilayer insulation was 7.0 watts (23.9 Btu/hr). The heat transfer rate chargeable to disturbances to the multilayer insulation was almost twice the rate through the undisturbed multilayer. The disturbances resulted from insulation support pins, seams, and the penetration of the insulation by the tank supports.

Testing to simulate deep space coast conditions was conducted inside a shroud cooled to liquid hydrogen temperature. For the test simulating a sun-oriented vehicle the measured heat transfer rate was 0.11 watt (0.36 Btu/hr), which was lower than the allowable design heat transfer rate of 0.21 watt (0.7 Btu/hr). A simulated deep space test without the shadow shields yielded a heat transfer rate of 0.98 watt (3.33 Btu/hr).

For all test conditions the analysis was able to accurately predict the temperatures for the truss structure and the tank supports and gave fair agreement for the heat transfer rates.

INTRODUCTION

Certain future space missions, involving the placement of large payloads in geosynchronous Earth orbit, lunar orbit, or planetary orbit, require the use of chemical propulsion stages capable of providing sizable velocity increments after a long space coast. Such missions benefit greatly from the use of chemical propellants that provide high specific impulse, smooth combustion, and reliable ignition. Two bipropellant combinations that satisfy these requirements are the cryogenics hydrogen-oxygen and hydrogen-fluorine. However, passive storage of cryogenics in space for long periods of time has not been demonstrated and presents a significant technological challenge.

It has previously been demonstrated that multilayer insulation can provide the necessary thermal protection for cryogenic propellants for missions of relatively short duration. Reference 1 contains a summary of the results obtained by various investigators in the area of cryogenic thermal control, and many of the results are concerned with the performance of multilayer insulation. Reference 2 gives the results of tests of a reusable multilayer insulation system and discusses the historical trends for the performance of multilayer insulation. Reference 3 contains experimental results and an experimentally derived heat transfer correlation for multilayer insulation. For missions of very long duration, however, the allowable heat flux to the propellants becomes very low, and multilayer insulation alone would not be able to provide the necessary thermal protection. The results of reference 4 indicate that the effectiveness of multilayer insulation may decrease beyond a thickness of 5.1 centimeters (2.0 in.).

Even though multilayer insulation alone would not provide the necessary low heat transfer rates for long-term missions, an integrated thermal protection system is capable of satisfying the mission requirements. In addition to multilayer insulation the integrated thermal protection system would include sun-orientation of the vehicle, shadow shields, low conductivity tank supports, and low thermal conductivity electrical wires. References 5 and 6 contain an analytic and experimental evaluation of shadow shields. Reference 7 contains the results of an experimental and analytic investigation of the temperatures and heat transfer rates for the thermal protection of a small-scale propellant tank. The results included the interaction of shadow shields with a simplified support structure. However, no multilayer insulation was used.

The present effort was undertaken to demonstrate the effectiveness of an integrated thermal protection system to enable the long-term storage of liquid hydrogen in space. Hydrogen was chosen as the test fluid because it is the most difficult to store in space. The test results are reported herein and in references 8 and 9. Reference 8 covers the design, fabrication, and structural testing of the shadow shields. Reference 9 covers the overall performance and details of the design of the modularized, replaceable multilayer system. For missions of relatively short duration, shadow shields would not be needed and a modularized, replaceable insulation would have several attractive features.

The work reported herein was primarily concerned with demonstrating the technology needed to design a long-term cryogenic storage system for a hydrogen fueled stage. It was necessary to (1) select a difficult set of mission requirements; (2) perform a complete stage design; (3) perform a thermal analysis as given in reference 3 to predict the behavior of the designed stage during all phases of the mission as well as during imposed test conditions; (4) fabricate and test a full-scale cryogenic propellant tank and associated vehicle structure under realistic space simulation conditions; and (5) provide valid correlation between the experimental results and analytical prediction so that the analysis could be shown to be of general utility and applicable to other stages typical of a general class of vehicles envisioned for future deep space mission applications.

Measurements were recorded in U. S. customary units and have been converted to SI units. Both sets of values are given throughout the report.

MISSION REQUIREMENTS

Hydrogen-fluorine and hydrogen-oxygen are propellant candidates for missions to the outer planets which have high terminal energy requirements. The results of reference 10 show nominal trip times to Jupiter of 2 years and longer trip times to Saturn. Since the longer the trip time, the more severe the thermal constraint, a 1200-day Saturn orbiter mission was selected for design purposes.

In order to minimize fluid management problems the design was chosen so that the oxidizer tank would not be vented after liftoff and that the hydrogen tank would not be vented after ascent. The tanks would remain locked up until use at Saturn 1200 days after launch. Preliminary analysis indicated that the vehicle would have to be oriented towards the sun for almost the entire mission. The vehicle could be reoriented for short periods during the flight however, and would not have to be sun-oriented immediately after launch while in a near Earth coast phase.

VEHICLE DESIGN

The vehicle designed for the Saturn orbiter mission had a total propellant mass of 3218 kilograms (7095 lb). Either oxygen or fluorine had enough thermal capacitance to absorb the heat loads imposed during the early phase of the mission and would tend to lose heat when the vehicle was sun-oriented. Since the hydrogen absorbed heat during the entire mission, it presented a more difficult thermal management problem than either oxidizer. The fluorine-hydrogen propellant combination was chosen because the oxidizer to fuel weight ratio of this combination (10) is about double that of the oxidizer

to fuel weight ratio of oxygen-hydrogen propellant. This resulted in a relatively small hydrogen tank containing 293 kilograms (645 lb) of propellant. The storage of hydrogen is more difficult for the smaller tank since the tank surface area to volume ratio is greater.

In order to store the liquid hydrogen for 1200 days in space without venting or excessive pressure increase, a very low average heat transfer rate into the tank must be achieved. Calculations showed that if the hydrogen is maintained in thermodynamic equilibrium, so that there are no temperature gradients in the fluid, a heat transfer rate of 0.2 watt (0.7 Btu/hr) would result in a pressure rise of 34.7 N/cm^2 (50 psi) at the end of the 1200-day coast. To provide a margin of safety, the test configuration was designed for a heat transfer rate much less than this value to the hydrogen tank.

The heat transfer to or from the fluorine tank also had to be low. If it was too high, the fluorine, like the hydrogen, would experience excessive pressure buildup. However, if the heat transfer from the tank was excessive, the fluorine would freeze. Table I gives the allowable heat transfer rates to both the hydrogen and fluorine tanks when the vehicle is sun-oriented.

A diagram of the stage design is shown in figure 1. The thermal design extended from the payload to the engine mounting structure. During the design study the engine and the liquid hydrogen feedline were omitted from the analysis. It was assumed that the feedline could be effectively isolated thermally from the tank by using low conductivity piping. It was further assumed that any solar panels and/or antennas could also be thermally isolated from the propellant tanks through shielding similar to the shadow shields.

The thermal management of the stage was accomplished by using low emissivity shadow shields, high emissivity-low solar absorptance coatings and coverings, multilayer insulation, low thermal conductivity support members and low thermal conductivity electrical wires. The low emissivity shadow shields reflect to space a large fraction of the energy emitted from the payload surface; the open truss structure facilitates this process. The multilayer insulation is the prime means of thermal control for the near Earth phase of the flight and is also needed when the vehicle is not sun-oriented. For most of the flight the vehicle is sun-oriented and the shadow shields and multilayer insulation combine together to reduce the heat flux to the hydrogen tank. The shadow shields greatly reduce the heat flux incident on the insulation and consequently the heat transfer through the insulation is greatly reduced. The multilayer insulation also serves to compensate for any degradation in the emittance of the shadow shield surfaces. It is possible that the emittance of the external surfaces of the shadow shields would increase during the mission. Table II gives the heat transfer rate to the hydrogen tank for different shadow shield external emissivities with and without insulation. With insulation a much larger emittance degradation can be tolerated than without insulation. The external surface of the insulation was covered with a single layer of Beta cloth in order to

provide meteoroid protection for the tanks. The choice of a single layer of Beta cloth was based on work reported in reference 11 and using an interplanetary meteoroid flux model given in reference 12. The exterior of the Beta cloth as well as all of the structure had high emittance-low solar absorption surfaces. The purpose of this arrangement was to minimize the amount of solar energy absorbed when the vehicle was not sun-oriented.

The predicted temperature profiles for the shadow shield sheets and the outer layer of the hydrogen tank insulation when the vehicle is sun-oriented are shown in figure 2. Figures 3 and 4 give the predicted temperature profiles for the structure, with figure 3 being for the truss and figure 4 giving the temperatures of the fiberglass support struts for both the hydrogen and fluorine tanks. The engine end of the truss structure was maintained at 78 K (140° R) in order to satisfy minimum temperature requirements for the engine.

Other areas of prime concern during the vehicle design period were (1) plumbing, (2) instrumentation and control wiring, and (3) lightweight construction. All of the plumbing and sensors except the tank outflow line which would be needed on an actual flight vehicle were included in the design. The hydrogen tank that was tested incorporated this hardware even though some of it was not called upon to function during the experimental testing period. It was assumed that the outflow line could be thermally isolated from the propellant tank by use of low conductivity piping. The designs of all electrical leads on the vehicle were based on the use of manganin instead of copper wires. If copper were used, the heat transfer to the hydrogen tank through the wires alone could exceed the total allowable heat transfer rate. The vehicle incorporated lightweight-type construction.

THERMAL ANALYSIS

The solution of the analytic equations results in temperature distributions for the shadow shields, truss structure, tank support struts, and insulation. The temperature distributions were found by dividing the truss structure, tank support struts, shadow shield sheets and insulation into a series of nodes. Heat balances were taken for each of the nodes. Both radiation and solid conduction terms were included in the analysis. Even though testing was done in a vacuum chamber, the heat fluxes were so low that gaseous conduction was significant. Therefore gaseous conduction terms were included in the analysis of the test configuration.

The analysis used was presented in reference 7. This reference gives a detailed description of the analytic procedure as well as the solution of the equations. The radiation balances were calculated assuming gray-diffuse surfaces. Directional properties for the sheets of the shadow shields were not used in the analysis. The gaseous conduc-

tion heat transfer considered only heat transfer directly between nodes. This was done primarily in order to keep the numerical calculations tractable and was warranted because of the uncertainties in the accommodation coefficients and the pressure around the vehicle. The analysis in reference 7 did not include insulation on the propellant tank. This was accommodated in the present analysis by adding nonlinear conduction terms, based on the heat transfer correlation given in reference 3, between the outside of the insulation and the tank.

The analytic correlation for the heat transfer rate through the insulation was derived in reference 3. The equation was derived from experimental measurements of the heat transfer rate through unperforated multilayer insulation in the normal direction. This correlation is as follows:

$$q = \frac{C_S \bar{N}^{2.56} (T_0^2 - T_T^2)}{N_S} + \frac{C_R \epsilon_{sh}}{N_S} (T_0^{4.67} - T_T^{4.67}) + \frac{C_P P}{N_S} (T_0^{0.26} - T_T^{0.26}) \quad (1)$$

where $C_S = 8.95 \times 10^{-8}$, $C_R = 5.39 \times 10^{-10}$, and $C_P = 3.67 \times 10^2$; when T is in K, \bar{N} is in layers/cm, q is in W/m^2 , and P is in N/cm^2 ; or $C_S = 8.06 \times 10^{-10}$, $C_R = 1.10 \times 10^{-11}$, and $C_P = 1.33 \times 10^4$; when T is in $^{\circ}R$, \bar{N} is in layers/in., q is in $Btu/(hr)(ft^2)$, and P is in torr. (See appendix A for definition of the other symbols.) The first term on the right of equation (1) gives the heat transfer through the multilayer insulation due to conduction while the second term gives the heat transfer rate due to radiation. The last term gives the gaseous conduction heat transfer due to the presence of helium gas within the insulation. The assumption was made that the vacuum pressure measured outside the insulation was the pressure within the multilayer insulation.

The equations of the analytic model were solved using a finite difference thermal analyzer computer program (ref. 13). In this analysis the temperatures of the outer surface of the insulation, the truss structure, and the fiberglass tank supports are found simultaneously. These temperatures were determined from the temperatures of the payload, propellant tank, and surrounding environment. Since the temperatures are found from heat balances, the heat transfer rates are determined as a consequence of calculating the temperatures.

The independent variables used in the analysis are given in table III; part (a) of this table gives the physical dimensions used in the analysis, and part (b) gives the material and surface properties used in the analysis. These properties were obtained from the references 3 and 14 to 17. The low emissivity properties of the metalized surfaces were measured at room temperature with a Gier-Dunkle reflectometer. A linear temperature extrapolation of the low emissivity properties was made between room temperature and absolute zero. Emissivity of metalized surfaces probably does not vary linearly

with temperature. Reference 18 indicates that there is a temperature to the two-thirds power relationship. However, reference 7 indicates that the sheet temperatures are more sensitive to the probable uncertainty in the emissivity measurement (± 0.005) than to the particular temperature dependency chosen.

Analytic heat transfer predictions were made only for the heat transfer rates to the tank through the multilayer insulation blankets and via the tank support struts. The electrical and plumbing line heat transfer rates were determined only experimentally using thermocouple measurements and material properties. No comparisons were made with analytic predictions.

The analytic model for the test configuration differed only slightly from that used for the vehicle design. The experimental data showed the presence of contact resistances at three places between parts of the structure. Conductance values were then incorporated into the analytic model to account for the experimental temperature differences appearing across the resistances. The three conductance values used were: (1) between the payload ring and the payload simulator resulting from warpage of the ring and having a value determined from the assumption of radiant heat transfer between black surfaces; (2) between each shield ring and the structure with a value of 0.11 W/K ($0.20 \text{ Btu/(hr)}(^{\circ}\text{R})$); (3) between the tank and each of its supports with a value of 0.027 W/K ($0.052 \text{ Btu/(hr)}(^{\circ}\text{R})$).

TEST PACKAGE AND TEMPERATURE CONDITIONING SHROUD

The major subdivisions of the test package were the LH_2 tank supported by 12 fiberglass struts, a tank mounted blanket-type multilayer insulation system, two double sheeted shadow shields, two sections of vehicle structure, a payload simulator, and a constant temperature equipment box. Two major test series were conducted. The first series was performed with just the insulated tank; the second group was performed after the two double sheeted shadow shields had been added. The two configurations are shown in figures 5 and 6, respectively. For each series the test package was contained within a temperature controllable shroud located inside a vacuum chamber. The test package was thermally isolated from the facility.

Deviations from actual flightweight design were accepted early in the program with regard to the structure and the propellant tank. Specifically, to minimize costs, stainless steel in appropriate standard gages was used for the test vehicle structure in place of titanium which would have been on the order of 19 percent lighter. Also, provisions for bolting together the two major portions of the structure to allow for disassembly and reassembly of the test package at least once during the program, caused some weight increases. A large manhole was provided, with a significant increase in the propellant tank weight, to allow installation and possible repair of research instrumentation within

the tank. The resulting structure and tank were designed on the basis of flight loads for the minimum possible weight within the constraints imposed by the above factors. Additionally, and of vital importance, analyses established that the resulting test vehicle structure did provide a correct simulation for the flight module.

Test Tank

The LH₂ tank, shown in figure 7, was an approximate 1.2-to-1.0 oblate spheroid with an actual volume of 4.96 m³ (175.0 ft³). The major and minor diameters were 2.23 and 1.85 meters (87.6 in.) and (73.0 in.), respectively. The tank was constructed of 2219-T62 aluminum and had a working pressure of 55 N/cm² differential (80 psid). The tank hemispheres were first spin formed and then chemically milled to a membrane thickness of between 0.196 to 0.221 centimeter (0.077 to 0.087 in.). Weld lands were 0.457 centimeter (0.180 in.) thick. Support loads were introduced into the tank by support brackets welded to the lower hemisphere. A 0.46-meter- (18-in.-) diameter man-hole allowed access to the interior. Vent, pressurization, LH₂ fill, and LH₂ outflow valves were mounted on channel shaped brackets also welded directly to the lower hemisphere.

Fiberglass Struts

The LH₂ tank support struts consisted of filament-wound fiberglass tubes with integral titanium end fittings. The titanium end fittings had a threaded hole to accommodate spherical rod end bearings which served as the connection device to the tank brackets and the vehicle structure. The struts were 3.8 centimeters (1.5 in.) in diameter and had a minimum wall thickness of 0.076 centimeter (0.030 in.). A mixture of chopped aluminized Mylar and "Dexiglas" flakes were inserted into the strut tubes prior to installation of the rod end bearings. This mixture served to inhibit radiation heat transfer inside of the hollow strut. The exterior of each strut was sprayed with high emissivity 3M White Velvet paint. A photograph of a typical strut is shown in figure 8. Details of the structural design, the thermal design and analysis, and developmental testing of these struts are available in reference 16.

Tank-Mounted Insulation System

The basic insulation concept arrived at for the LH₂ tank is shown in figure 9. Two MLI blankets were used. Each blanket consisted of 15 double aluminized Mylar

(0.0064 mm, 0.25 mil) radiation shields alternately spaced between 16 double layers of silk net spacers (0.0015 g/cm², 0.048 oz/ft² per double layer), with two outer cover sheets of Schjeldahl X-850 reinforced aluminized Mylar (0.0078 g/cm², 0.256 oz/ft²). Each blanket was held together with nylon button-pins and retainers located on 20 centimeter (8 in.) centers. The button-pins and retainers were cemented to the cover sheets at their points of contact in an attempt to provide a positive means of layer density control for the insulation. In addition, where possible, the cover sheets, spacers, and radiation shields were formed to their required contour to further control the insulation density. Nominal insulation density based on the button pin to retainer dimension was 17.7 layers/cm (45 layers/in.).

Modularizing the insulation system in combination with the use of structural cover sheets resulted in an insulation system that was rugged, lightweight, and easily applied or removed. As shown in figure 10, the insulation is broken up into several elements including: 60° gore panels, upper polar cap, lower polar cap, fill line and fill line elbow cover, vent line cover, valve box cover, strut penetration covers, and gore section positioning pin covers. A combination of six positioning pins, mounted on the LH₂ tank wall, and Velcro hook-pile tapes were used to fasten each of the inner blanket gores to the tank. The outer blanket gores were then attached using the same two fastening techniques. The longitudinal joints between the gore segments of the inner and outer blankets were of a staggered butt design to minimize seam heat leaks.

Both the upper and lower insulation caps were in the form of truncated cones and were applied to fiberglass forms which, in turn, were attached to the LH₂ tank. Each cap consisted of two separate blankets held together by double length nylon button-pins and retainers. Velcro fastening tapes were the main method of attachment to the test tank and the fiberglass forms.

The fill line, fill line elbow, vent line, and valve box insulations were also composed of two separate blankets joined by double length button-pins and retainers. The valve box insulation was mounted over a fiberglass form. Offset butt joint design and hook and pile attachment tapes were applied in the same general fashion as for the upper and lower insulation caps.

The strut penetration covers and positioning pin circular covers consisted of five layers of double aluminized Mylar and silk net sandwiched between two Schjeldahl X-850 reinforced Mylar cover sheets. Both types of covers used Velcro for attachment to the outer gore blankets. A photograph of the tank, during the insulation addition period, is shown as figure 11.

The design mission also necessitated the use of a meteoroid shield. The shield, made of Beta cloth, covered the entire tank. The design contained gore sectors, upper and lower caps, and a valve box covering similar to the insulation design. It was attached to the insulation with Velcro hook mated to exposed Velcro pile on the insulation. In addition, a running stitch using Dacron thread was applied between the (1) gore sectors

and edge of the polar caps, (2) gore sector and line covers, and (3) line covers and valve box cover.

The MLI system applied to the LH₂ tank weighed approximately 23 kilograms (50.8 lb), 1.54 kg/m² (0.32 lb/ft²), including the fiberglass polar caps and valve box. The fiberglass components weighed 3.9 kilograms (8.6 lb).

A more complete and detailed description of the design, fabrication, and application of this MLI system is covered in reference 9.

Shadow Shields

The major element of the LH₂ tank deep space thermal protection system was a set of two double sheeted shadow shields. Figure 12 shows a double sheeted shadow shield. Figure 12(a) is an overall view of a completed unit; figure 12(b) details the sheet-to-rim connections as well as the structure strut penetrations. Each shield consisted of two sheets of Schjeldahl X-850 reinforced aluminized Mylar stretched over either side of a 2.95-meter (116-in.) inside diameter tubular aluminum frame (ring). The ring tubing was 3.8 centimeter (1.5 in.) diameter by 0.165 centimeter (0.065 in.) wall. Each circular sheet of a shield assembly was constructed of three separate pieces of Schjeldahl X-850 roll stock material. The separate pieces of material were butted side by side and the junction between the two adjoining pieces was bridged on both top and bottom surfaces by bonding on a continuous strip of Schjeldahl X-850 5.1 centimeters (2 in.) wide. In order to fasten the shield sheets around the tubular ring 36 support tabs were installed on each sheet. Mounting of the sheets was completed by connecting the tabs from opposing sheets over the outside surface of the tubular ring using wire clips which were bolt tensioned. Holes were cut in each sheet of each shield to allow passage of the vehicle structure struts. The attachment between the struts and the shadow shield ring was made via a leaf-spring type connection that allowed for the difference between the thermal contraction of the stainless steel vehicle support struts and the aluminum ring.

Complete details of the structural design, the thermal design and analyses, and developmental testing of these shadow shields are available in reference 8.

Vehicle Structure

The structure was an open truss type and had two natural divisions designated as (1) the forward structure and (2) the midstructure. A photograph of these sections is shown in figure 13.

The forward structure consisted of a circular payload support ring connected to

12 struts which were joined at six equally spaced points on the ring. The forward struts were designed for flight load conditions while the support ring was designed for handling purposes during testing. For a flight vehicle this ring could be lightened. Eighteen discretely spaced Schjeldahl X-850 circular shields were installed concentrically inside each of the forward struts. These disks served to inhibit radiation heat transfer inside the hollow strut from the payload simulator to the midstructure support ring.

The midstructure consisted of a hexagonal frame (midstructure support ring) which supported the fuel tank at six node points. Twelve midstructure struts also join at these six points. The struts were sized for flight loading conditions while the hexagonal frame member thickness was the minimum gage available without special mill runs. As a result the thickness of the frame member was about twice that required from a stress consideration.

As part of the thermal management of the test vehicle, the exterior of both sections of the vehicle structure was sprayed with high emissivity 3M White Velvet paint.

Payload Simulator

The vehicle payload was only simulated thermally and contained no vehicle flow subsystems or electronics superfluous to the immediate testing. The payload simulator was a 3.0-meter- (10-ft-) diameter, 0.64-centimeter- (1/4-in. -) thick, aluminum plate bolted directly to the forward structure payload ring. The bottom surface of the simulator, the side facing the propellant tank, was polished to an emissivity of 0.076. On the back or topside of the simulator, 2.5-centimeter- (1-in. -) inside diameter D-shaped LH₂ flow tubes (see fig. 14) were welded on to enable cooling of the simulator to 22 K (40 °R). In addition, electrical resistance heater strips (not shown in fig. 14) were adhesively bonded between the LH₂ flow tubes to allow heating of the simulator to room temperature.

Tank Pressurization Hardware

Gaseous helium was chosen as the pneumatic valve operator fluid and propellant tank pressurant for this test package. In order to simulate an actual flight vehicle more completely, a pressurization system requiring gas regulators, flow control orifices, shutoff valves, and pressure switches was designed and installed as part of the test package. This system remained passive during all thermal tests and was used only to slowly pressurize the propellant tank during expulsion of LH₂ at the end of a test series.

All helium flow control equipment was housed in a small insulated box, referred to as the equipment box, of approximately 0.08 cubic meter (2.83 ft³) mounted on top of the

payload simulator (fig. 15). The four pressure switches used were mounted on an unheated plate (referred to in fig. 5 as the pressure switch plate) tied to two of the struts of the midstructure.

Shroud

In order to simulate the thermal environment of space vacuum a high absorptivity shroud was used (see fig. 16). For tests simulating deep space and a sun-oriented payload the shroud was maintained at 22 K (40° R); for all other testing it was maintained at 294 K (530° R).

The shroud was nominally 4.0 meters (13 ft) high and approximately 4.0 meters (13 ft) in diameter. The vertical body of the shroud was composed of 12 panels with vertical D-shaped LH₂ flow tubes of 2.5 centimeter (1 in.) inside diameter welded on the outside surfaces. One of the vertical panels was a door which allowed access to the shroud interior to facilitate repair of any test configuration malfunctions. Both the bottom and the top of the shroud were flat and also had LH₂ flow tubes mounted on their exterior surfaces. The fourth major part of the shroud assembly was a group of three annular baffles. These units, also capable of being cooled with LH₂, were mounted inside the shroud coplanar with the payload simulator and the two shadow shields (see fig. 6) during testing. They served to prevent the majority of energy reflected from the shadow shields and the upper shroud wall from reaching the insulated LH₂ tank. The basic construction of all shroud surfaces was 0.32-centimeter- (1/8-in. -) thick aluminum plate. Each major section of the shroud (i. e., vertical walls, bottom, top, and baffles) had resistance heaters adhesively bonded between the LH₂ flow tubes to allow heating of the surfaces to room temperature. To improve the absorptivity of the shroud, the inside surfaces of the walls, the bottom, and the top, as well as the topside surfaces of each baffle, had a covering of 0.95 centimeter (3/8 in.) hexagonal honeycomb which was 0.95 centimeter (3/8 in.) thick. These honeycomb surfaces were sprayed with 3M Black Velvet paint. The honeycomb on the shroud bottom, as well as on the shroud walls below the baffles, helped absorb the residual energy escaping from the baffled volume as well as the energy radiated from the bottom sheet of the lower shadow shield.

Each major section of the shroud was commonly connected to a pressurized circular ring LH₂ manifold located at the base of the vertical walls. Each section, however, had an independent vent line containing a two position flow control valve. During low temperature operation, the control circuits of these valves were regulated by the output of platinum resistance temperature sensors located in the hydrogen lines between the valves and the surfaces being cooled. In order to reduce radiant heat transfer from the chamber to the shroud, and ultimately the amount of LH₂ used during cryogenic operations, a single layer of double aluminized Mylar was draped around all exterior sur-

faces of the shroud (see fig. 17).

Thermal Isolation of Test Tank

All the plumbing and electrical wiring required for the test vehicle can be divided into one of two distinct groups.

The first group consists of those flow lines and electrical wires needed as part of the vehicle itself. These lines and wires ran from the payload simulator to the LH_2 tank valve box via the pressure switch plate. Any heat transferred along these lines and wires was attributed to the way the vehicle was designed and was considered as part of the expected flight heat loading of the propellant tank.

The second group of lines and wires consisted of those needed for tank flow operations, test instrumentation, and control purposes. This group would not be necessary on a flight vehicle but was, however, needed for testing operations and collection of data. The test vehicle was designed so that these operations flow lines, the instrument wires from temperature transducers in the tank and insulation, as well as the control wires from shutoff valves were all brought out from the same location on the tank. A pronounced effort was made to (1) limit the number and size of the control and instrument wires as well as (2) to use materials having minimum values of thermal conductivity. After leaving the tank this second group of lines and wires passed through an enclosed duct up to a second LH_2 tank, called a cold guard tank, located immediately outside the wall of the shroud (see fig. 17). All plumbing lines were sloped slightly upward from the test tank to the guard tank to help inhibit the transfer of heat back to the test tank via convection currents inside the lines. The guard tank was 0.46 meter (1.5 ft) in diameter and 1.4 meters (4.6 ft) high. When filled, it contained ≈ 0.23 cubic meter ($\approx 8.1 \text{ ft}^3$) of hydrogen. It was kept filled with LH_2 during all thermal testing of the vehicle. All plumbing lines passed directly through this tank, and, as a result, were completely submerged in LH_2 for at least 1.2 meters (4 ft) of their length. Temperature conditioning of the instrumentation and control wires was obtained by adhesively bonding them onto the outside of the guard tank for a length of approximately 1.5 meters (5 ft). In addition, in all the nonthermocouple circuits, manganin wires were used instead of copper wires between the cold guard and the test tank. The greater electrical resistance of the manganin requires the use of larger diameter wires to avoid incurring an excessive voltage drop in the lines; however, the reduced thermal conductivity of manganin more than offset the effect of wire diameter. During all steady state test periods, any unnecessary current carrying circuits to the insulated LH_2 tank were physically interrupted to prevent any resistance heating loads in these manganin lead lines.

TEST FACILITY

All thermal testing of the vehicle was done in a 7.6-meter- (25-ft-) diameter spherical side loading vacuum chamber (see figs. 16 and 17). The entrance door to the chamber had a diameter of 6.1 meters (20 ft). The "clean-dry-empty" vacuum capability was approximately 1.1×10^{-4} N/m² (8×10^{-7} torr). Figure 18 is a general schematic of facility plumbing and control circuits required for this experimental program.

Liquid hydrogen had to be furnished to the insulated test tank, the cold guard tank, the shroud, and the payload simulator. Hydrogen flow through the simulator was controlled in the same manner as for the shroud (see the section entitled Shroud). Parallel flow paths in the vent lines of both the test tank and the cold guard allowed independent filling of these tanks. As a safety feature a burst disk was added to the LH₂ test tank. This item would not be on a flight version of the test package.

Electric power and control circuits were needed for the shroud, the payload simulator, and the equipment box. The shroud had four separate heater circuits (side walls, bottom, top, and baffles); the payload simulator had three separately controlled areas (a center circle and two annular rings); the equipment box was on a separate single circuit.

Several test periods were required at pressure levels higher than the chamber minimum vacuum. These vacuum levels were created by adjusting a controlled bleed of gaseous helium into the chamber outside of the shroud enclosure.

A major piece of equipment in the vent lines of both the test tank and the cold guard tank was the backpressure control valve and its associated control equipment. Figure 19 is a block diagram of the two parallel backpressure control circuits used during this test program. The critical components of the circuitry are the high resolution differential pressure transducers and the reference volume ice bath. The particular transducers employed were a high resolution capacitance type. These units sensed any differential pressure between the tank they were monitoring and a "constant" pressure held in a reference bottle located in the ice bath outside the environmental chamber. The output of each differential pressure transducer was electrically conditioned and used as an input signal to the controller of a valve in the vent line of each tank. An ice water bath was selected to house the reference volume bottle because this type of bath had the least temperature change for the range of barometric pressure values expected during testing. A detailed discussion of how the practical problems of servicing and maintaining the ice bath affected the backpressure control circuit appears in appendix B.

INSTRUMENTATION

One of the objectives of the instrumentation was to provide enough temperature data

so all heat transfer rates, as well as energy content changes of the insulation, tank, ullage, and liquid propellant could be determined. Another objective was to determine the mass rate of flow and energy level of the vent gases. In addition, steady state temperature data for the vehicle structure, tank mounted insulation system, and shadow shields were also needed (1) to allow verification of the analytical program which was used to predict thermal performance of the test hardware and (2) to determine the effectiveness of construction techniques used in the insulation fabrication.

Thermocouples and platinum resistance temperature sensors (PRTS) comprised the temperature transducers on the test configuration. As mentioned earlier, a pronounced effort was made to limit the number and size of wires leading to the test vehicle hardware as well as to employ wires having low values of thermal conductivity. As a result, the majority of the temperature transducers employed were chromel constantan thermocouples. These units each required only two leads whereas a platinum sensor required four. Figure 20 is a schematic of the instrumentation on the test package.

The use of PRTS on the test vehicle was confined to the tank interior, the tank wall, several locations on the fiberglass struts, two places on the midstructure, three places within the insulation blankets, the pressure switch plate, and on the payload simulator. The leads from the PRTS, except for the six transducers which were mounted on and thermally shorted to the payload simulator, all exited from the test configuration through the tank-to-cold guard duct. The leads were 0.51-millimeter- (20-mil-) diameter copper inboard of the tank valve box and outboard of the cold guard end of the duct. Inside the duct, jumper wires of 0.81-millimeter- (32-mil-) low thermal conductivity manganin were used to complete the circuitry. The majority of the PRTS used were spanned from 20 to 39 K (36° to 70° R). The probable error of the complete measurement channel was computed to be ± 0.2 K at 20 K ($\pm 0.36^{\circ}$ R at 36° R) improving to ± 0.13 K at 39 K ($\pm 0.23^{\circ}$ R at 70° R). For PRTS used to measure temperatures on the structure, insulation blankets, and the pressure switch plate, the probable error was $\leq \pm 0.33$ K ($\pm 0.59^{\circ}$ R) for temperatures > 55.6 K (100° R). Room temperature measurements on the payload simulator were within ± 1.6 K ($\pm 2.9^{\circ}$ R).

All thermocouples on or within the insulation, on tubes beneath the insulation, and on the tank fiberglass struts, were of 0.25-millimeter- (10-mil-) diameter chromel constantan and were referenced to 78 K (140° R) electronic ovens. The lead wires from these transducers ran through the duct and were temperature conditioned on the wall of the cold guard. The thermocouples on the structure and the shadow shields were also of 0.25-millimeter- (10-mil-) diameter chromel constantan; however, they exited from the test hardware through connectors mounted on the payload simulator. They were also referenced to 78 K (140° R) electronic ovens. Each chromel constantan thermocouple measurement channel had a computed probable error of ± 2.7 K at 20 K ($\pm 4.8^{\circ}$ R at 36° R) which improved to ± 0.79 K at 100 K ($\pm 1.4^{\circ}$ R at 180° R) and then dropped off to ± 2.7 K at 294 K ($\pm 4.8^{\circ}$ R at 530° R). The equipment box temperature was monitored by

four 0.25-millimeter- (10-mil-) copper constantan couples referenced to an ice point electronic oven. The instrumentation channels for these transducers had a probable error of ± 0.44 K at 294 K ($\pm 0.8^{\circ}$ R at 530° R).

All temperature sensors located on the insulation cover sheets and on the shadow shields were mounted by first laying a strip of double backed Mylar tape (2.5 cm, 1 in. wide) along the isothermal path desired for the wires. The choice of an isothermal path minimized any heat transfer to or from the temperature sensor along its lead wires. For the tank mounted insulation system this path was at least 30° of the tank meridional distance at the level of the transducers measurement point. For the shadow shields it was 60° of the circumference at the radial position of the thermocouple measurement junction. The transducer and its lead wires were then laid on the exposed tape surface and the assembly was covered with aluminized Mylar tape.

Temperature sensors on cylindrical surfaces (e.g., tank fiberglass support struts, vehicle structure struts, inside surface of the tank-to-guard duct, etc.) had their lead wires laid on an isotherm for 180° and then were adhesively bonded from the transducer to the point where the wires left the cylindrical surface.

Temperature sensors located on surfaces having little or no curvature (e.g., tank wall, pressure switch plate, cold guard, payload simulator, etc.) and their lead wires were also mounted and temperature conditioned by adhesively bonding them along an isotherm.

Liquid level sensors and PRTS inside the test tank were mounted on a low mass Bakelite support rake hung from the test tank lid. In addition, a resistor was also mounted on this rake to allow dissipation of electrical energy into the liquid propellant.

Temperatures of the individual shroud surfaces (e.g., top, each baffle, vertical sides, and bottom) were also measured. A total of 13 PRTS and 9 chromel constantan thermocouples were used. All transducers and sections of their lead wires were attached by adhesive bonding.

Hot cathode tubulated (enclosed) ionization gages were used to measure the vacuum level at two positions inside the shroud volume and at one position in the chamber outside the shroud. The transducers inside the shroud were mounted approximately 0.3 meter (1 ft) off the shroud floor and faced the vertical centerline of the shroud. The chamber gage was mounted at the middle of the chamber "side wall" and faced inward towards the shroud. A copper constantan thermocouple was bonded on the tubulation of each gage to measure its operating temperature.

Five mass flowmeters were used to measure the test tank boiloff gas flow rate. Their ranges were 0 to $49.8 \text{ m}^3/\text{hr}$ (0 to 1760 scfh), 0 to $2.83 \text{ m}^3/\text{hr}$ (0 to 100 scfh), 0 to $0.28 \text{ m}^3/\text{hr}$ (0 to 10 scfh), 0 to $0.03 \text{ m}^3/\text{hr}$ (0 to 1 scfh), and 0 to $0.003 \text{ m}^3/\text{hr}$ (0 to 0.1 scfh). These units were remotely valved into the test tank vent line as the boiloff rate came within their respective ranges. For any given boiloff rate the smallest range meter applicable was always employed. A standard copper constantan thermocouple and

bonded strain gage pressure sensor were used directly upstream of the bank of meters to verify that the boiloff gas state point was always within the operating limits of the meters. The probable error for each of these mass flow measurement channels was ± 2.5 percent of full-scale of the transducer range.

Measurements were recorded on an automatic voltage digitizing system and/or continuous, direct reading, strip charts. Digitized data was recorded only periodically, the frequency depending on whether the test hardware was going through a transient or a steady state condition.

TEST CONDITIONS AND PROCEDURE

The test vehicle structure and insulation system were exposed to three different temperature environments. The first condition, descriptively referred to as Near Earth, required that the vehicle payload and the shroud be maintained at approximately 294 K (530° R). During Deep Space, the second test condition, the payload was still maintained at 294 K (530° R) but the shroud was cooled to LH₂ temperature. The Null test condition required that both the payload simulator and the shroud be cooled with LH₂. The terms Near Earth, Deep Space, and Null will be used hereafter to denote the aforementioned test temperature conditions. Variations of these basic test conditions were steady state periods (1) at pressure levels higher than the chamber minimum vacuum and (2) Deep Space testing with the payload simulator at two other temperature levels. The payload simulator intermediate temperatures (i. e. , other than 294 K (530° R) or LH₂) were attained by simply regulating the amount of power to the heater strips adhesively bonded to the simulator. The cold guard was filled with LH₂ during all test conditions.

The total program was divided into two major test series. The first series was performed with the insulated tank and no shadow shields; the second group was performed after the two double sheeted shadow shields had been added. Each test series contained steady state periods at each of the three different temperature environments. Once a test series was started the procedure was to continue consecutively with different temperature environments unless interrupted by some sort of shroud failure in which case the testing was stopped, the hardware warmed, the leaks located and repaired, and testing resumed. A chronology of the different temperature environments for each major test series is listed in table IV. The vacuum level readings, area weighted payload temperatures, and area weighted shroud temperatures are also listed.

During all the test work conducted, a helium background existed in the chamber and in the shroud volume. In addition, when the shroud was being operated at LH₂ temperature, the tubulations of the ion gages inside the shroud volume were considerably colder than during the Near Earth test periods. As a result, both a helium gas correction and a gage operating temperature correction were made on the shroud volume vacuum level

readings taken during the Null and Deep Space test periods. The correction applied for the helium background was obtained from reference 19. The correction applied because of different gage tubulation temperatures is detailed in appendix C.

At the beginning of each major test series, or the resumption of testing after repair of a shroud failure, the warm test tank and insulation system were cooled as the tank was filled against a controlled backpressure of at least 13 N/cm^2 abs (19 psia). The decreasing boiloff flow rate was only roughly monitored by splitting the flow between the group of boiloff meters and the tank main vent line. Intermittent topping of the tank was continued during an additional insulation cooling period after the fill. Once the boiloff was below approximately $49.8 \text{ m}^3/\text{hr}$ (1760 scfh), the topping process was discontinued and the tank fill backpressure control valve (see fig. 18) was closed. The tank was then slowly vented (using the run backpressure control valve) to the desired steady state pressure. This venting operation served to release the excess sensible heat in the tanked liquid and ensure saturation at the lower pressure. The run backpressure control system was then put into automatic operation. Next, activation of the cold guard was accomplished in like manner using its fill and run backpressure control valves. The cold guard tank pressure was always maintained above the pressure in the insulated test tank during the initial fill, steady state, and retopping operations. This procedure assured that no boiloff gas from the test tank would condense in its vent line where the line passed through the cold guard tank.

At various times during the program both tanks needed to be topped or refilled. If the required operation involved only the cold guard, then that tank was filled according to the aforementioned procedure. If the operation involved both tanks, then they were refilled or topped concurrently with the condition that guard tank pressure always was kept higher than test tank pressure.

During steady state periods, the pressure differential between the two tanks was held constant. For the tests the differential was at least 1.5 millimeters of mercury.

Pressure levels other than the chamber minimum vacuum were created by bleeding ambient temperature GHe into the chamber. Flow was manually controlled using a micrometer needle valve located immediately outside the chamber wall.

DATA REDUCTION

The basic procedure used was to subtract all the solid conduction heat flows, the degrading effect of penetrations and seams in the insulation blankets, as well as any energy content release of the insulation, tank, ullage, and liquid propellant, from the latent and sensible energy increase of the measured gaseous hydrogen boiloff. The net heat transfer rate obtained was the heat flow through the uninterrupted insulation blankets. Thus,

$$\underbrace{\text{QBLKTS}} = \underbrace{\text{QBOILOFF}} - \underbrace{\text{DULLAGE} - \text{DTANK} - \text{DINSUL} - \text{DLIQUID}}$$

Heat transferred through uninterrupted insulation blankets

Latent and sensible heat content of boiloff gas

Energy content increase of ullage volume, tank wall, insulation system, and liquid propellant

- $\underbrace{\text{QSTRUTS}}$ - $\underbrace{\text{QDUCT}}$ - $\underbrace{\text{QWIRES}}$ - $\underbrace{\text{QPLUMBING}}$

Heat added by conduction down fiberglass struts

Heat added to tank by conduction through valve box wall and by radiation from duct volume

Heat added by conduction through instrumentation and control wires

Heat added by solid conduction through service lines and tubes connected to test tank

- $\underbrace{\text{QPINS}}$ - $\underbrace{\text{QPEN. EFFECTS}}$ - $\underbrace{\text{QSEAM}}$ (2)

Heat added by solid conduction through nylon positioning pins

Increased heat transfer through blankets due to penetration of fiberglass struts

Increased heat transfer through blankets due to presence of seams in blankets

Every term on the right side of the equation was experimentally evaluated during this program or derived as a direct result of work reported in reference 20. The term QBLKTS was then obtained directly by subtraction.

QBOILOFF

QBOILOFF is defined as the total latent and sensible heat gained by the liquid propellant evaporated during the boiloff process. After leaving the test tank and passing the backpressure control valve the gas was measured by a mass-type flowmeter. Temperature and static pressure transducers located immediately upstream of the flowmeter verified that the statepoint of the gas was within the operating limits of the meter. The mass flow rate of gas was determined using the equation

$$\dot{M}_{BO} = \dot{V}_{BO} \rho_{STP} \quad (3)$$

where $\rho_{STP} = \rho(294 \text{ K } (530^\circ \text{ R}), 1.0 \times 10^5 \text{ N/m}^2 \text{ (760 mm)})$. The mass flow rate was monitored constantly via a stripchart recorder during the entire test period. Discrete data points were recorded on magnetic tape at least every 20 minutes during the steady state periods. The value of QBOILOFF was then calculated from the magnetic tape data by the following equation:

$$Q_{BOILOFF} = \underbrace{\dot{M}_{BO} \lambda \left(\frac{\rho_{LIQ}}{\rho_{LIQ} - \rho_{SV}} \right)}_{\text{Latent heat}} + \underbrace{\dot{M}_{BO} (h_{TV} - h_{SV})}_{\text{Sensible heat}} \quad (4)$$

The factor $\rho_{LIQ}/(\rho_{LIQ} - \rho_{SV})$ corrects for the vapor that was formed but did not leave the test tank; it merely occupied the space vacated by the evaporated liquid.

Energy Content Changes

Since the tank and the environmental chamber pressures, as well as the shroud and payload temperatures, were maintained constant during each steady state period, it was expected that there would be no change in the energy content of the ullage, the tank wall, the insulation, or the LH_2 propellant. However, to detect any changes which might occur, temperature sensors were employed throughout these volumes and materials. Each sensor was assigned a volume of material, and any change in that temperature would result in an energy content change.

For the first three energy changes (i. e., DULLAGE, DTANK, and DINSUL) a close examination was made over all steady state periods of the temperature values required for their calculation. This study revealed that the experimentally measured temperatures used in the calculation of each energy change varied by less than their expected margin of error. The conclusion reached, therefore, was that these energy changes were below our level of detection and, hence, were considered to be zero for all steady state periods reported herein.

While the accuracy of the platinum resistance sensors (used in calculating DLIQUID) was $\pm 0.2 \text{ K}$ at 20 K ($\pm 0.36^\circ \text{ R}$ at 36° R), the authors found that saturation temperature changed by less than $\pm 0.78 \times 10^{-5} \text{ K}$ ($\pm 0.14 \times 10^{-4} \text{ }^\circ \text{R}$) during an steady state period. This value resulted from a review made of the tank pressure history during all steady state periods. No pressure changes equal to or greater than $0.27 \text{ N/m}^2 \pm 0.002$ millimeters of mercury (limit of strip chart resolution) were found to have occurred. The temperature variation of $\pm 0.78 \times 10^{-5} \text{ K}$ ($\pm 0.14 \times 10^{-4} \text{ }^\circ \text{R}$) corresponds to a DLIQUID change of only $\pm 0.0059 \text{ watt}$ ($\pm 0.02 \text{ Btu/hr}$). Since this is a small value, DLIQUID was assumed to be

zero for all steady state periods.

QSTRUTS, QWIRES, QPLUMBING, QPINS, and QDUCT

The first four of these terms were composed of pure conduction; the QDUCT value consisted of both a conduction and a radiation component. The conduction calculations were evaluated using the Fourier heat transfer equation

$$Q_{\text{COND}} = \frac{A}{L} \int_{T_1}^{T_2} k(T) dT \quad (5)$$

The radiation term was obtained from the equation

$$Q_{\text{RAD}} = \sigma AT^4 \quad (6)$$

In evaluating the terms QSTRUTS for all the Near Earth tests, the temperature differential was taken between two transducers located along the main axis of the strut near the tank end of one of the struts. The resulting heat transfer was considered to be identical for the other eleven struts. For the Deep Space tests, however, a different technique was used for determination of the differential temperature. The temperature readings from four different transducers along the main axis of a strut were plotted. A linear curve was then drawn through these points, the slope of which was considered the final value of $\Delta T/\Delta L$. The reason for using this technique was that temperature values measured during Deep Space were quite low, and an average of several measurements proved to be a better representation of the heat transfer than simply using just two discrete experimental temperature values. The heat transfer rate for these tests was also considered to be identical for all struts.

The term QWIRES consisted of the heat transferred via instrument and control wires to the tank from (1) the cold guard and (2) the pressure switch plate. The wires coming from the cold guard were of chromel, constantan, or manganin. The wires from the switch plate were all manganin. These instantaneous solid conduction heat transfer rates were evaluated using equation (5). Temperature boundaries were obtained from transducers located on the tank surface, the pressure switch plate, and the cold guard wall.

The term QPLUMBING consisted of the solid conduction heat transfer to the test tank from the cold guard and the pressure switch plate via the LH₂ fill line, the vent line, the pressure sensing tubes and the valve operator lines. Because of the presence of the cold guard, and the resulting insignificant temperature differential, no considera-

tion was given to heat transferred to the test tank by gases contained within these lines.

In calculating QPINS, the contributing 36 nylon positioning pins were considered to be in either of two different groups. The first group, 24 pins, were those located at the upper and lower insulation caps; the second group, 12 pins, were those around the equator of the tank. One thermocouple was on a pin near the upper insulation cap for pins in the first group and one thermocouple was on an equatorial pin for the second group. The tank wall temperature served as T_2 in equation (5). In the Near Earth tests, the pin heat transfer was taken as the sum of 24 times the rate for the upper end cap pin and 12 times the rate for the equatorial pin. In the Deep Space tests, only heat transfer through the upper end cap and equatorial pins was considered. The rate for these tests was the sum of 12 times that for the upper end cap pin plus 12 times the rate for the equatorial pin. The insulation outer surface temperature was very low for the lower half of the tank during the Deep Space tests. Consequently, the heat transfer for the 12 pins located at the bottom end cap was negligible.

As stated previously, the term QDUCT had two components: (1) solid conduction from the duct, through the fiberglass form of the valve box, to the test tank and (2) radiation from the duct volume, through the valve box-to-duct opening, to the test tank. The solid conduction term was evaluated using equation (5) with temperatures on the tank surface and the valve box wall as the boundary temperatures T_1 and T_2 . The radiation heat transfer was calculated using equation (6). The area A was that of the box-to-duct opening and the temperature T was determined from a thermocouple located on the duct. The opening of the duct was considered to be a perfect emitter because it was, in effect, a cavity. Further, because the hardware attached to the tank formed a group of highly absorbing cavities, the tank was assumed to be a perfect absorber.

QSEAM

The seam effect heat transfer was based on the results of flat plate calorimeter testing reported in reference 20. In that reference, the heat transfer rate per unit of seam length was determined to be 0.189 W/m (0.0164 Btu/(hr)(in.)).

On the large scale test tank of this report there were 20.6 meters (810 in.) of insulation seam length directly over the tank wall and 5.31 meters (208 in.) of length over fiberglass forms. Only the 20.6 meters (810 in.) directly over the tank wall was considered since the fiberglass forms reduced any heat transfer through the other 5.31 meters (209 in.).

For the minimum vacuum pressure Near Earth tests on the hydrogen tank, the seam effect was found by multiplying the calorimeter determined unit length heat transfer rate by 20.6 meters (810 in.) of seam length as follows:

$$(20.6 \text{ m})(0.189 \text{ W/m}) = 3.89 \text{ W}$$

$$(810 \text{ in.})(0.0164 \text{ Btu/hr})(\text{in.}) = 13.28 \text{ Btu/hr}$$

The work reported in reference 20 did not contain sufficient information to determine the effect of vacuum pressure level on the seam heat transfer rate. Therefore, the assumption was made for this report that the seam effect heat transfer rate was constant for the tests without helium bleed. For the tests with helium bleed the assumption was made that the seam effect heat transfer rate was the same percentage of the heat transfer through the insulation as it was in the first Near Earth test (NE-1).

No tests were reported in reference 20 for the effect of the seam on the heat transfer rate for the tank insulation boundary temperatures corresponding to those obtained in the Deep Space tests. In the Deep Space tests there is relatively little heat transfer to the tank through the insulation on the bottom half of the tank, since the outer insulation temperature on this half of the tank was low. The assumption was made that the seam effect was confined to the upper half of the tank insulation so that the seam length was taken as 10.3 meters (405 in.). The seam heat transfer rate per unit length of seam for the Deep Space tests without shadow shields was assumed to be the same percentage of the heat transfer rate through the insulation (20.3 percent) as for the first Near Earth test. For the Deep Space tests with shadow shields the seam effect heat transfer rate was neglected.

OPEN. EFFECTS

The penetration heat transfer rate was also based on the results of flat plate calorimeter testing. The increase in heat transfer rate between an uninterrupted blanket panel and the same panel after it had been penetrated with a single fiberglass tank support strut was 0.788 watt (2.69 Btu/hr) (ref. 20). This increase was composed of the heat conducted along the body of the strut into the calorimeter plus the MLI degradation due to the presence of the strut. For the large scale tank the experimentally determined conduction heat transfer for the 12 struts during Near Earth was 2.0 watts (6.8 Btu/hr) or 0.17 watt/strut (0.57 Btu/hr/strut). By using this strut heat leak for the large scale tank, and MLI degradation effect was calculated for a single strut penetration as follows:

$$(0.788 \text{ W}) - (0.17 \text{ W}) = 0.618 \text{ W}$$

$$(2.69 \text{ Btu/hr}) - (0.57 \text{ Btu/hr}) = 2.12 \text{ Btu/hr}$$

Since the large insulated tank had pairs of adjacent struts (as opposed to a single strut for the calorimeter tests), the heat transfer through the MLI per pair was between one and two times the heat transfer for a single strut. Analysis of the test tank insulation thermocouples showed a radius of influence of between 15 and 30 centimeter (6 and 12 in.) for each strut of any given pair. The amount of overlap at these two radii (centered on each of the two strut brackets of any given pair of struts) is such that the heat transfer through the MLI for the pair varies from 1.76 to 1.63 times that of a single bracket. A multiple of 1.7 was selected. As a result, the penetration effect for the test tank during Near Earth testing was

$$(6 \text{ strut pairs})(1.7)(0.62 \text{ W}) = 6.32 \text{ W}$$

$$(6 \text{ strut pairs})(1.7)(2.12 \text{ Btu/hr}) = 21.6 \text{ Btu/hr}$$

The test results reported in reference 20 indicated that the penetration effects were not influenced by increasing vacuum pressure. The tank supports penetrate the insulation on the bottom half of the tank. The outer insulation temperatures were low on the bottom half of the tank for all Deep Space tests. Therefore, the penetration effect was assumed to be zero for all Deep Space tests.

CORRELATION OF EXPERIMENTAL RESULTS AND ANALYSIS

The primary purpose of the test program was to verify the thermal design for the stage in a space environment. Because the minimum pressure obtainable within the vacuum chamber was greater than the pressure in the vacuum of space, there was concern that the tests might not yield accurate space simulation results. Therefore, tests were run at different vacuum pressure levels to determine the thermal performance of the stage in space. The measured temperatures did not differ significantly between tests at the minimum vacuum pressure and GHe bleed tests at 4 to 8 times minimum vacuum pressure. This indicated that the temperatures obtained for the minimum vacuum pressure tests were accurate simulations of the temperatures for a space environment. When the vacuum pressure was increased further by increasing the rate of helium bleed, there were significant changes in the measured temperatures. For the Near Earth tests the heat transfer rates for the tests without helium bleed indicated that the test vacuum pressures were sufficiently low that the results would be applicable to a space environment. For the Deep Space tests the heat transfer rates were significantly influenced by the vacuum pressure level. Fortunately, however, the data indicated that the heat transfer rates became asymptotic with respect to pressure at low vacuum pressure levels. The asymptotic heat transfer rates were taken as the performance in space

and were compared with analyses at zero pressure.

There are two major divisions within this section of the report. The first deals primarily with the tests without helium bleed and relates the test results to the expected performance in space. The second division deals with the results obtained for the tests with helium bleed as well as all of the Null tests. For the tests with helium bleed the ability of the analysis to account for the effects of pressure within the vacuum of the shroud is examined. Within each division of the section the heat transfer rates and temperatures for the Near Earth tests will be discussed. Following this the temperatures and their resulting heat transfer rates for the Deep Space tests will be discussed.

The sequence of tests is given in table IV. For each test the length of the steady state period, the average vacuum pressure inside the shroud and the measured boiloff heat transfer rate are shown. For the Near Earth tests the minimum measured boiloff heat transfer rate was 22.5 watts (76.9 Btu/hr). For the Deep Space tests with the payload-simulator at room temperature, the minimum heat transfer rate was 0.98 watt (3.33 Btu/hr) for the tests without shadow shields and 0.11 watt (0.36 Btu/hr) for the tests with shields. Even without the correction for the Null test results the heat transfer rate is within the design requirement of 0.21 watt (0.7 Btu/hr). Also, it should be noted that the Null heat transfer rate is about two-thirds of the heat transfer rate for the Deep Space test with shadow shields.

Space Simulation Results

Near Earth tests. -

Heat transfer rate: Table V gives a summary of the heat transfer rates for the Near Earth tests. Also shown in this table is the experimental shroud vacuum pressure. By comparing item 1 with item 6 for the minimum vacuum pressure tests (tests NE-1 to NE-5 and NE-7, NE-8, and NE-11) it can be seen that between 85 and 90 percent of the measured heat transfer given by item 1 was through the insulation.

Test NE-2 had electrical power supplied to a resistor inside the tank. All of this energy was reflected in increased boiloff.

The strut heat transfer rate is the heat transfer rate down the strut as measured by thermocouples on the strut. The penetration and seam effects are the results of tests on flat plate calorimeters. The procedure used to extrapolate the flat plate calorimeter heat transfer rates to this test configuration is given in the section DATA REDUCTION.

It can be seen from the data in table V that the sum of the heat transfer rates due to pins, seams, and penetrations of the insulation blanket (item 7 in table V) was over 50 percent of the assumed heat transfer rate through the insulation (item 6 in table V). The experimental heat transfer rate through the undisturbed insulation (item 8 in table V) was obtained from the difference between the two heat transfer rates. This rate was

then compared with the blanket heat transfer rate prediction (item 9 in table V) using equation (1). As can be seen from item 10 in table V there is good agreement between the predicted and experimental heat transfer rates for the initial tests. There was a 15 percent increase in the insulation heat transfer rate at minimum vacuum pressure for tests NE-5, NE-7, NE-8, and NE-11 relative to test NE-1. Test NE-5 occurred after the insulation was subject to a Deep Space test series but before the shadow shields had been added. The apparent degradation of the multilayer insulation as the tests progressed is discussed in reference 9.

Reference 2 gives a historical trend for the performance of multilayer insulation. In this comparison the product of the insulation overall thermal conductivity and density is taken as a measure of the insulation effectiveness. The data in this reference show that an insulation effectiveness about four times better than that obtained for the initial Near Earth test would be expected for flight-type tanks. This disagreement is due largely to differences in the insulation density rather than to differences in the overall thermal conductivity. The last historical point used in the trend had both the best effectiveness and an insulation density only about a third of that used in this test program. Also, the scatter in the historical data is greater than the absolute difference between the test insulation effectiveness and the historical trend. The weight of the insulation used in the test program increased from its absolute minimum due to the requirement that it be modularized and replaceable.

The predicted heat transfer rate is not known precisely due to uncertainties in both the layer density and the sheet emittance. The predicted blanket heat transfer rate for test NE-7 would be 20 percent less if a layer density of 11.8 layers/cm (30 layers/in.) were used rather than the assumed layer density of 17.7 layers/cm (45 layers/in.). It would increase by 34 percent if a density of 23.6 layers/cm (60 layers/in.) were used. This shows that uncertainties in the insulation layer density can significantly affect the predicted heat transfer. It is unlikely that the actual average layer density would vary by as much as ± 33 percent from nominal density of 17.7 layers/cm (45 layers/in.). The heat transfer rate is less sensitive to changes in the sheet emissivity. The uncertainty in the emittance measurements was about 0.005. Varying the emissivity in the heat transfer correlation by this amount resulted in a variation in the heat transfer rate of 6 percent.

For the shroud pressures encountered in the minimum vacuum pressure tests the analytic heat transfer rate was slightly affected by pressure. For test NE-5 which had the highest vacuum pressure without any helium bleed the analytic heat transfer rate decreased by 18 percent when zero pressure was assumed. Therefore the zero pressure analysis for test NE-5 would underpredict the experimental heat transfer rate by twice the amount that it underpredicts the heat transfer rate when the experimental pressure is included in the analysis.

Temperature comparisons: Table VI gives the insulation and tank support strut temperatures for each of the Near Earth tests. The insulation temperature profiles are similar for tests NE-1 to NE-4. Also, the temperature profiles for tests NE-8 and NE-11 are similar. For this table and others which follow, figure 20 gives the location of the sensors which are given in the first column. Figure 21 gives the experimental temperature profiles for each of the minimum vacuum pressure tests which had a unique profile. In this figure, and others which follow, the predicted temperature profile is given by a solid line. The effects of other analytic assumptions are shown by dashed lines.

For each of the tests the experimental temperatures at the interface between the two blankets are warmer than the predicted temperatures. It can be seen from the data in table VI that the meridional location of the thermocouples on the gore panel does not appear to be the cause of the difference. The temperatures for the thermocouple at the edge (HI-19) are warmer than the temperatures for the thermocouple near the edge (HI-18) but colder than the temperatures for the thermocouple in the center of the panel (HI-16), indicating no lateral heat transfer into the blanket at the edge of the gore panel.

Also shown in figure 21 are the effects of vacuum pressure and layer density for tests NE-5 and NE-7, respectively. Test NE-5 had the highest vacuum pressure for a Near Earth test without helium bleed. When the assumption was made of zero pressure within the insulation the resultant temperature profile was noticeably different. This zero pressure profile is in good agreement with the experimental temperatures. The analysis assumes that the shroud vacuum pressure exists everywhere within the insulations. Since the pressure decreases with temperature, the pressure between the colder layers could be significantly less than the shroud vacuum pressure.

Figure 21(c) shows the effect of layer density on the insulation temperature profile. It is seen to be small. Although not shown on the figure, an increase in the sheet emissivity from 0.053 to 0.063 changed the analytic profile by less than 3 K (5° R).

The temperatures of the fiberglass tank support struts are shown in table VI(b) and are nearly identical for each test without helium bleed. The temperatures drop below room temperature only close to the tank. This is the result of thermal radiation from the shroud to the strut. Figure 22 shows the experimental and analytic strut temperature profiles for test NE-7. There is experimental evidence of thermal contact resistance at the junction of the end fitting and the support bracket. Two analytic profiles are shown in figure 22. They differ in that one of them has a contact resistance while the other has none. This resistance was chosen so that the temperature of the titanium end fitting agreed with the experimental value and the analytic fiberglass strut temperatures were determined from heat transfer balances between the strut and its environment. Without the contact resistance the end of the strut is at the tank temperature. The experimental heat transfer rate was the result of strut temperature measurements and equaled 2.0 watts (6.8 Btu/hr). The analytic heat transfer rate computed across the

contact resistance was 2.4 watts (8.2 Btu/hr). When the contact resistance was neglected the analytic heat transfer at the end of the strut increased by 14 percent.

Deep Space tests. -

Temperature comparisons: The experimental temperatures for the truss structure and fiberglass tank support struts are given in table VII for both shadow shield and no shield tests. When shadow shields were added to the configuration, they intercepted much of the payload simulator energy which would have been incident on the truss structure. Consequently, with shadow shields the temperature of the truss structure was significantly lower along almost its entire length. This was in spite of the fact that, for the shadow shield tests, the payload simulator end of the truss structure was warmer due to the outside of the payload simulator support ring being coated to give a low emissivity surface. This was done to reduce the temperature difference between the simulator and support ring to better represent the flight vehicle. The two shadow shield tests with lowered payload simulator temperature (tests S-1 and S-2) were done primarily to provide data for the analysis of the shield sheet temperatures.

The comparison of the analytic and experimental temperatures of the truss structure and tank support members for the minimum vacuum pressure no shadow shield test (NS-1) is given in figure 23. Figure 23(a) gives the temperature profiles for the truss structure which consisted of the forward and midstructure truss. Figure 23(b) gives the temperature profiles for the fiberglass tank support struts. This figure shows that the shroud absorptivity has a noticeable effect on the midstructure temperature profile. Two analytic curves are shown in this figure. The curve for the lower absorptivity (0.93) is for the gray radiant heat transfer assumption where the absorptivity of the honeycomb on the shroud interior surfaces is determined from the emissivity of the paint at liquid hydrogen temperature. The curve for the higher absorptivity (0.98) represents a first order nongray approximation. Here the absorptivity of the honeycomb is determined by the wavelength corresponding to the temperature of the incoming radiation. Since most of the incoming radiation is from the payload simulator, the absorptivity of the shroud is assumed to be determined by the emissivity of the paint at the payload simulator temperature. For both curves the emissivity was taken to be equal to the absorptivity. Since the shroud is at liquid hydrogen temperature, it emits relatively little thermal energy.

It can be seen from the data in figure 23 that there is good agreement between the analysis and experimental data for both the truss structure and tank support struts. The higher absorptivity improves the agreement for the midstructure truss. For the minimum vacuum pressure test (NS-1), pressure had a negligible effect on the truss structure and tank support temperatures. This can be seen by comparing the experimental data in table VII for test NS-1 with the data for test NS-2 where the pressure was nearly five times higher. Similarly all the analytic temperatures for test NS-1 changed by less than 2 K (4° R) when the pressure was assumed to be zero.

The truss structure temperatures shown in table VII for the tests with shadow shields (S-1, S-2, and S-3) are compared with the predicted temperature profiles in figures 24 to 26. Again each figure has two parts. Part (a) has the temperature profiles for the truss structure and part (b) has the profiles for the tank support struts. The data are for three different payload simulator temperatures and no helium bleed into the shroud. There was good agreement between the predicted and experimental temperature profiles. The payload simulator temperature did not strongly influence the temperature of the tank support struts.

Table VIII gives the experimental insulation temperatures for each of the Deep Space tests. For the no shield tests the outer insulation temperature is fairly high for the upper half of the tank, but is near the shroud temperature for the lower half of the tank. For the tests with shadow shields the temperature of the insulation is low on both the top and bottom halves of the tank. Figure 27 gives the analytic and experimental outer insulation temperature profiles for the minimum vacuum pressure no shield test (NS-1). There is good agreement between the analytic and experimental temperatures for the upper half of the insulation. Using the nongray approximation with its consequent higher absorptivity for the shroud gives good agreement for the lower half of the tank, while not affecting the agreement for the upper half of the tank. By comparing the outer insulation temperatures given in table VIII for the no shield tests it can be seen that increasing the vacuum pressure within the shroud had a negligible effect on these temperatures.

Table IX gives the experimental temperatures for the shadow shields. There were thermocouples on the outside of all sheets of the shadow shields. Also, thermocouples were mounted on the inside of all sheets except for the warm sheet of the shadow shield next to the tank. The inside surface of a sheet is that side which sees the other sheet of the same shield. The analytic and experimental temperature profiles for the shields and the outer surface of the insulation are given in figure 28. The data in this figure are for the three different payload simulator settings and no helium bleed (S-1, S-2, and S-3).

There is good agreement between the analysis and the experimental data for the outer insulation temperatures. This is largely a consequence of the good agreement for the temperatures of the coldest sheet of the shadow shields. The short horizontal lines on the figure at the edge of the shadow shield are the analytic prediction for the temperature of each shadow shield ring. The apparent agreement between the analysis and the experimental data is the consequence of the choice for a contact resistance between the shadow shield ring and the struts of the forward truss structure. A contact resistance of 0.11 W/K ($0.20 \text{ Btu/(hr)}(^{\circ}\text{R})$) was used between each ring and the truss structure. With the payload simulator at room temperature assuming perfect conduction between the ring and the truss resulted in the payload shield ring temperature increasing by 8 K (15° R). Assuming no conduction between the ring and the truss resulted in a decrease of 13 K (24° R). The corresponding changes for the ring of the tank shield were a 6 K (10° R) increase and a 36 K (64° R) decrease.

Temperature differences across shadow shield sheet thickness: As can be seen from figure 28(a) and table IX the experimental thermocouples showed a temperature difference across each sheet of the payload shield. This temperature difference increased with increased payload simulator temperature. For the low temperature payload simulator setting (test S-1) there is good agreement between the analysis and the experimental data. This is not true for the sheets of the payload shadow shield with the payload simulator at room temperature (test S-3). The analysis agrees only with the thermocouple readings on the sides of this shield which face the payload simulator. After the Deep Space tests had been completed small scale tests were done to try to resolve the questions associated with the temperature difference across the sheet. A description of the small scale testing is given in appendix D. The small scale tests indicated that for sheet temperatures similar to those of the full scale testing the actual sheet temperature was close to the thermocouple readings for thermocouples on the side of the sheet facing the payload simulator. If this also occurred for the full scale testing, there was good agreement between the analysis and the experimental data. The small scale testing also showed that the apparent temperature difference across the sheets was a function of the material used for the sheets of the shadow shields.

Heat transfer rate: Table X gives the heat transfer rates for all the Deep Space tests. It can be seen that the heat transfer rates are strongly influenced by pressure, especially the blanket correlation. In the no shadow shield tests the major source of heat transfer was through the insulation, while for the tests with shadow shields the Null heat transfer rate was a large fraction of the measured heat transfer rate.

In space the pressure would be much lower than that encountered in the shroud volume. The heat transfer rates at zero pressure are necessary to determine the space performance of the insulation. The procedure used to determine the space performance of the system will be discussed in a section under pressure effects, and the results will be summarized here.

When the experimental heat transfer rates were plotted as a function of shroud vacuum pressure they approached asymptotic values as the pressure decreased. These asymptotic values were then compared with the analytic heat transfer rates at zero pressure to determine the thermal performance in space. For the no shadow shield tests the experimental blanket heat transfer rate (item 6 in table X) approached an asymptote of 0.41 watt (1.4 Btu/hr) at low pressures. The blanket correlation at zero pressure is 0.25 watt (0.85 Btu/hr) so that the analysis is expected to underpredict the heat transfer in space by 64 percent. This is in contrast to the test results at minimum vacuum pressure (test NS-1) where the analysis overpredicts the experimental heat transfer rate by 52 percent.

It can be seen from table X that for each test where shadow shields were used, the measured heat transfer rate was not much greater than the Null heat transfer rate. All the other experimental heat transfer rates for each test are much lower and are not

known precisely. Their cumulative effect is almost as great as the Null test heat transfer rate. The simplest procedure to obtain the space heat transfer rate is to subtract the asymptotic low pressure Null heat transfer rate from the measured heat transfer rate. This asymptotic Null heat transfer rate was 0.068 watt (0.23 Btu/hr), while the asymptotic measured heat transfer rate for the shadow shield test was 0.094 watt (0.32 Btu/hr). The difference of 0.026 watt (0.09 Btu/hr) compares favorably with the total analytic heat transfer rate at zero pressure and 22 K (40° R) surroundings of 0.035 watt (0.12 Btu/hr). Hence the analysis is expected to overpredict the space heat transfer by 35 percent. It should be noted that the analysis used the predicted outer insulation temperatures to predict the space heat transfer rates for both the shadow shield and no shield cases.

There is good agreement between the analysis and the experimental data when the data is extrapolated to the zero pressure condition of space.

The experimental tank support strut heat transfer rate for the no shadow shield test (NS-1) at minimum shroud vacuum pressure was 0.062 watt (0.21 Btu/hr). The analytic strut heat transfer rate was 0.085 watt (0.29 Btu/hr). With shadow shields the experimental rate was 0.015 watt (0.05 Btu/hr) and the analytic rate was 0.013 watt (0.043 Btu/hr) for Deep Space simulation test (S-3). For both cases the agreement is good.

Environmental Chamber Pressure Effects

There was concern that the pressure in the vacuum chamber would influence the test results so that they would be different from those obtainable in the vacuum of space. The approach used to verify that the lowest pressure test results approximated the results for a space vacuum was to conduct tests at different pressure levels. For the Null, Near Earth, and Deep Space configurations tests were run for at least three different vacuum pressure levels. The higher pressure levels were achieved by bleeding gaseous helium into the vacuum chamber in order to raise the pressure inside the shroud significantly above that achieved by the vacuum pumps.

Near Earth tests. - When helium was bled into the shroud volume during the Near Earth test, the most noticeable effect was an increase in the boiloff rate. There was also some decrease in the insulation temperatures and a slight increase in the fiberglass strut temperatures near the tank.

Heat transfer rates: The blanket heat transfer rate and the heat transfer prediction are shown in figure 29 as a function of vacuum pressure. The tests without helium bleed as well as those with helium bleed are shown.

The experimental results for tests NE-1 to NE-6 are in good agreement with the analytical prediction. The experimental results of tests NE-7, NE-8, and NE-11 indicated poorer insulation performance for the no bleed tests. Part of the discrepancy between the predicted and experimental heat transfer rates for tests NE-9 and NE-10 could

be the result of inaccuracies in the shroud ionization gage pressure measurements. A byproduct of the testing reported in appendix C showed that the pressure readings for different filaments could differ by a factor of two.

Temperature comparisons: Figure 30 gives the analytic and experimental temperatures through the insulation for each of the tests in which helium was bled into the shroud volume. Figure 30(a) is for the short time test NE-6 and illustrates how even though the boiloff measurement was near equilibrium the midpoint insulation temperatures were not. In this test the boiloff was measured for an hour after the helium bleed was started. Within 5 minutes of the start of the bleeding the boiloff had doubled, and then gradually decreased by 10 percent during the course of the hour. When test NE-9 was started, there was a similar behavior in the boiloff rate. The boiloff rate climbed immediately to 120 percent of the eventual steady state value. Over a period of 8 hours the boiloff decreased to the steady state value. However, in test NE-9, the temperatures for the midpoint took over 15 hours to reach their steady state values. The insulation temperatures for test NE-6 are transient temperatures even though the measured boiloff for this test, based on the results of test NE-9, is probably not greater than 110 percent of the steady state rate which would be achieved if the test had been prolonged.

The effects of variation in the insulation vacuum pressure are also shown in figure 30. In figure 30(b) and (c) the data agree with the analytic curve for a pressure less than the shroud vacuum pressure. From figure 21 this can also be seen for the no bleed tests. Using a pressure below the shroud vacuum pressure for the analysis improves the agreement between the analysis and the experimental data.

There is experimental evidence that the actual vacuum pressure was not the same for tests NE-5 and NE-9. From table VI it can be seen that the shroud vacuum pressure is approximately the same for tests NE-5 and NE-9. The vacuum pressure is also approximately the same for tests NE-4 and NE-8. The temperature differences between tests NE-4 and NE-5 are less than the temperature differences between tests NE-8 and NE-9 for the outer blanket gore panel. This indicates that the actual vacuum pressure differential between tests NE-4 and NE-5 is less than the actual vacuum pressure differential between tests NE-8 and NE-9. The actual vacuum pressure for test NE-9 may have been greater than the pressure for test NE-5.

Null tests. - Five Null tests were conducted. One occurred prior to the Deep Space tests without shadow shields; three occurred prior to the Deep Space tests with shadow shields and one after these tests. Figure 31 gives the measured heat transfer rate for each of the Null tests as a function of shroud vacuum pressure. Tests NU-3 and NU-4 had a helium bleed into the chamber while the others did not. Even without a helium bleed the major constituent of the gas in the chamber was helium. This was based on measurements made with a residual gas analyzer during the tests. The difference in the heat transfer rates between tests NU-1 and NU-3 was 0.04 watt (0.13 Btu/hr) and is a measure of the uncertainty in the heat transfer rate due to variations in the boiloff of

hydrogen. These heat transfer rates were very low, and there were considerable fluctuations in the measured boiloff during the steady state periods. The ordinate of figure 31 is the heat transfer obtained from the average measured boiloff rate. No correction was made for other sources of heat transfer. The measurements for the other sources of heat transfer were lower than the threshold values associated with the thermocouple sensors. The faired curve passing through the data in figure 31 was used to determine the Null test heat transfer rate as a function of vacuum pressure, and is not an analytic prediction.

Deep Space tests. - Both the analytic and experimental data for the minimum vacuum pressure tests both with and without shadow shields indicated that the measured temperatures accurately represent the results obtainable in space. However, the analytic, and to a lesser extent the experimental heat transfer rates, were strong functions of pressure. The experimental and analytic temperature profiles will be compared for the shadow shield and no shield tests with helium bleed. The purposes of doing this are to show the effects of pressure and to indicate that the vacuum pressure in the test volume of the shroud was probably close to the measured value.

Temperature comparisons: The analytic and experimental structure temperature profiles for the two no shadow shield helium bleed tests (NS-2 and NS-3) are given in figures 32 and 33. Part (a) of each figure gives the temperatures for the truss structure while part (b) gives the temperatures for the tank support struts. In addition to a prediction using the measured vacuum pressure, two additional analytic profiles are shown for each figure for pressures less than and greater than the measured pressure. They are profiles in which the shroud vacuum pressure differed by a factor of two from the measured pressure. Except for the free end of the midstructure strut, the experimental temperatures are bounded by the pressure profiles. As shown in figure 23, using the higher shroud absorptivity to approximate the nongray analysis would result in the midstructure strut temperatures being bounded by the pressure curves.

Figures 34 and 35 give the structure temperature profiles for the two shadow shield tests with helium bleed. The experimental data in figure 35 indicated that the actual shroud vacuum pressure may have been more than a factor of two higher than the measured pressure for the highest vacuum pressure test. This is consistent with the results obtained for the last Near Earth test with helium bleed (NE-10) as shown in figure 29. The Deep Space tests with shadow shields immediately preceded the last series of Near Earth tests. For the highest vacuum pressure Deep Space and Near Earth tests there would have been better agreement if a higher pressure had been used in the analysis.

For the Deep Space tests with no shields the experimental outer insulation temperatures were virtually unchanged by the addition of helium into the shroud volume. This can be seen from the data in table VIII. There is, however, a greater change in the analytic outer insulation temperature with pressure because of a greater analytic heat transfer rate through the insulation. As an illustration the analytic temperature at the

centerline for the top of the tank was 1.8 K (3.3° R) less for test NS-2 than for test NS-1. For test NS-3 this temperature was 5 K (9° R) less than the temperature at the same point for test NS-1.

Figure 36 gives the shadow shield and insulation temperatures for the two Deep Space tests with shadow shields and helium bleed (S-4 and S-5). These results can be compared with the data from test S-3 shown in figure 28(c) for the room temperature payload simulator and no helium bleed. The relative agreement between the analysis and the experimental data is about the same when helium was bled into the shroud. An exception to this is the ring of the tank shadow shield for the highest vacuum pressure test. The experimental temperature difference across the thickness of the cold sheet of the payload shadow shield decreased with increasing vacuum pressure, while the average temperature level for the sheet remained relatively constant.

The centerline temperature for the coldest sheet first decreased and then increased as the shroud vacuum pressure increased. This is true both analytically and experimentally.

Heat transfer rate: Figure 37 gives the blanket heat transfer rate and the analytic insulation heat transfer rate as a function of shroud vacuum pressure for the Deep Space tests without shadow shields (NS-1, -2, and -3). Figure 38 gives the total measured heat transfer rate and the total analytic heat transfer rate as a function of shroud vacuum pressure for the tests with shadow shields (S-3, S-4, and S-5). In figure 38 the measured heat transfer rate is plotted rather than the blanket heat transfer rate because of large relative uncertainties in the rates which are used to determine the blanket heat transfer rate from the measured heat transfer rate for the tests with shadow shields.

From both of these figures it can be seen that the analysis severely overpredicts the effect of vacuum pressure on the heat transfer rate. However, the trend of the experimental data and the analysis converge at very low pressures. The difference shown in figure 38 between the experimental data trend and the analysis at low pressure is about the same magnitude as the asymptotic null heat transfer rate shown in figure 31.

It can be seen from figure 37 that an analysis incorporating a pressure one-tenth of the shroud vacuum pressure would be in good agreement with the experimental data for the no shadow shield tests. For the tests with shadow shields the data in figure 38 show that using a pressure one-fifth of the shroud vacuum pressure in the analysis would give fair agreement with the experimental data when the effect of the Null heat transfer rate is included with the experimental data. The pressure used in equation (1) for the heat transfer rate is the pressure given by the vacuum gage within the shroud. This results in good agreement between the predicted and experimental heat transfer rates for the initial Near Earth tests. In free molecular flow the pressure varies inversely as the square root of the temperature and correcting the pressure used in equation (1) to that corresponding to the outer insulation temperature would not significantly affect the results. This is not true for the Deep Space tests, since the temperatures of the outer in-

sulation are only a small fraction of the temperature of the pressure gage. An additional analytic curve is shown in both figures 37 and 38 where the local insulation heat transfer rate used the gage pressure corrected to the local outer insulation temperatures. In the analysis, when the local pressure has been reduced from the shroud vacuum pressure there is better agreement with the experimental data.

SUMMARY OF RESULTS

The report presents the results of an effort to demonstrate that cryogenic propellants can be stored for long periods of time in space. To do this the following was accomplished: (1) the thermal requirements necessary to store cryogenic propellants without venting for a 1200-day Saturn orbiter mission were determined; (2) an integrated thermal protection system suitable for both the near Earth and interplanetary coast phases of the mission was designed and fabricated; (3) the thermal simulation of that portion of the stage encompassing the hydrogen propellant tank was accomplished; (4) the experimental results were correlated with analytic predictions.

The experimental program was divided into two phases which simulated different portions of the mission. The early phase of the mission in which the vehicle is near the Earth would have relatively high heat transfer rates. For the initial Near Earth test in which the outside temperature of the insulation was close to room temperature, the measured heat transfer to the hydrogen tank was 22.0 watts (75.1 Btu/hr); 2.8 watts (9.5 Btu/hr) of this heat transfer rate was to the tank from sources other than the insulation. Of the remaining 19.2 watts (65.6 Btu/hr), 12.2 watts (41.7 Btu/hr) were chargeable to disturbances caused by insulation support pins, seams, and penetrations to the multilayer insulation blanket. This left 7.0 watts (23.9 Btu/hr) as an estimate of the heat transfer rate for the multilayer insulation blanket. This heat transfer rate was within 10 percent of the heat transfer rate predicted analytically. As the testing progressed, the experimental heat transfer rate for the tests without helium bleed increased. Since the analytic heat transfer rate for the blanket heat transfer rate remained relatively constant, the agreement between the analysis and the experimental data became poorer.

For the majority of the mission the heat transfer rate to the propellants had to be low. For the hydrogen tank the allowable heat transfer rate was 0.21 watt (0.7 Btu/hr). In order to achieve this heat transfer rate the thermal protection system required that the vehicle be sun-oriented and incorporate an open truss structure, shadow shields, low conductivity tank supports, low heat leak plumbing and electrical lines, as well as the multilayer insulation. Tests of this thermal protection system resulted in measured heat transfer rates of 0.11 watt (0.36 Btu/hr) which was only about half of the allowable heat transfer rate for the mission. The estimate of the Null heat transfer rate at zero pressure was 0.068 watt (0.23 Btu/hr) while the estimate of what the measured heat transfer

rate would have been at zero pressure for the shadow shield test was 0.094 watt (0.32 Btu/hr). This difference of 0.026 watt (0.09 Btu/hr) compares favorably with the predicted heat transfer rate at zero pressure of 0.035 watt (0.12 Btu/hr). The pretest design heat transfer rate was 0.026 watt (0.09 Btu/hr), and the principal difference between the analytic heat transfer rate at zero pressure and the design heat transfer rate was the inclusion of a shroud at 22 K (40⁰ R). For missions of shorter duration a higher heat transfer rate would be acceptable and shadow shields might not be necessary. For the minimum vacuum pressure test without shadow shields the measured heat transfer rate was 0.98 watt (3.33 Btu/hr). About 90 percent of this heat transfer rate was through elements which would be on the flight vehicle, and about half of the measured heat transfer rate was chargeable to the undisturbed multilayer insulation. Due to the strong effect of pressure on the analytic correlation, the analysis overpredicted the blanket heat transfer for the test at minimum vacuum pressure, but it underpredicted the expected space heat transfer at zero pressure.

There is good agreement between the analysis and the experimental temperatures for the structure for all of the Deep Space tests. In addition the analysis gives an accurate prediction for the outer insulation temperatures. Within the uncertainty in the pressure measurements the analysis is able to account for the effect of vacuum pressure inside the shroud on the component temperatures. The experimental data show an apparent temperature differential across the thickness of a sheet of a shadow shield. This appeared to be the result of the choice of the material for the shadow shield sheets.

CONCLUDING REMARKS

The results of the test program showed that cryogenic propellants can be stored for long duration in space without loss of fluid. In order to compare the heat transfer rates with the results of other investigators the simulation of the vehicle near Earth was done with the outer insulation at room temperature. Since the outer insulation temperature is expected to be less, the actual heat transfer rate would be less. If in the near Earth phase the outer insulation temperature was 167 K (300⁰ R) the heat transfer rate would be less than half. Also, as the vehicle moved further from the sun, the heat transfer rate to the hydrogen tank when the vehicle was not sun-oriented would be less than in the near Earth phase. If the total heat to the vehicle when it was unoriented was the same as the rate for test NE-1 over a 1-day period, a total of 528 watt-hour (1800 Btu) would be absorbed. This quantity of heat is less than 10 percent of the total allowable heat transfer to the hydrogen tank for the entire mission.

There was difficulty in accurately determining the low heat transfer rates for the Deep Space tests with shadow shields and for the Null tests. Much of this seemed to be caused by the inability of the backpressure control system to maintain a finer resolution

of the tank pressure at the extremely low boiloff values encountered. If tests with similar heat transfer rates are conducted, care should be taken to ensure that the tank pressure can be controlled with a finer resolution. It was also found that low thermal conductivity electrical leads were essential both to reduce heat transfer to the hydrogen propellant and to obtain accurate sensor readings.

Lewis Research Center,
National Aeronautics and Space Administration,
Cleveland, Ohio, October 22, 1976,
506-21.

APPENDIX A

SYMBOLS

A	area, m^2 ; ft^2
B	proportionality constant
DINSUL	energy content change of insulation system, W; Btu/hr
DLIQUID	energy content change of test tank liquid, W; Btu/hr
DTANK	energy content change of test tank wall, W; Btu/hr
DULLAGE	energy content change of test tank ullage, W; Btu/hr
h	specific enthalpy, J/kg; Btu/lb
K	Boltzmann's constant
k	thermal conductivity, W/(m)(K); Btu/(hr)(ft)($^{\circ}$ R)
L	length or thickness, m; ft
\dot{M}	mass flow rate, kg/hr; lb/hr
\bar{N}	insulation layer density, layers/cm; layers/in.
N_S	number of insulation sheets, dimensionless
P	pressure, N/cm^2 ; torr
QBLKTS	heat transferred through uninterrupted insulation blankets, W; Btu/hr
QBOILOFF	latent and sensible heat content of boiloff gas, W; Btu/hr
Q_{COND}	heat transferred by conduction, W; Btu/hr
QDUCT	heat added to tank by conduction through hat wall and radiation from duct volume, W; Btu/hr
QPEN. EFFECTS	increased heat transfer through insulation blankets due to the pene- tration of fiberglass struts, W; Btu/hr
QPINS	heat added by solid conduction through insulation support pins, W; Btu/hr
QPLUMBING	heat added by solid conduction through service lines and tubes con- nected to test tank, W; Btu/hr
Q_{RAD}	heat transferred by radiation, W; Btu/hr

QSEAM	increased heat transfer through insulation blanket system due to presence of seams between blankets, W; Btu/hr
QSTRUTS	heat added by conduction down fiberglass struts, W; Btu/hr
QWIRES	heat added by conduction through instrumentation and control wires, W; Btu/hr
q	heat flux, W/m^2 ; Btu/(ft ²)(hr)
T	temperature, K; °R
\dot{V}	volumetric flow, m ³ /hr; ft ³ /hr
ϵ	emissivity
Δ	indicates a differential
λ	latent heat of evaporation, J/kg; Btu/lb
ρ	density, kg/m ³ ; lb/ft ³
σ	Stephen-Boltzmann constant, $5.668 \times 10^{-8} W/(m^2)(K^4)$; $1.713 \times 10^{-9} Btu/(hr)(ft^2)(^{\circ}R^4)$

Subscripts:

BO	boiloff
LH ₂	liquid hydrogen
LIQ	liquid
n	index
sh	insulation sheet
STP	standard temperature and pressure
SV	saturated vapor
TV	tank vent
0	outside surface of insulation
1, 2	denote a position

APPENDIX B

ICE BATH CONSIDERATIONS

The pressure difference between the test tank and a reference volume (located outside the environmental chamber) was the feedback signal in the test tank closed loop backpressure control system. In order to maintain a constant pressure in the reference bottle, it was submerged in an ice-water bath. Any variation in bath temperature caused a change in reference pressure which manifested itself as a change in the test tank boiloff.

During test operations, all of the three following anomalies in test tank boiloff were encountered at one time or another: (1) mixer motor stoppage and resulting dropoff in tank boiloff, (2) a short term (15-min maximum) rise in boiloff immediately after adding ice to the reference volume bath, and (3) anomaly (2) followed by a drop in boiloff (over a period of hours) from its steady state value existing prior to ice addition.

A detailed consideration of the thermodynamics of the ice-water bath is needed to explain these anomalies.

In an ice bath, being influenced by an influx of heat from the surrounding environment, a natural pattern of convection as shown in figure 39 is expected. Because of this convection a temperature profile such as B (see fig. 40) will exist. A mixer motor is employed to destroy this profile and approach a condition labeled as "desired bath temperature" (again see fig. 40). Since this desired bath temperature profile is difficult to reach, a condition portrayed by profile C exists in the ice-water mixture.

If the mixer motor stops, the bath will tend to warm and approach profile B. When this happens, the reference volume is warmed; it increases in pressure and causes the control system to respond as though the LH_2 tank pressure had dropped, thus closing down the vent flow control valve.

Consider, now, the case where ice is added to the bath when profile C exists in the ice-water mixture. The addition of ice would drive profile C toward the "desired" temperature curve because the ice region would increase in depth. The resulting lower temperature would cause the reference volume pressure to drop and the control system to respond as though the LH_2 tank pressure had risen, thus further opening the vent flow control valve. However, after the ice addition is made, the bath temperature would tend to increase toward some intermediate profile represented again by profile C in figure 40. This temperature profile would be expected simply because of the mixing inhibiting effect the extra ice causes by its presence. This "bath warming" would cause the reference volume to warm, the reference pressure to rise, and the LH_2 tank boiloff to decrease.

If the ice bath is considered a "lump system" (i. e., let one value of temperature

be used to describe the bath), then a plot such as figure 41 may be drawn to display the relation between bath temperature, test tank pressure, and possible error in hydrogen vent gas flow rate. This figure will be used to assess credibility limits on the extremely low boiloff values encountered in this test program.

During actual testing, the most difficulty with test tank boiloff was encountered because of previously mentioned anomaly (3). Quantitatively speaking the maximum drop in boiloff was a value of $0.007 \text{ m}^3/\text{hr}$ (0.24 scfh). If this boiloff change is used in conjunction with figure 41, the result is that the ice bath "lump temperature" would only have to have increased by 0.006° C (0.011° F) over an hour time period. Considering the "data in hand" and the foregoing analysis, the authors cannot guarantee boiloff values within the computed error value $0.007 \text{ m}^3/\text{hr}$ (0.24 scfh).

The major point to be made is the extra care necessary when constructing an ice bath reference for extremely low boiloff testing. Improvements to the system used in this report would be as follows: (1) more mixing in the ice-water solution is necessary; (2) ice should be added to the bath more frequently (the bath used for this testing was serviced only at the beginning and end of each daily work shift); (3) the reference volume tank (considered to be cylindrical) should be mounted horizontally so it exists more nearly on an isotherm in the bath; (4) an annular screen "cage" should be mounted around the reference volume tank to prevent ice from coming into direct contact with the tank walls.

The authors believe that, if these extra design considerations were added to the existing backpressure system, the result would be a control system capable of being used confidently in extremely low boiloff testing.

APPENDIX C

DEVELOPMENT OF TUBULATION TEMPERATURE CORRECTION

FOR IONIZATION GAGE READINGS

General Theory

The following statement is taken from reference 19: ". . . a gage (ed. ionization gage) responds to the concentration of molecules within its ionizing zone. In a steady flow system, or in any system where the gage enclosure is only a small part of the high vacuum zone, the concentration of molecules in the gage is inversely proportional to the square root of the absolute temperature of the surfaces enclosing the gage sensing element." That is,

$$GR_2 = GR_1 \sqrt{\frac{T_1}{T_2}} \quad (C1)$$

where GR denotes gage reading and the subscripts denote different readings.

It can safely be stated that the gas within the ionizing zone of a gage is at the temperature of the gage tubulation because almost all the collisions that a molecule would undergo are with the "wall" formed by the tubulation.

Consider two different tubulation temperatures, T_1 and T_2 , such that

$$T_2 > T_1 \quad (C2)$$

It follows from equation (C1) that $GR_2 < GR_1$. These gage readings are a direct result of gas concentration (i. e., n) within the ionizing zone of the gage and can be expressed as

$$GR_1 = Bn_1 \quad (C3)$$

and

$$GR_2 = Bn_2 \quad (C4)$$

where B is a proportionality constant and n is the molecular density expressed in molecules/cm³.

Each gage reading GR_n corresponds to some value of vacuum pressure P_n within

the ionizing zone of the gage. At some tubulation temperature, say T_1 , we know that

$$GR_1 = P_1 \quad (C5)$$

from a prerun calibration. Applying the simple perfect gas law at T_1 , we can write

$$P_1 = n_1KT_1 \quad (C6)$$

where K is Boltzmann's constant. Similarly, at T_2

$$P_2 = n_2KT_2 \quad (C7)$$

From equations (C7) and (C4)

$$P_2 = \frac{GR_2}{B} KT_2 \quad (C8)$$

Since $B = GR_1/n_1$ from equation (C3),

$$P_2 = \frac{GR_2}{GR_1} n_1KT_2 \quad (C9)$$

Multiplying by T_1/T_1 and regrouping result in equation (C9) becoming

$$P_2 = \frac{GR_2}{GR_1} n_1KT_1 \frac{T_2}{T_1}$$

or

$$P_2 = \frac{GR_2}{GR_1} \frac{T_2}{T_1} P_1 \quad (C10)$$

Determination of, and Representation of, Terms in Equation (C10)

An experimental test was conducted at several different vacuum levels to determine the relation between gage reading (i. e. , GR) and gage tubulation temperature. Schemat-

ically, the test arrangement is as shown in figure 42.

Four major sets of data were taken. Set 1 consisted of GR data taken at a minimum of six different gage 1 tubulation temperatures, while a constant vacuum pressure, indicated by gage 2, was maintained in the chamber. In total, this temperature effect data was obtained at five different, constant, vacuum pressure levels. The background gas for Data Set 1 was GN_2 .

Data Set 2 was identical to Set 1 except the background gas was helium.

The oven was then moved such that it encapsulated gage 2 (see fig. 42). Data Sets 3 and 4 were obtained from gage 2 using GHe and GN_2 , respectively.

All four sets of data are shown in figures 43 and 44. From these curves, at a constant value of the abscissa (tubulation temperature "x"), ordinate values (i. e., vacuum pressure level) were read and the ratio of $\text{GR}_{432 \text{ K}}/\text{GR}_x$ ($\text{GR}_{7770 \text{ R}}/\text{GR}_x$) was computed for each curve. An average of the ten values was considered to be the $\text{GR}_{432 \text{ K}}/\text{GR}_x$ ($\text{GR}_{7770 \text{ R}}/\text{GR}_x$) at temperature T_x . Figure 45 is a plot of this $\text{GR}_{432 \text{ K}}/\text{GR}_x$ ($\text{GR}_{7770 \text{ R}}/\text{GR}_x$) as a function of tubulation temperature and represents the first ratio in equation (C10). The value of 432 K (777° R) representing T_2 was selected as a common comparison temperature simply because it was the average tubulation temperature of the ion gages used inside the shroud during all the Near Earth tests. As expected, the ratio of gage readings over the range of testing varies as $\sqrt{T_1/T_2}$ (see interrupted curve of fig. 45).

Before projecting the raw gage readings from the insulated tank tests, the assumption was made that the gage reading at condition 1 (i.e., the reading obtained during each separate tests on the insulated tank) was the actual vacuum pressure level in the shroud volume. This value was corrected for the GHe background which had existed in the chamber during the experiment. The corrected value then represented P_1 in equation (C10). The last term in equation (C10), T_2/T_1 , was computed using the tubulation temperature obtained during each independent test on the tank as T_1 and 432 K (777° R) as T_2 .

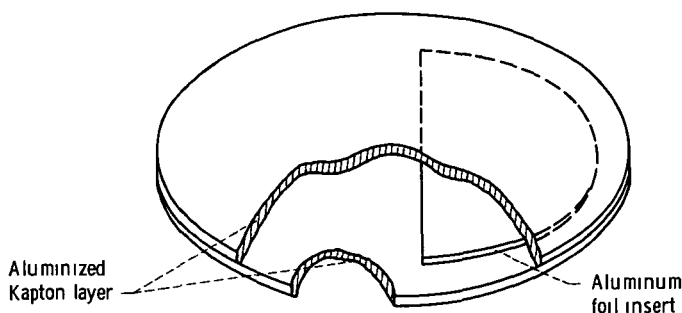
In conclusion, the authors wish to state that calibrating the ion gage as a function of tubulation temperature does not improve the accuracy but does improve the confidence of using the gage over the range of operating temperatures.

APPENDIX D

SHADOW SHIELD SMALL SCALE TEST RESULTS

The test results indicate a temperature difference across each sheet of the payload shadow shield. In an effort to determine the cause of this apparent temperature difference a series of small scale tests were done. This appendix contains a brief description of the tests and a summary of the results.

The small scale tests were done with double sheeted shadow shields 36 centimeters (14 in.) in diameter in a vacuum chamber with a liquid nitrogen cooled cryoshroud. The small scale shields were made from two different materials. The sheets of one shield were made from Schjeldahl X-850 material, which was the same material used for the full scale shadow shields. Each sheet of the other shield was made by laminating two single aluminized Kapton sheets together. A thermocoupled aluminized foil insert was placed between the sheets prior to bonding. The insert had an area about 40 percent of the area of the sheets (see sketch (a))



(a) Laminated sheet construction.

The thermocouples were applied in two different ways in an attempt to determine whether the method of attaching the thermocouples was the cause of the temperature difference across the shadow shield sheet. Half of the thermocouples on the Schjeldahl X-850 sheets and all of those on the laminated sheets were attached in the same manner as the thermocouples in the full scale tests. The other thermocouples were laid in a bead of high thermal conductivity epoxy. This bead was also formed along an isotherm. Heaters were placed on the terminal blocks where the thermocouple leads (0.08 mm (3 mil)) from the test sheets joined 0.8-millimeter- (30-mil-) diameter facility wiring. The purpose for doing this was to determine if heat transfer along the 0.08-millimeter (3-mil) thermocouple wires would affect the thermocouple readings. The small scale testing was conducted so that the sheet temperatures approximated those of the payload

shadow shield in the full scale testing when the payload simulator was at room temperature. Additional small scale testing was done with the sheet temperatures increased by 40 to 50 percent.

The results of the small scale thermocouple tests were: (1) no temperature difference between thermocouples at the same radius was observed for the laminated Kapton sheets; (2) temperature differences across the warmer Schjeldahl X-850 sheets were about half as great as those found in the full scale tests when the thermocouples were bonded to the sheet in the same manner as the taped thermocouples in the full scale tests; (3) the temperatures for the thermocouples laid in the high thermal conductivity epoxy bead showed differences across the sheet twice as great as the taped thermocouples; (4) increasing the thermocouple junction block temperature by 55 K (100° R) had no significant effect on the thermocouple readings; (5) the temperature difference across the colder Schjeldahl X-850 sheet was generally small, but increased when the temperature of the nitrogen cooled cryoshroud was lowered; (6) increasing the sheet temperatures by 40 to 50 percent resulted in noticeable temperature differences across the warmer Kapton sheet. This temperature difference was about 8 K (15° R). A similar increase in the temperatures of the Schjeldahl X-850 shield resulted in temperature differences across the warmer sheet of about 28 K (50° R) for the epoxied thermocouples and 19 K (35° R) for the taped thermocouples. For the colder sheet the temperature differences were 17 K (30° R) and 8 K (14° R), respectively; (7) the area of the Kapton sheet containing the foil insert never showed any temperature difference; (8) placing thermocouples directly opposed to each other so that they had a common point coordinate but were on opposite sides of the sheet eliminated any temperature difference across the sheet for that pair of thermocouples. This was true for two pair of epoxied thermocouples on the Schjeldahl X-850 sheets and two pair of taped thermocouples on the Kapton sheets in an area removed from the foil.

As a consequence of the small scale test results, it appears that the choice of sheet material will influence the presence of a temperature difference across the sheet. In the case of the Schjeldahl X-850 material the Dacron scrim may have caused voids between the Mylar layers. These voids could act as very efficient insulators and be the cause of the temperature difference across the sheet. The pressure resulting from the application of the thermocouple might have locally shorted the void. This could account for the two directly opposed thermocouples measuring the same common temperature. The common point temperature was compared with readings for thermocouples on the same radius but at different circumferential positions. Since circumferential symmetry exists, all thermocouples at the same radius were expected to give the same temperature. The common point temperature was less than the temperature on the side of the sheet facing towards the heater and greater than the temperature on the side of the sheet facing away from the heater. Unfortunately, the relation between the common point temperature and temperatures on opposite sides of the sheet varied during the small

scale testing. For sheet temperatures similar to those found in the full scale testing the common point temperature was close to the temperature for the heater side of the cold sheet, and midway between the temperatures on either side of the warm sheet. If this were true in the full scale testing the analysis would be in good agreement with the experimental data. However, when the sheet temperatures increased 40 percent the common point temperature fell close to the temperatures on the side of the sheet away from the heater. If this were true in the full scale testing there would be poor agreement between the analysis and the experimental data.

REFERENCES

1. Stark, J. A.; Leonhard, K. E.; and Bennett, F. O., Jr.: Cryogenic Thermal Control Technology Summaries. (CASD-NAS-74-067, General Dynamics/Convair; NAS3-17814) NASA CR-134747, 1974.
2. Walburn, Allen B.: Development of a Reusable Flightweight Cryogenic Storage System. AIAA Paper 74-726, July 1974.
3. Keller, C. W.; Cunnington, G. R.; and Glassford, A. P.: Thermal Performance of Multilayer Insulations. (LMSC-D349866, Lockheed Missiles & Space Co.; NAS3-14377), NASA CR-134477, 1974.
4. Stochl, Robert J.: Basic Performance of a Multilayer Insulation System Containing 20 to 160 Layers. NASA TN D-7659, 1974.
5. Boyle, Robert J.; and Knoll, Richard H.: Thermal Analysis of Shadow Shields and Structural Members in a Vacuum. NASA TN D-4876, 1968.
6. Knoll, Richard H.; and Bartoo, Edward R.: Experimental Studies on Shadow Shields for Thermal Protection of Cryogenic Tanks in Space. NASA TN D-4887, 1968.
7. Boyle, Robert J.; and Stochl, Robert J.: Analytic and Experimental Evaluation of Shadow Shields and Their Support Members for Thermal Control of Space Vehicles. NASA TN D-7612, 1974.
8. Miao, David; Barber, James R.; and DeWitt, Richard L.: Design, Fabrication, and Structural Testing of a Lightweight Shadow Shield for Deep Space Application. NASA TN D-8319, 1977.
9. Knoll, Richard H.; and DeWitt, Richard L.: Thermal Performance of a Modularized Replaceable Multilayer Insulation System for a Cryogenic Stage. NASA TN D-8282, 1977.
10. Oglebay, Jon; Sagerman, Gary D.; and Valentine, Harold H.: Analytic Evaluation of Space Storeable Propellants for Unmanned Jupiter and Saturn Missions. NASA TM X-1793, 1969.
11. Bartlett, D. H.; and Zimmerman, D. K.: Space Vehicle Integrated Thermal Protection-Structural-Meteoroid Protection System. Vol. I. (D180-15172-1; Boeing Aerospace Co.; NAS3-13316) NASA CR-121103, 1973.
12. Meteoroid Environment Model, 1970: Interplanetary and Planetary NASA Space Vehicle Design Criteria (Environment). NASA SP-8038, 1970.
13. Smith, James P.: Systems Improved Numerical Differencing Analyzer (SINDA): User's Manual. (TRW-14690-H001-R0-00, TRW Systems Group; NAS9-10435) NASA CR-134271, 1971.

14. Spisz, Ernie W.; and Jack, John R.: Thermal and Radiative Property Measurements of Thermal-Control Coatings by Cyclic Radiation. NASA TN D-6316, 1971.
15. Touloukian, Y. S., ed.: Recommended Values of the Thermophysical Properties of Eight Alloys, Major Constituents and Their Oxides. NASA CR-71699, 1966.
16. Carter, J. S.; and Timberlake, T. E.: Filament-Wound, Fiberglass Cryogenic Tank Supports. (BC-8367-FR, Brunswick Corp.; NAS3-14627) NASA CR-120828, 1971.
17. Androulakis, John G.: Effective Thermal Conductivity Parallel to the Laminations of Multilayer Insulation. AIAA Paper 70-846, June-July 1970.
18. Cunnington, G. R.; Keller, C. W.; and Bell, G. A.: Thermal Performance of Multilayer Insulations. (LMSC-A903316, Lockheed Missiles & Space Co.; NAS3-12025) NASA CR-72605, 1971.
19. Santeler, Donald J.; et al.: Vacuum Technology and Space Simulation. NASA SP-105, 1967.
20. Sumner, Irving E.: Degradation of a Multilayer Insulation Due to a Seam and a Penetration. NASA TN D-8229, 1976.

TABLE I. - DEEP SPACE HEAT
TRANSFER DESIGN RATES

Source	Heat transfer rate ^a				
	W	Btu/hr	W	Btu/hr	
	H ₂ tank		F ₂ tank		
Insulation	0.016	0.056	-0.13	-0.45	
Struts	.007	.024	-.09	-.31	
Electrical wires	.002	.007	-.01	-.05	
Plumbing lines	.001	.003	-.02	-.07	
Total	.026	.09	-.26	-.88	
Allowable	Maximum	.21	.7	.41	1.4
	Minimum	-----	-----	-1.46	-5.0

^a₊ denotes heat transfer to propellant; - denotes heat transfer from propellant.

TABLE II. - HEAT TRANSFER RATE
TO HYDROGEN TANK AS A
FUNCTION OF SHADOW
SHIELD EXTERNAL EMISSIVITY

External emissivity of shield	Heat transfer rate			
	W	Btu/hr	W	Btu/hr
	With insulation		Without insulation	
Design ^a	0.026	0.09	0.571	1.95
0.1	.035	.12	.846	2.89
.3	.041	.14	.978	3.34
.6	.044	.15	1.069	3.65
.9	.044	.15	1.139	3.89

^a0.03 at room temperature.

TABLE III - INDEPENDENT VARIABLES USED IN ANALYSIS

(a) Physical dimensions

Radius, cm (in)		Thickness, cm (in)	
Payload	146 05 (57 50)	Payload ring	0.483 (0 190)
Hydrogen tank (including insulation)		Hydrogen tank ring	0.165 (0 065)
Major	114 55 (45 10)	Fluorine tank ring	0.165 (0 065)
Minor	96 01 (37 80)	Forward strut	0 124 (0 049)
Fluorine tank		Hydrogen tank strut	0.076 (0 030)
Major	91 44 (36 00)	Midstructure strut	0.107 (0 042)
Minor	65 02 (25 60)	Fluorine tank strut	0 127 (0 050)
Payload ring (to ϵ)	142 24 (56 00)	Aft strut	0.165 (0 065)
Hydrogen tank ring (to ϵ)	145 54 (57 30)	Engine strut	0.089 (0 035)
Fluorine tank ring (to ϵ)	115 56 (45 50)	Shield sheet material	1.91×10^{-3} (0.75×10^{-3})
Shield ring (to ϵ)	149 35 (58 80)	Aluminized coating	8.0×10^{-6} (3.1×10^{-6})
Shield sheet (to edge)	151 13 (59 50)	Tank insulation	1.905 (0 750)
Forward strut	2 69 (1 06)	Length, cm (in)	
Hydrogen tank strut	1 90 (0 75)	Forward strut	145.29 (57 20)
Midstructure strut	3 17 (1 25)	Hydrogen strut	55 37 (21.80)
Fluorine tank strut	2 24 (0.88)	Midstructure strut	166 12 (65.40)
Aft strut	3 17 (1 25)	Fluorine tank strut	34 54 (13.60)
Engine strut	1 90 (0 75)	Aft strut	92.71 (36.50)
Inside of shroud	198 12 (78 00)	Engine strut	113.03 (44.50)
Baffle edge	165 10 (65 00)	Area, cm ² (in ²)	
Spacing (along centerline), cm (in.)		Hydrogen tank	1.49×10^5 (23 100)
Payload to hydrogen tank	41 91 (16 50)	Fluorine tank	8.71×10^4 (13 500)
Payload to shield	20 32 (8 00)	Insulation density, layers/cm (layers/in)	17 7 (45)
Between shields	12 70 (5 00)		
Between sheets of shield	3 81 (1 50)		
Shield to tank	1 27 (0.50)		
Hydrogen tank to fluorine tank	6 35 (2 50)		

(b) Emissivity and thermal conductivity values

Property	Source	SI units ^b	U S Customary units ^c
		Temperature dependent equation	
Emissivity			
Payload surface	(a)	$0.0 + 2.57 \times 10^{-4} T$	$0.0 + 1.43 \times 10^{-4} T$
Shield - sheet exterior		$0.0 + 1.02 \times 10^{-4} T$	$0.0 + 5.65 \times 10^{-5} T$
- sheet interior		$0.0 + 2.03 \times 10^{-4} T$	$0.0 + 1.13 \times 10^{-4} T$
Insulation sheets		0.053 at 294 K	0.053 at 530 ^o R
Painted surfaces	Ref. 15	$0.748 - 2.01 \times 10^{-4} T + 2.170 \times 10^{-6} T^2$	$0.748 - 1.114 \times 10^{-4} T + 6.696 \times 10^{-7} T^2$
Thermal conductivity, W/(m)(K), (Btu/(hr)(ft²)(^oR))			
Stainless steel	Ref. 16	$-9.71 \times 10^{-2} + 1.38 \times 10^{-1} T - 4.97 \times 10^{-4} T^2 + 6.69 \times 10^{-7} T^3$	$-4.67 \times 10^{-3} + 3.69 \times 10^{-3} T - 7.38 \times 10^{-6} T^2 + 5.52 \times 10^{-9} T^3$
Fiberglass	Ref. 17	$6.80 \times 10^{-2} + 2.86 \times 10^{-3} T - 4.54 \times 10^{-6} T^2 - 1.08 \times 10^{-10} T^3$	$3.27 \times 10^{-3} + 7.64 \times 10^{-5} T - 6.75 \times 10^{-8} T^2 - 8.91 \times 10^{-13} T^3$
Insulation (lateral)	Ref. 18	$1.147 \times 10^{-2} + 1.837 \times 10^{-4} T$	$5.52 \times 10^{-4} + 4.91 \times 10^{-6} T$
Insulation (normal)	Ref. 3	See equation (1)	See equation (1)

^aMeasured at room temperature

^bTemperature in K.

^cTemperature in ^oR

TABLE IV - DESCRIPTION AND CHRONOLOGY OF THERMAL TESTS

Series	Test designation	Test condition	Area weighted payload temperature		Area weighted shroud temperature		Original recorded shroud volume on gage reading, N/m ² (torr)	Corrected shroud volume on gage reading, N/m ² (torr)	Test purpose	Duration of steady state, hr	Measured boiler rate				
			K	°R	K	°R					W	Btu/hr			
I - no shadow shields	NE-1	Near Earth	295	531	295	532	4.5 × 10 ⁻⁴ (3.4 × 10 ⁻⁵)	2.3 × 10 ⁻³ (1.7 × 10 ⁻⁵)	Baseline	14	23	5	76	9	
	NE-2	Near Earth	297	534	297	534	4.5 × 10 ⁻⁴ (3.4 × 10 ⁻⁵)	2.3 × 10 ⁻³ (1.7 × 10 ⁻⁵)	Effect of heat addition	2	27	3	93	1	
	NE-3	Near Earth	296	533	295	532	4.5 × 10 ⁻⁴ (3.4 × 10 ⁻⁵)	2.1 × 10 ⁻³ (1.6 × 10 ⁻⁵)	Repeat after heat addition	8	22	4	76	6	
	NE-4	Near Earth	294	530	295	532	2.9 × 10 ⁻⁴ (2.2 × 10 ⁻⁵)	1.5 × 10 ⁻³ (1.1 × 10 ⁻⁵)	Repeat after tank retopping	12	23	0	78	6	
	Shroud failure and repair														
	NU-1	Null		23	42	23	41	1.7 × 10 ⁻³ (1.3 × 10 ⁻⁵)	9.6 × 10 ⁻³ (7.2 × 10 ⁻⁵)	Determine effect of facility	18	0	0.41	0	14
	NS-1	Deep Space		286	516	23	42	1.3 × 10 ⁻³ (1.0 × 10 ⁻⁵)	7.9 × 10 ⁻³ (5.9 × 10 ⁻⁵)	Baseline	17	0	0.98	3	33
	NS-2	Deep Space		286	516	23	41	6.3 × 10 ⁻³ (4.7 × 10 ⁻⁵)	3.6 × 10 ⁻² (2.7 × 10 ⁻⁴)	Effect of pressure (GHe bleed)	9	1	4.4	4	93
	NS-3	Deep Space		286	516	23	41	6.1 × 10 ⁻² (1.2 × 10 ⁻⁴)	9.3 × 10 ⁻² (7.0 × 10 ⁻⁴)	Effect of pressure (GHe bleed)	21	2	18	7	46
	NE-5	Near Earth		296	533	297	534	1.6 × 10 ⁻³ (1.2 × 10 ⁻⁵)	7.5 × 10 ⁻³ (5.6 × 10 ⁻⁵)	Repeat after Deep Space	19	26	1	89	1
	NE-6	Near Earth		295	532	297	534	1.0 × 10 ⁻² (7.7 × 10 ⁻⁵)	4.9 × 10 ⁻² (3.7 × 10 ⁻⁴)	Effect of pressure (GHe bleed)	(a)	46	1	157	5
	Shields added to vehicle														
	NE-7	Near Earth		294	530	295	532	1.1 × 10 ⁻³ (8.0 × 10 ⁻⁵)	4.8 × 10 ⁻³ (3.6 × 10 ⁻⁵)	Verify hardware integrity	23	25	7	87	6
	Shroud failure and repair														
	NU-2	Null		23	41	23	41	2.3 × 10 ⁻⁴ (1.7 × 10 ⁻⁶)	1.2 × 10 ⁻³ (9.1 × 10 ⁻⁶)	Determine effect of facility	16	0	0.7	0	25
	NU-3	Null		23	42	23	41	1.7 × 10 ⁻³ (1.3 × 10 ⁻⁵)	9.2 × 10 ⁻³ (6.9 × 10 ⁻⁵)	Effect of pressure (GHe bleed)	11	08	08	27	
NU-4	Null		23	42	23	42	9.2 × 10 ⁻³ (6.9 × 10 ⁻⁵)	5.1 × 10 ⁻² (3.8 × 10 ⁻⁴)	Effect of pressure (GHe bleed)	15	12	12	41		
S-1	Deep Space		216	389	24	5	4.1 × 10 ⁻⁴ (1.1 × 10 ⁻⁶)	8.3 × 10 ⁻⁴ (6.2 × 10 ⁻⁶)	Lowered payload temperature	8	0	0.8	0	28	
S-2	Deep Space		210	451	23	5	4.2 × 10 ⁻⁴ (1.1 × 10 ⁻⁶)	1.3 × 10 ⁻³ (9.4 × 10 ⁻⁶)	Lowered payload temperature	14	09	31			
S-3	Deep Space		289	521	23	5	4.2 × 10 ⁻⁴ (2.2 × 10 ⁻⁶)	1.6 × 10 ⁻³ (1.2 × 10 ⁻⁵)	Baseline	15	11	36			
S-4	Deep Space		289	521	23	5	4.2 × 10 ⁻⁴ (1.2 × 10 ⁻⁶)	9.1 × 10 ⁻³ (6.8 × 10 ⁻⁵)	Effect of pressure (GHe bleed)	13	16	53			
S-5	Deep Space		289	520	23	5	4.2 × 10 ⁻² (8.0 × 10 ⁻⁵)	5.9 × 10 ⁻² (4.4 × 10 ⁻⁴)	Effect of pressure (GHe bleed)	11	51	1	174		
NE-5	Null		22	40	23	41	2.4 × 10 ⁻⁴ (1.8 × 10 ⁻⁶)	1.3 × 10 ⁻³ (9.9 × 10 ⁻⁶)	Repeat of test NU-2	24	08	08	26		
NE-8	Near Earth		294	529	295	531	3.7 × 10 ⁻⁴ (2.8 × 10 ⁻⁶)	1.9 × 10 ⁻³ (1.4 × 10 ⁻⁵)	Repeat after Deep Space	15	25	5	87	2	
NE-9	Near Earth		294	529	295	531	1.6 × 10 ⁻³ (1.2 × 10 ⁻⁵)	7.9 × 10 ⁻³ (5.9 × 10 ⁻⁵)	Effect of pressure (GHe bleed)	11	34	7	118	5	
NE-10	Near Earth		293	528	295	532	1.8 × 10 ⁻³ (6.1 × 10 ⁻⁵)	4.0 × 10 ⁻² (3.0 × 10 ⁻⁴)	Effect of pressure (GHe bleed)	11	80	4	274	6	
NE-11	Near Earth		294	529	295	531	1.7 × 10 ⁻⁴ (1.3 × 10 ⁻⁶)	8.7 × 10 ⁻⁴ (6.5 × 10 ⁻⁶)	Repeat of test NE-7	18	25	6	87	5	

^aShort time test, steady state not achieved for all parameters

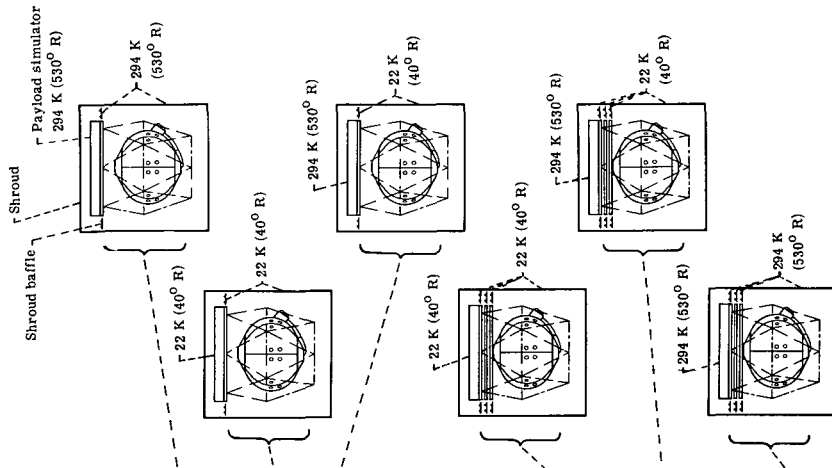


TABLE V - SUMMARY OF HEAT TRANSFER RATES FOR NEAR EARTH TESTS

Item	Heat transfer terms	Test											
		Minimum pressure - no GHe bleed					GHe bleed		No bleed		GHe bleed		No bleed
		NE-1	NE-2	NE-3	NE-4	NE-5	NE-6	NE-7	NE-8	NE-9	NE-10	NE-11	
Shroud vacuum pressure, N/m ² (torr)													
Steady state heat transfer rate, W (Btu/hr)													
1	Measured boiloff heat transfer rate	22 5 (76 9)	27 3 (93 1)	22 4 (76 6)	23 0 (78 6)	26 1 (89 1)	46 1 (157 5)	25 7 (87 6)	25 5 (87 2)	34 7 (118 5)	80 4 (274 6)	25 6 (87 5)	
	Nonflight measured heat transfer rates												
	Electric power to resistor												
	Duct	0 5 (1 6)	0 5 (1 6)	0 5 (1 6)	0 5 (1 6)	0 4 (1 3)	0 3 (1 0)	0 4 (1 3)	0 3 (1 1)	0 3 (1 1)	0 3 (1 1)	0 4 (1 2)	
	Plumbing lines and electrical wires	0 (0)	0 (0)	0 (0)	0 (0)	03 (1)	03 (1)	03 (1)	03 (1)	03 (1)	03 (1)	03 (1)	
2	Sum of nonflight heat transfer rates	5 (1 6)	4 4 (15 1)	5 (1 6)	5 (1 6)	4 (1 4)	3 (1 1)	4 (1 4)	4 (1 2)	4 (1 2)	4 (1 2)	4 (1 3)	
3	Null heat transfer rate	0 1 (0 2)	0 1 (0 2)	0 1 (0 2)	0 1 (0 2)	0 1 (0 2)	0 1 (0 3)	0 1 (0 2)	0 1 (0 2)	0 1 (0 2)	0 1 (0 2)	0 1 (0 2)	
4	Heat transfer rate to flight LH ₂ tank (items 1 - 2 - 3)	22 0 (75 1)	22 8 (77 8)	21 9 (74 8)	22 5 (76 8)	25 6 (87 5)	45 7 (156 1)	25 2 (86 0)	25 1 (85 8)	34 3 (117 1)	80 0 (273 2)	25 2 (86 0)	
	Measured noninsulation heat transfer rates												
	Struts	2 0 (6 8)	2 0 (6 8)	2 0 (6 8)	2 0 (6 8)	1 9 (6 6)	2 0 (6 9)	2 0 (6 8)	2 0 (6 8)	2 1 (7 2)	2 5 (8 6)	2 0 (6 9)	
	Electrical wires	4 (1 3)	4 (1 3)	4 (1 3)	4 (1 3)	4 (1 3)	4 (1 3)	4 (1 3)	4 (1 2)	4 (1 2)	4 (1 2)	4 (1 3)	
	Plumbing lines	4 (1 4)	4 (1 4)	4 (1 4)	2 (6)	1 (5)	2 (6)	2 (6)	1 (5)	2 (6)	1 (2)	1 (4)	
5	Sum of noninsulation heat transfer rates	2 8 (9 5)	2 8 (9 5)	2 8 (9 5)	2 5 (8 7)	2 5 (8 4)	2 6 (8 8)	2 5 (8 7)	2 5 (8 5)	2 6 (9 0)	2 9 (10 0)	2 3 (7 8)	
6	Heat transfer rate through insulation (items 4 - 5)	19 2 (65 6)	20 0 (68 3)	19 1 (65 3)	19 9 (68 1)	23 2 (79 1)	43 1 (147 3)	22 6 (77 3)	22 6 (77 3)	31 7 (108 1)	77 1 (263 2)	22 9 (78 2)	
	Measured insulation heat transfer rates												
	Plugs	2 0 (6 8)	2 0 (6 8)	2 0 (6 8)	2 0 (6 8)	1 9 (6 4)	1 8 (6 1)	1 8 (6 3)	1 7 (5 9)	1 4 (4 9)	1 2 (4 0)	1 7 (5 9)	
	Seam effect	3 9 (13 3)	3 9 (13 3)	3 9 (13 3)	3 9 (13 3)	3 9 (13 3)	8 8 (29 9)	3 9 (13 3)	3 9 (13 3)	6 4 (21 9)	15 6 (53 4)	3 9 (13 3)	
	Penetration effect	6 3 (21 6)	6 3 (21 6)	6 3 (21 6)	6 3 (21 6)	6 3 (21 6)	6 3 (21 6)	6 3 (21 6)	6 3 (21 6)	6 3 (21 6)	6 3 (21 6)	6 3 (21 6)	
7	Sum of disturbances to insulation blanket	12 2 (41 7)	12 2 (41 7)	12 2 (41 7)	12 2 (41 7)	12 1 (41 3)	16 9 (57 6)	21 1 (41 2)	11 9 (40 8)	14 2 (48 4)	23 1 (79 0)	11 9 (40 8)	
8	Blanket heat transfer rate (items 6 - 7)	7 0 (23 9)	7 8 (26 6)	6 9 (23 6)	7 7 (26 4)	11 1 (37 8)	26 3 (89 7)	10 6 (36 1)	10 7 (36 5)	17 5 (59 7)	53 9 (184 2)	11 0 (37 4)	
9	Blanket correlation (eq (1))	7 6 (25 8)	7 6 (26 0)	7 6 (25 9)	7 2 (24 7)	9 4 (32 1)	23 9 (81 5)	8 4 (28 8)	7 3 (24 8)	9 3 (31 9)	20 1 (68 5)	6 9 (23 7)	
10	Percent difference (items (8 - 9)/9 × 100)	-7 4	2 3	-8 9	6 9	17 8	10 1	25 3	47 2	87 1	168 9	57 8	

TABLE VI - INSULATION AND TANK SUPPORT STRUT TEMPERATURES FOR NEAR EARTH TESTS

(a) Insulation temperatures

Sensor	Location	Cover sheet	Layer	Test										
				NE-1	NE-2	NE-3	NE-4	NE-5	NE-6	NE-7	NE-8	NE-9	NE-10	NE-11
				Shroud vacuum pressure, N/m ² (torr)										
				1 7x10 ⁻⁵ (2 3x10 ⁻³)	1 7x10 ⁻⁵ (2 3x10 ⁻³)	1 6x10 ⁻⁵ (2 1x10 ⁻³)	1 1x10 ⁻⁵ (1 5x10 ⁻³)	5 6x10 ⁻⁵ (7 5x10 ⁻³)	3 7x10 ⁻⁴ (4 9x10 ⁻²)	3 6x10 ⁻⁵ (4 8x10 ⁻³)	1 4x10 ⁻⁵ (1 9x10 ⁻³)	5 9x10 ⁻⁵ (7 9x10 ⁻³)	3 0x10 ⁻⁴ (4 0x10 ⁻²)	6 5x10 ⁻⁶ (8 7x10 ⁻⁴)
				Temperature, K (°R)										
	Outer layer (average) ^a	Outer	34	293 (527)	293 (528)	293 (528)	292 (526)	293 (528)	292 (526)	292 (526)	291 (524)	291 (523)	288 (519)	291 (524)
HI-5	Outer blanket gore panel	Outer	34	293 (528)	293 (528)	293 (528)	293 (527)	293 (528)	292 (526)	292 (526)	292 (526)	291 (524)	289 (521)	292 (526)
HI-6	Center of panel	Inner	18	257 (462)	257 (463)	257 (463)	257 (462)	254 (458)	252 (453)	254 (458)	251 (451)	231 (415)	178 (320)	251 (451)
HI-17	Upper half - near edge	Outer	34	292 (526)	293 (527)	293 (527)	292 (526)	293 (527)	291 (524)	291 (524)	291 (523)	290 (522)	288 (518)	291 (523)
HI-18	Upper half - near edge	Inner	18	246 (443)	246 (443)	247 (444)	246 (443)	242 (435)	238 (428)	239 (431)	234 (422)	212 (381)	165 (297)	234 (422)
HI-19	Upper half - at edge	Inner	18	253 (456)	254 (457)	254 (457)	253 (456)	249 (449)	246 (443)	246 (443)	243 (437)	227 (408)	195 (351)	243 (437)
HI-20	Positioning pin cover	-----	28	278 (500)	278 (500)	278 (500)	277 (499)	278 (500)	276 (496)	275 (495)	276 (496)	273 (492)	267 (481)	276 (496)
HI-7	Inner blanket gore panel	Outer	17	252 (454)	252 (454)	252 (454)	252 (454)	-----	-----	-----	245 (441)	223 (401)	168 (303)	245 (441)
HI-8	Center of panel	Inner	1	76 (137)	77 (138)	77 (138)	76 (137)	49 (89)	29 (53)	51 (92)	43 (78)	31 (55)	28 (50)	44 (79)
HI-9	Upper half - at edge	-----	-----	104 (188)	105 (189)	105 (189)	106 (190)	92 (166)	54 (97)	89 (160)	81 (146)	47 (85)	32 (58)	84 (151)
HI-31	Lower half - on flap	-----	-----	-----	-----	-----	-----	-----	-----	27 (48)	26 (47)	25 (45)	25 (45)	27 (48)
HI-32	- at edge	-----	-----	-----	-----	-----	-----	-----	-----	37 (66)	31 (56)	27 (49)	24 (44)	32 (57)
HI-33	- near edge	-----	-----	-----	-----	-----	-----	-----	-----	40 (72)	31 (55)	22 (39)	21 (37)	31 (56)
HI-34	- middle	-----	-----	-----	-----	-----	-----	-----	-----	38 (69)	28 (51)	22 (39)	19 (35)	29 (52)
HI-22	Upper polar fiberglass cap	-----	0	144 (260)	144 (260)	145 (261)	145 (261)	136 (245)	119 (214)	-----	-----	-----	-----	-----
HI-10	Fiberglass valve box lid	-----	0	107 (193)	107 (193)	108 (194)	107 (193)	94 (170)	82 (148)	92 (166)	79 (142)	74 (134)	68 (123)	82 (148)
P-7	Fiberglass valve box side	-----	0	91 (163)	91 (164)	91 (164)	92 (165)	76 (137)	71 (127)	70 (126)	61 (110)	58 (105)	57 (103)	64 (115)

^aAverage of HI-23, HI-2, HI-1, HI-30, HI-15, HI-4, HI-16, HI-17, HI-5, HI-12, HI-13, HI-14, and HI-3

TABLE VI - Concluded

(b) Fiberglass tank support strut temperatures

Sensor	Location from tank		Test										
	cm	in	NE-1	NE-2	NE-3	NE-4	NE-5	NE-6	NE-7	NE-8	NE-9	NE-10	NE-11
			Shroud vacuum pressure, N/m ² (torr)										
			1 7x10 ⁻⁵ (2.3x10 ⁻³)	1 7x10 ⁻⁵ (2 3x10 ⁻³)	1 6x10 ⁻⁵ (2 1x10 ⁻³)	1 1x10 ⁻⁵ (1 5x10 ⁻³)	5 6x10 ⁻⁵ (7 5x10 ⁻³)	3 7x10 ⁻⁴ (4 9x10 ⁻²)	3 6x10 ⁻⁵ (4 8x10 ⁻³)	1 4x10 ⁻⁵ (1 9x10 ⁻³)	5 9x10 ⁻⁵ (7 9x10 ⁻³)	3 0x10 ⁻⁴ (4 0x10 ⁻²)	6.5x10 ⁻⁶ (8 7x10 ⁻⁴)
			Temperature, K (°R)										
HI-27	5 0	2 0	---	---	---	---	89 (160)	86 (156)	90 (162)	88 (159)	92 (166)	106 (191)	90 (161)
S-35	5 0	2 0	---	---	---	---	---	---	100 (179)	---	---	---	---
HI-26	7 3	2 9	104 (187)	104 (187)	104 (187)	104 (187)	101 (181)	99 (179)	102 (184)	99 (178)	104 (187)	121 (218)	101 (182)
HI-25	8 7	3 4	145 (262)	146 (262)	146 (262)	145 (262)	142 (255)	144 (259)	144 (260)	141 (254)	148 (267)	169 (305)	144 (259)
S-33	10 3	4 0	---	---	---	---	---	---	---	---	---	---	---
HI-24	10 6	4 2	184 (332)	185 (332)	185 (332)	184 (332)	180 (324)	182 (328)	181 (326)	178 (321)	185 (334)	206 (370)	181 (326)
S-21	10 6	4 2	(a)										
S-30	15 3	6 0	---	---	---	---	---	---	---	---	---	---	---
S-18	15 6	6 2	---	---	---	---	267 (480)	268 (482)	279 (502)	---	---	---	---
S-19	15 6	6 2	255 (459)	256 (460)	255 (460)	256 (460)	265 (476)	266 (479)	---	---	---	---	---
S-31	37 0	14 6	---	---	---	---	---	---	---	---	---	---	---
S-20	54 2	21 3	(a)										
S-17	54 2	21 3	295 (532)	295 (532)	295 (532)	295 (531)	295 (531)	294 (528)	294 (530)	294 (530)	294 (530)	295 (531)	294 (530)
S-34	54 2	21 3	---	---	---	---	---	---	---	---	---	---	---
S-32	54 2	21 3	---	---	---	---	---	---	---	---	---	---	---
S-16	59 3	23 3	295 (530)	295 (531)	295 (531)	295 (531)	295 (532)	294 (529)	294 (530)	294 (529)	294 (530)	295 (531)	294 (529)

^aNot operative

TABLE VII - TRUSS STRUCTURE AND TANK SUPPORT STRUT TEMPERATURES FOR DEEP SPACE TESTS

Sensor	Sensor location	Measurement path (reference)	Distance from reference		No shields			Shadow shields				
					Test							
			cm	in	NS-1	NS-2	NS-3	S-1	S-2	S-3	S-4	S-5
			Payload simulator temperature, K (°R)									
			287 (516)	287 (516)	287 (516)	216 (389)	251 (451)	289 (521)	289 (521)	289 (520)		
Shroud vacuum pressure, N/m ² (torr)												
7.9 × 10 ⁻³ (5.9 × 10 ⁻⁵)	3.6 × 10 ⁻² (2.7 × 10 ⁻⁴)	9.3 × 10 ⁻² (7.0 × 10 ⁻⁴)	8.3 × 10 ⁻⁴ (6.2 × 10 ⁻⁶)	1.3 × 10 ⁻³ (9.4 × 10 ⁻⁶)	1.6 × 10 ⁻³ (1.2 × 10 ⁻⁵)	9.1 × 10 ⁻³ (6.8 × 10 ⁻⁵)	5.9 × 10 ⁻² (4.4 × 10 ⁻⁴)					
Temperature, K (°R)												
FSR-3	Payload simulator ring	Along ring (reference is junction of pair of struts)	9 7	3 8	218 (392)	216 (388)	213 (384)	192 (345)	220 (396)	249 (449)	248 (447)	244 (440)
FSR-2			10 2	4 0	219 (394)	217 (391)	215 (387)	193 (347)	222 (399)	252 (453)	251 (452)	247 (445)
FSR-1			71 1	28 0	248 (447)	247 (445)	246 (442)	206 (370)	238 (429)	272 (489)	271 (488)	268 (483)
FSR-4			71 9	28 3	230 (414)	228 (410)	225 (405)	193 (348)	222 (399)	252 (454)	251 (452)	246 (443)
FSR-5			73 2	28 8	229 (412)	226 (407)	223 (401)	193 (347)	221 (397)	251 (451)	249 (449)	243 (438)
S-1	Forward struts	Along structure from payload (reference is payload simulator)	8 4	3 3	216 (389)	215 (387)	213 (384)	187 (337)	214 (385)	243 (437)	242 (436)	238 (429)
S-2			13 5	5 3	193 (347)	191 (344)	189 (341)	171 (307)	193 (347)	217 (391)	217 (390)	212 (381)
S-3			13 5	5 3	189 (340)	187 (337)	185 (333)	169 (305)	193 (347)	217 (390)	216 (388)	211 (380)
S-4			18 5	7 3	174 (313)	172 (309)	169 (305)	156 (280)	175 (315)	196 (353)	195 (351)	189 (340)
S-5			24 1	9 5	156 (281)	153 (276)	151 (272)	137 (247)	153 (275)	171 (308)	169 (304)	161 (289)
S-6			33 8	13 3	141 (254)	138 (249)	136 (245)	121 (217)	132 (238)	146 (262)	143 (257)	132 (238)
S-8			43 2	17 0	130 (234)	127 (228)	124 (223)	103 (185)	111 (200)	120 (216)	116 (209)	103 (185)
S-7			84 6	33 3	108 (195)	103 (185)	99 (178)	73 (132)	76 (137)	79 (143)	74 (134)	58 (104)
S-9			84 6	33 3	109 (196)	103 (186)	99 (179)	72 (130)	75 (135)	78 (141)	73 (132)	56 (101)
S-10			148 1	58 3	91 (163)	81 (146)	74 (133)	48 (86)	49 (88)	50 (90)	42 (76)	38 (68)
S-11			148 1	58 3	90 (162)	81 (145)	73 (132)	57 (102)	57 (103)	58 (105)	52 (93)	38 (69)
S-12			148 1	58 3	90 (162)	80 (144)	73 (131)	56 (101)	57 (103)	58 (104)	52 (93)	38 (69)
S-13	Hydrogen tank ring	Along structure from payload (reference is payload simulator)	155 4	61 2	88 (158)	78 (140)	70 (126)	46 (82)	47 (84)	48 (86)	41 (74)	30 (54)
S-14			155 4	61 2	93 (167)	83 (150)	76 (136)	43 (77)	44 (79)	45 (81)	38 (68)	31 (55)
S-15	Midstructure struts	Along structure from payload (reference is payload simulator)	158 7	62 5	87 (157)	77 (139)	69 (125)	45 (81)	46 (83)	47 (85)	40 (72)	31 (55)
S-26			158 7	62 5	89 (160)	79 (143)	72 (129)	47 (85)	48 (86)	48 (87)	42 (75)	33 (60)
S-22			242 6	95 5	57 (103)	41 (74)	34 (62)	37 (67)	38 (68)	37 (67)	28 (51)	25 (45)
S-23			242 6	95 5	56 (101)	39 (71)	34 (61)	36 (65)	37 (66)	36 (65)	29 (52)	25 (45)
S-37			243 8	96 0	-----	-----	-----	37 (66)	38 (68)	38 (69)	32 (58)	29 (52)
S-36			307 3	121 0	-----	-----	-----	33 (59)	34 (61)	34 (61)	27 (48)	25 (45)
S-38			307 3	121 0	-----	-----	-----	32 (58)	33 (60)	33 (60)	27 (49)	25 (45)
S-24			318 8	125 5	47 (84)	29 (52)	26 (47)	34 (62)	35 (63)	34 (62)	27 (48)	24 (44)
S-25			318 8	125 5	44 (79)	28 (50)	25 (45)	36 (65)	37 (66)	35 (63)	28 (53)	28 (50)
HI-27			Fiberglass tank support struts	Along structure from tank (reference is tank surface)	5 0	2 0	24 (43)	24 (43)	25 (45)	25 (45)	25 (45)	25 (45)
HI-26	7 3	2 9			26 (47)	26 (47)	27 (49)	26 (47)	26 (46)	26 (46)	26 (46)	26 (47)
HI-25	8 7	3 4			27 (48)	27 (48)	28 (50)	23 (42)	23 (41)	23 (42)	23 (41)	24 (43)
S-33	10 3	4 0			-----	-----	-----	28 (50)	28 (50)	28 (50)	28 (50)	28 (51)
HI-24	10 6	4 2			30 (54)	28 (51)	30 (54)	23 (42)	23 (42)	23 (42)	23 (41)	24 (43)
S-21	10 6	4 2			-----	-----	-----	22 (40)	22 (40)	22 (40)	22 (40)	23 (41)
S-30	15 3	6 0			-----	-----	-----	29 (53)	29 (53)	29 (53)	28 (50)	28 (51)
S-18	15 6	6 2			48 (86)	-----	42 (75)	-----	-----	-----	-----	-----
S-19	15 6	6 2			44 (80)	40 (72)	40 (72)	31 (55)	31 (55)	31 (55)	28 (50)	28 (50)
S-31	37 0	14 6			-----	-----	-----	36 (65)	37 (66)	37 (67)	32 (57)	28 (50)
S-20	54 2	21 3			-----	-----	-----	39 (70)	40 (72)	42 (75)	36 (64)	29 (52)
S-17	54 2	21 3			85 (153)	74 (133)	65 (117)	39 (70)	39 (71)	42 (75)	35 (63)	28 (50)
S-34	54 2	21 3			-----	-----	-----	42 (75)	42 (76)	44 (79)	38 (68)	32 (57)
S-32	54 2	21 3			-----	-----	-----	42 (75)	42 (76)	44 (79)	37 (67)	31 (55)
S-16	59 3	23 3			87 (156)	76 (137)	68 (122)	42 (75)	43 (77)	45 (81)	38 (69)	28 (51)

TABLE VIII - INSULATION TEMPERATURES FOR DEEP SPACE TESTS

Sensor	Location	Hemi-sphere	Layer	Radial position		No shields					Shadow shields				
				cm	in	NS-1	NS-2	NS-3	S-1	S-2	S-3	S-4	S-5		
														Payload simulator temperature, K (°R)	
						287 (516)	287 (516)	216 (389)	251 (451)	289 (521)	289 (521)	289 (521)	289 (521)	289 (521)	289 (521)
						Shroud vacuum pressure, N/m ² (torr)									
						7.9 × 10 ⁻³ (5.9 × 10 ⁻⁵)	3.6 × 10 ⁻² (2.7 × 10 ⁻⁴)	9.3 × 10 ⁻² (7.0 × 10 ⁻⁴)	8.3 × 10 ⁻⁴ (6.2 × 10 ⁻⁶)	1.3 × 10 ⁻³ (9.4 × 10 ⁻⁶)	1.6 × 10 ⁻³ (1.2 × 10 ⁻⁵)	1.6 × 10 ⁻³ (1.2 × 10 ⁻⁵)	9.1 × 10 ⁻³ (6.8 × 10 ⁻⁵)	5.9 × 10 ⁻² (4.4 × 10 ⁻⁴)	
						Insulation temperature, K (°R)									
HI-23	Outer cover - outer blanket	Top	34	0 0	159 (287)	159 (286)	159 (286)	159 (286)	39 (70)	41 (74)	47 (84)	47 (84)	53 (95)	69 (124)	
HI-2				36.6 14 4	147 (264)	146 (262)	145 (261)	145 (261)	38 (68)	40 (72)	45 (81)	45 (81)	47 (84)	57 (102)	
HI-1				61 7 24 3	128 (230)	126 (227)	126 (227)	126 (227)	35 (63)	37 (66)	40 (72)	40 (72)	41 (74)	49 (88)	
HI-30				61 7 24 3					38 (68)	39 (71)	42 (76)	42 (76)	43 (78)	50 (90)	
HI-3				61 7 24 3					34 (61)	36 (64)	39 (71)	39 (71)			
HI-15				82 8 32 6	119 (215)	117 (210)	116 (209)	116 (209)	38 (68)	39 (71)	43 (78)	43 (78)	42 (75)	45 (81)	
HI-4				99 3 39 1	99 (178)	95 (171)	93 (167)	93 (167)	36 (64)	37 (66)	39 (71)	39 (71)	36 (65)	36 (65)	
HI-16				110.5 43 5	79 (143)	72 (130)	70 (126)	70 (126)	33 (60)	34 (62)	37 (66)	37 (66)	33 (59)	31 (56)	
HI-17				110 5 43 5	75 (135)	71 (127)	69 (124)	69 (124)	33 (59)	33 (60)	36 (64)	36 (64)	33 (59)	33 (59)	
HI-5				114.6 45 1	67 (121)	58 (104)	55 (99)	55 (99)	32 (57)	32 (58)	33 (60)	33 (60)	30 (54)	28 (50)	
HI-12		Bottom	34	99 3 39 1	36 (64)	33 (60)	34 (61)	34 (61)							
HI-13				57 9 22 8	28 (51)	28 (51)	29 (52)	29 (52)	27 (49)	27 (49)	27 (48)	27 (48)	26 (46)	25 (45)	
HI-14				27 4 10 8	26 (47)	26 (47)	27 (48)	27 (48)	23 (41)	23 (41)	22 (40)	22 (40)	22 (40)	22 (40)	
HI-20	Positioning pin cover	Top	28	114 6 45 1	50 (90)	43 (78)	43 (77)	43 (77)	28 (50)	28 (51)	29 (53)	29 (53)	27 (48)	26 (47)	
HI-6	Inner cover - outer blanket	Top	18	114 6 45 1	42 (75)	38 (68)	37 (66)	37 (66)	26 (47)	26 (47)	27 (48)	27 (48)	27 (48)	25 (45)	
HI-18				110 5 43 5	52 (93)	48 (86)	46 (83)	46 (83)	26 (46)	26 (47)	27 (48)	27 (48)	27 (48)	27 (48)	
HI-19				110 5 43.5	53 (95)	50 (90)	49 (89)	49 (89)	26 (47)	27 (48)	28 (50)	28 (50)	27 (49)	28 (50)	
HI-7	Outer cover - inner blanket	Top	17	114 6 45.1					24 (44)	25 (45)	26 (46)	26 (46)	25 (45)	23 (42)	
(a)	Inner cover - inner blanket	-----	1	-----	24 (43)	24 (43)	24 (43)	24 (43)	22 (40)	22 (40)	22 (39)	22 (39)	21 (38)	21 (38)	
HI-22	Upper polar cap	Top	0	0 0	45 (81)	37 (67)	33 (59)	33 (59)							
HI-10	Valve box lid	Bottom	0	-----	24 (43)	24 (43)	23 (42)	23 (42)	22 (40)	22 (40)	22 (40)	22 (40)	22 (39)	22 (39)	
P-7	Valve box side	-----	0	-----	23 (42)	23 (42)	23 (42)	23 (42)	22 (40)	22 (40)	22 (40)	22 (40)	22 (40)	22 (40)	

^aAverage value

TABLE IX. - SHEET AND RING TEMPERATURES FOR DEEP SPACE TESTS WITH SHADOW SHIELDS

Sensor	Shield	Sheet	Location	Radius		Test						
				cm	in.	S-1	S-2	S-3	S-4	S-5		
						Payload simulator temperature, K (^o R)						
						216 (389)	251 (451)	289 (521)	289 (521)	289 (520)		
						Shroud vacuum pressure, N/m ² (torr)						
						8.3×10 ⁻⁴ (6.2×10 ⁻⁶)	1.3×10 ⁻³ (9.4×10 ⁻⁶)	1.6×10 ⁻³ (1.2×10 ⁻⁵)	9.1×10 ⁻³ (6.8×10 ⁻⁵)	5.9×10 ⁻² (4.4×10 ⁻⁴)		
						Temperature, K (^o R)						
PS-1	Payload	Warm	Outside	0.0	0.0	152 (273)	178 (320)	208 (375)	209 (376)	210 (378)		
PS-2			Outside	61.0	24.0	151 (271)	177 (319)	207 (373)	208 (374)	208 (375)		
PS-11			Inside	61.0	24.0	142 (255)	166 (298)	195 (351)	196 (352)	199 (358)		
PS-3			Outside	106.7	42.0	141 (254)	-----	-----	-----	-----		
PS-4			Outside	137.2	54.0	138 (248)	161 (289)	186 (335)	183 (330)	171 (308)		
PS-9		Cold	Outside	0.0	0.0	119 (215)	136 (245)	157 (282)	156 (280)	158 (284)		
PS-8			Outside	61.0	24.0	118 (213)	135 (243)	156 (280)	154 (277)	154 (278)		
PS-12			Inside	61.0	24.0	127 (228)	146 (262)	168 (303)	165 (297)	161 (289)		
PS-7			Outside	106.7	42.0	117 (210)	133 (239)	151 (272)	148 (266)	143 (257)		
PS-13			Inside	106.7	42.0	123 (222)	142 (255)	163 (294)	158 (285)	148 (267)		
PS-6			Outside	137.2	54.0	114 (205)	129 (233)	147 (264)	139 (251)	120 (216)		
PS-5			Payload shield ring			148.1	58.3	118 (212)	132 (238)	149 (269)	147 (264)	134 (242)
PS-10						148.1	58.3	118 (212)	132 (238)	149 (269)	147 (264)	133 (240)
TS-1	Tank	Warm	Outside	0.0	0.0	84 (151)	93 (167)	103 (185)	105 (189)	114 (205)		
TS-2			Outside	61.0	24.0	84 (152)	93 (167)	103 (186)	103 (186)	107 (193)		
TS-3			Outside	106.7	42.0	84 (151)	91 (163)	102 (183)	98 (176)	96 (172)		
TS-4			Outside	137.2	54.0	83 (150)	90 (162)	99 (178)	89 (160)	77 (138)		
TS-9			Cold	Outside	0.0	0.0	73 (131)	77 (139)	84 (151)	78 (141)	89 (160)	
TS-8		Outside		61.0	24.0	76 (136)	79 (143)	87 (156)	72 (130)	77 (139)		
TS-10		Inside		61.0	24.0	74 (134)	77 (138)	84 (152)	71 (128)	78 (140)		
TS-7		Outside		106.7	42.0	77 (139)	80 (144)	87 (157)	68 (123)	68 (123)		
TS-6		Outside		137.2	54.0	74 (134)	76 (137)	82 (148)	60 (108)	56 (100)		
TS-5		Tank shield ring			148.1	58.3	87 (157)	93 (167)	99 (179)	94 (169)	72 (130)	
TS-11					148.1	58.3	87 (156)	92 (166)	99 (178)	93 (168)	71 (127)	

TABLE X - SUMMARY OF HEAT TRANSFER RATES FOR DEEP SPACE TESTS

Item	Heat transfer terms										
	Test										
	NS-1	NS-2	NS-3	S-1	S-2	S-3	S-4	S-5	Payload simulator temperature, K (°R)		
	287 (516)	287 (516)	287 (516)	216 (389)	251 (451)	289 (521)	289 (521)	289 (521)	289 (521)	289 (520)	
	Shroud vacuum pressure, N/m ² (torr)										
	7.9 × 10 ⁻³ (5.9 × 10 ⁻⁵)	3.6 × 10 ⁻² (2.7 × 10 ⁻⁴)	9.3 × 10 ⁻² (7.0 × 10 ⁻⁴)	8.3 × 10 ⁻⁴ (6.2 × 10 ⁻⁶)	1.3 × 10 ⁻³ (9.4 × 10 ⁻⁶)	1.6 × 10 ⁻³ (1.2 × 10 ⁻⁵)	9.1 × 10 ⁻³ (6.8 × 10 ⁻⁵)	9.1 × 10 ⁻³ (6.8 × 10 ⁻⁵)	5.9 × 10 ⁻² (4.4 × 10 ⁻⁴)		
	Steady state heat transfer rate, W (Btu/hr)										
1	0.98 (3.33)	1.44 (4.93)	2.18 (7.46)	0.08 (0.28)	0.09 (0.31)	0.11 (0.36)	0.16 (0.53)	0.16 (0.53)	0.51 (1.74)		
	Nonflight measured heat transfer rates										
	Duct										
	0.01 (0.03)	0.01 (0.03)	0.01 (0.02)	0.01 (0.02)	0.01 (0.02)	0.01 (0.02)	0.01 (0.02)	0.01 (0.02)	0.01 (0.02)	0.01 (0.02)	
	Plumbing lines and electrical wires ^a										
	0	0	0	0	0	0	0	0	0	0	
2	0.01 (0.03)	0.01 (0.03)	0.01 (0.02)	0.01 (0.02)	0.01 (0.02)	0.01 (0.02)	0.01 (0.02)	0.01 (0.02)	0.01 (0.02)	0.01 (0.02)	
3	0.07 (0.25)	0.09 (0.32)	0.13 (0.45)	0.07 (0.23)	0.07 (0.23)	0.07 (0.23)	0.07 (0.23)	0.07 (0.23)	0.11 (0.37)		
4	0.89 (3.05)	1.34 (4.58)	2.05 (6.99)	0.01 (0.03)	0.02 (0.06)	0.03 (0.11)	0.08 (0.26)	0.08 (0.26)	0.40 (1.35)		
	Measured noninsulation heat transfer rates										
	Struts										
	0.06 (0.21)	0.04 (0.13)	0.04 (0.13)	0.01 (0.05)	0.01 (0.05)	0.01 (0.05)	0.01 (0.05)	0.01 (0.05)	0.01 (0.03)		
	Electrical wires										
	0.04 (0.13)	0.03 (0.11)	0.03 (0.11)	0.01 (0.03)	0.01 (0.03)	0.01 (0.03)	0.01 (0.03)	0.01 (0.03)	0.01 (0.03)		
	Plumbing lines										
	0.01 (0.02)	0.01 (0.02)	0.01 (0.02)	0	0	0	0	0	0		
5	0.11 (0.36)	0.08 (0.26)	0.08 (0.26)	0.02 (0.08)	0.02 (0.08)	0.02 (0.08)	0.02 (0.08)	0.02 (0.08)	0.02 (0.08)		
6	0.79 (2.69)	1.27 (4.32)	1.97 (6.73)	-0.01 (-0.05)	-0.01 (-0.02)	0.01 (0.03)	0.05 (0.18)	0.05 (0.18)	0.37 (1.27)		
	Insulation disturbance heat transfer rates										
	Pins										
	0.12 (0.41)	0.10 (0.34)	0.09 (0.32)	0.01 (0.05)	0.01 (0.05)	0.02 (0.06)	0.01 (0.05)	0.01 (0.05)	0.02 (0.06)		
	Seam effect										
	0.08 (0.26)	0.13 (0.44)	0.20 (0.68)								
	Penetration effect										
	0.20 (0.67)	0.23 (0.78)	0.29 (1.00)	0.01 (0.05)	0.01 (0.05)	0.02 (0.06)	0.01 (0.05)	0.01 (0.05)	0.02 (0.06)		
7											
8	0.59 (2.02)	1.04 (3.54)	1.68 (5.73)	-0.03 (-0.10)	-0.02 (-0.07)	-0.01 (-0.03)	0.04 (0.13)	0.04 (0.13)	0.35 (1.21)		
9	1.22 (4.18)	3.96 (13.53)	8.36 (28.55)	0.04 (0.15)	0.06 (0.22)	0.09 (0.30)	0.33 (1.11)	0.33 (1.11)	1.83 (6.24)		
10	-51.7	-73.8	-79.9								

^a0 entries are for measured values less than 0.001 W (0.005 Btu/hr)

Page intentionally left blank

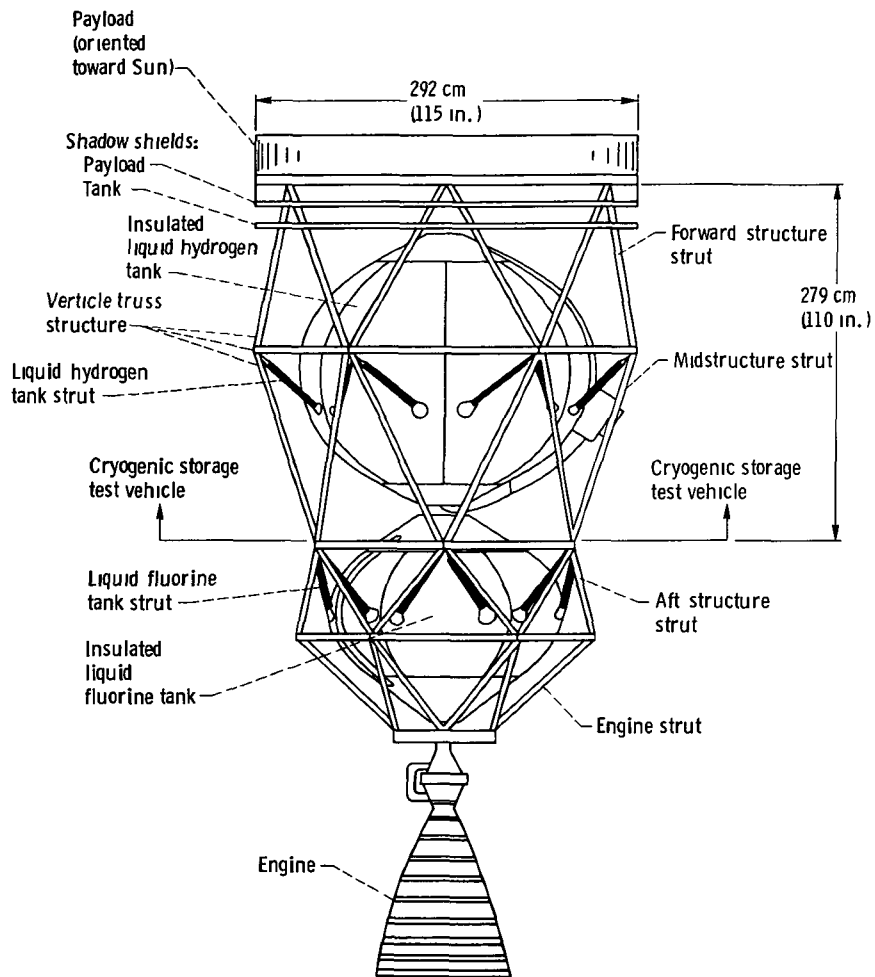


Figure 1. - Conceptual design of hydrogen fluorine rocket stage.

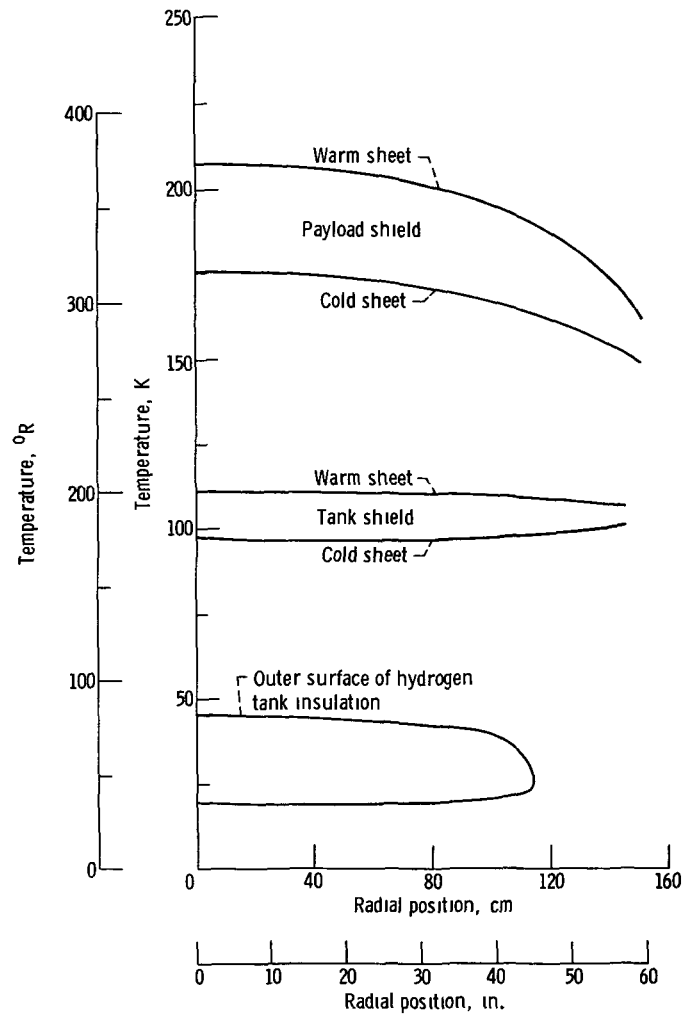


Figure 2. - Temperature profiles for shadow shield sheets and outer surface of hydrogen tank insulation.

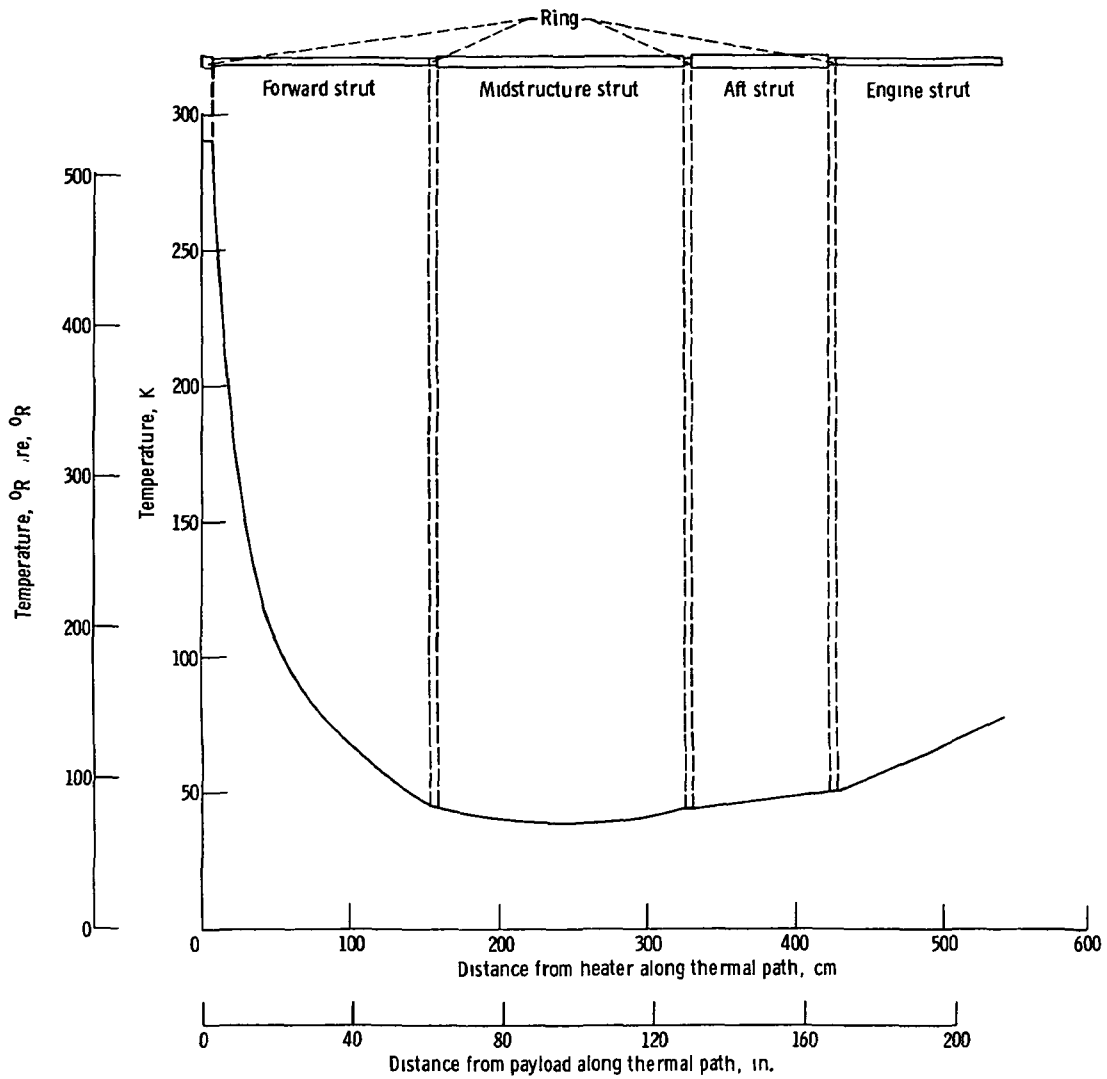
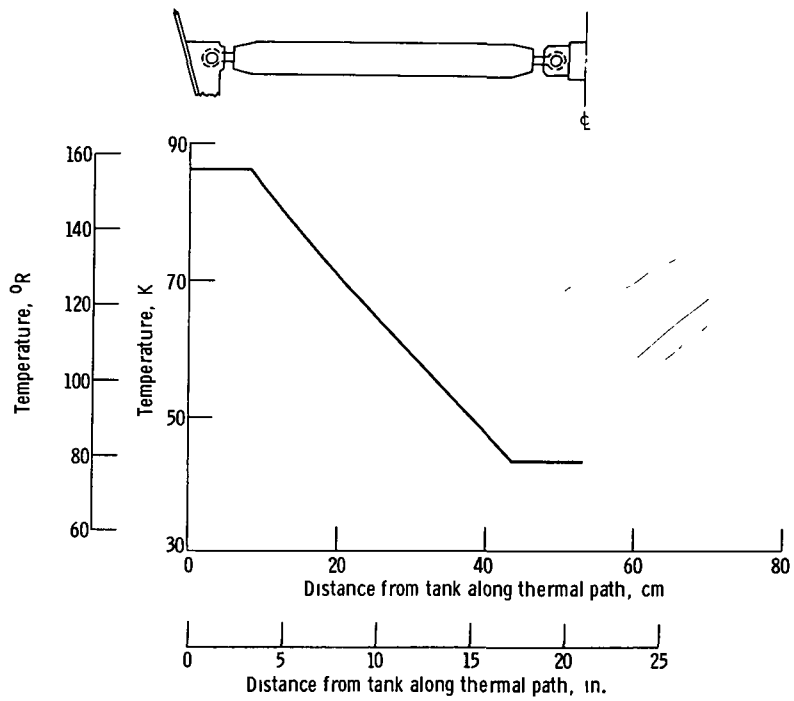
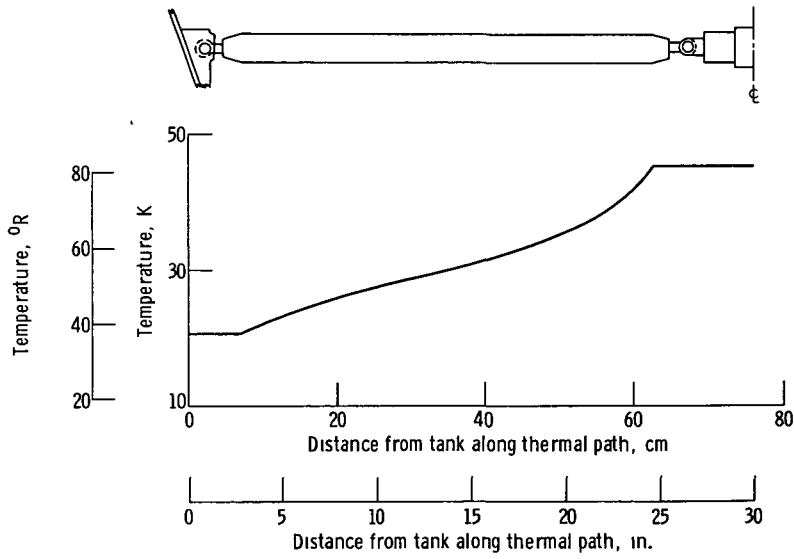


Figure 3. - Temperature profile for hydrogen-fluorine stage truss structure



(a) Fluorine strut.



(b) Hydrogen strut

Figure 4 - Temperature profiles for hydrogen-fluorine stage tank supports.

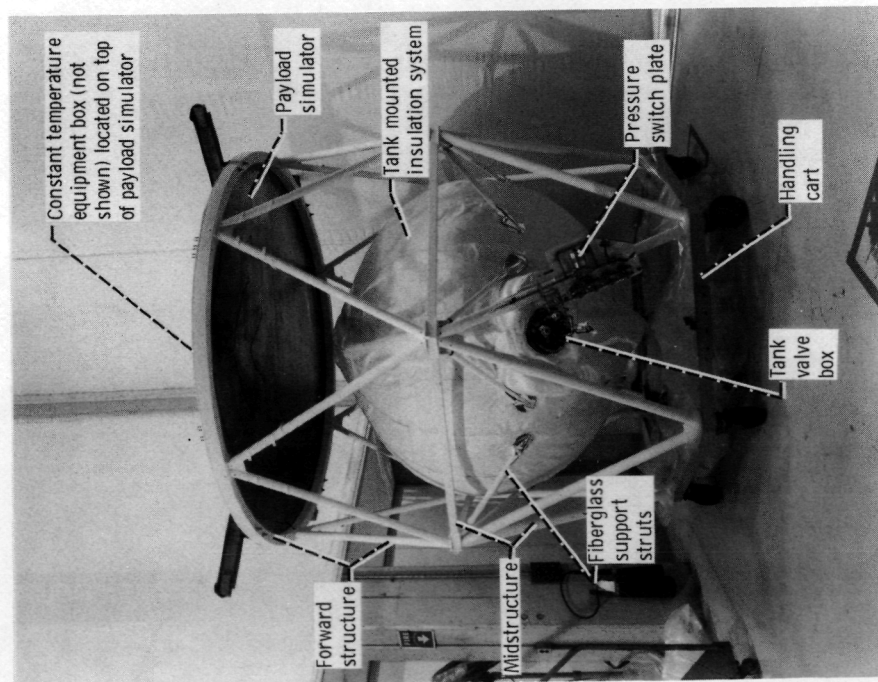
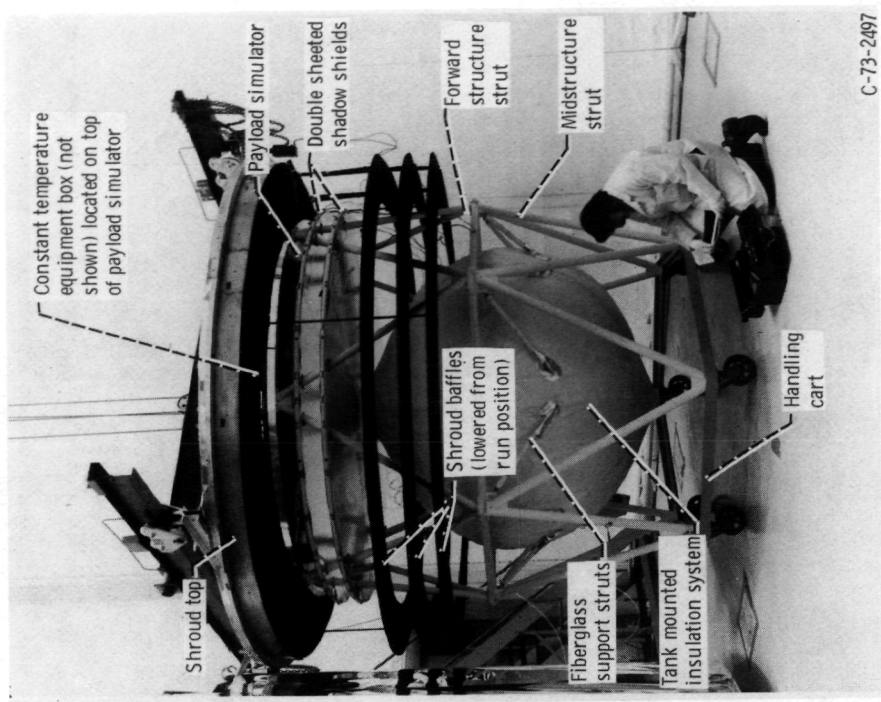


Figure 5. - Insulated hydrogen tank test configuration.



C-73-2497

Figure 6. - Hydrogen tank integrated thermal protection system test configuration.

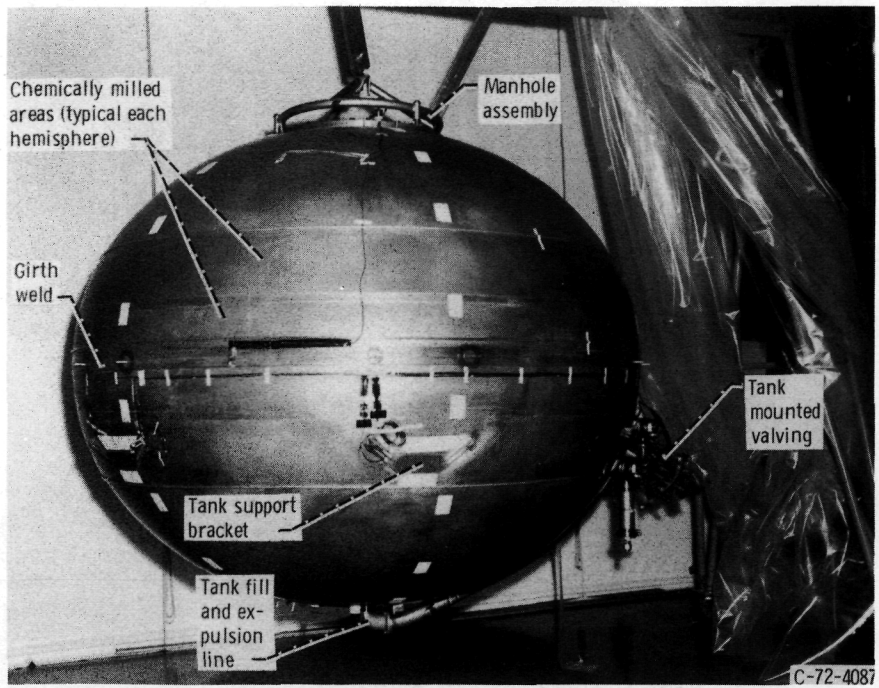


Figure 7. - Liquid hydrogen tank prior to application of multi layer insulation.

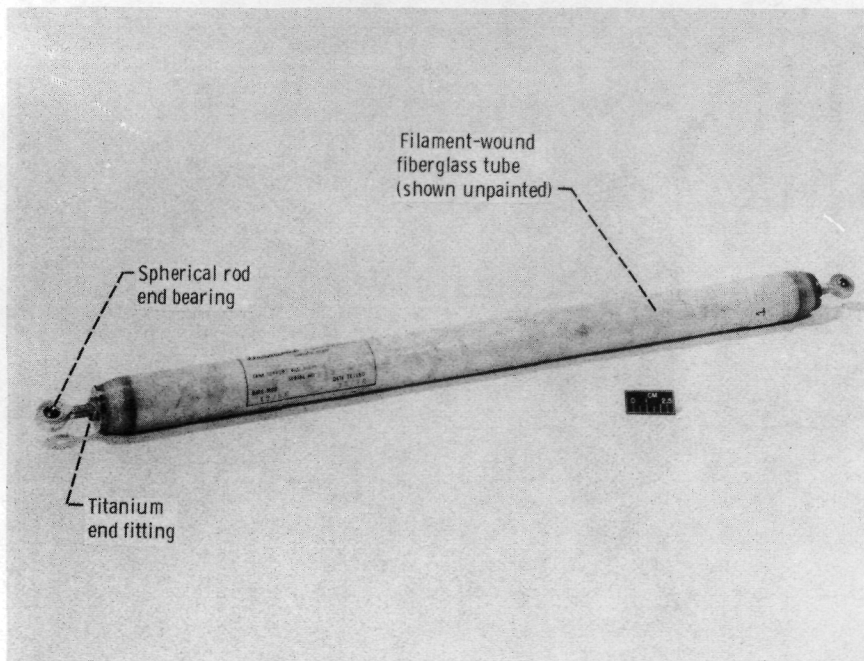


Figure 8. - LH₂ tank fiberglass support strut.

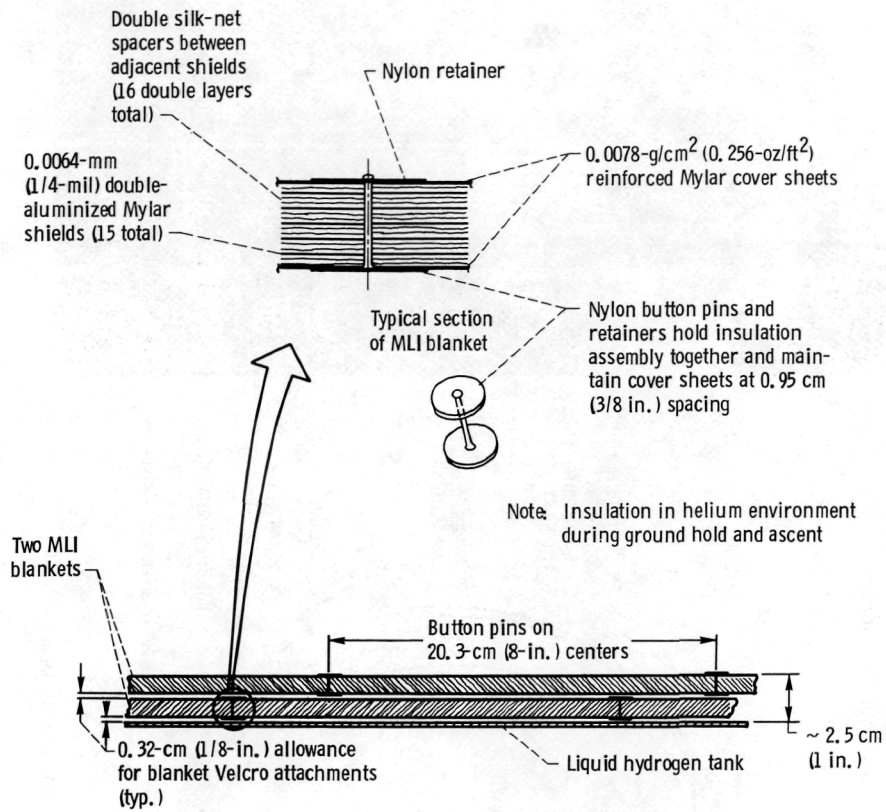


Figure 9. - Basic concept of multilayer insulation.

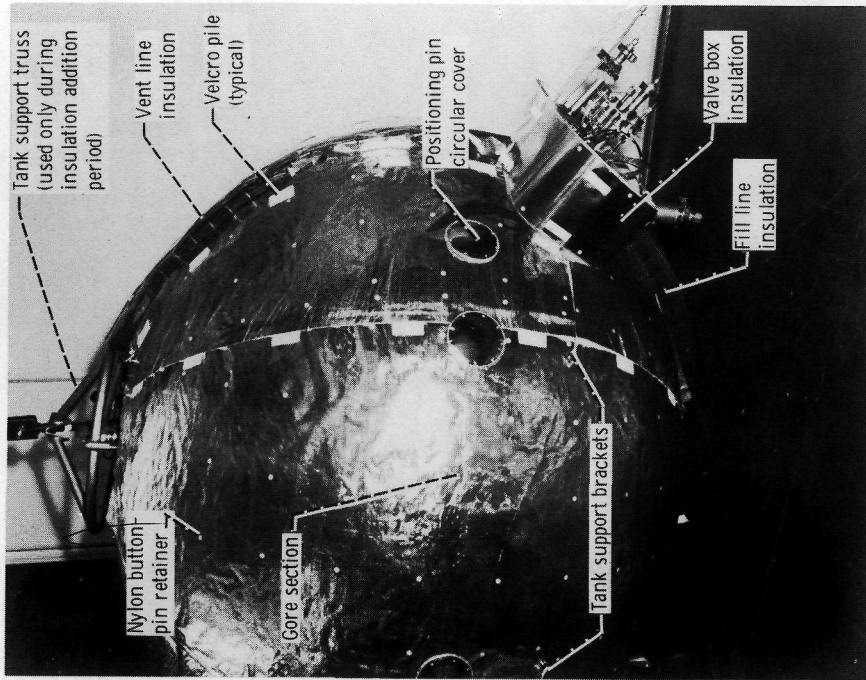


Figure 11. - LH₂ tank during insulation application.

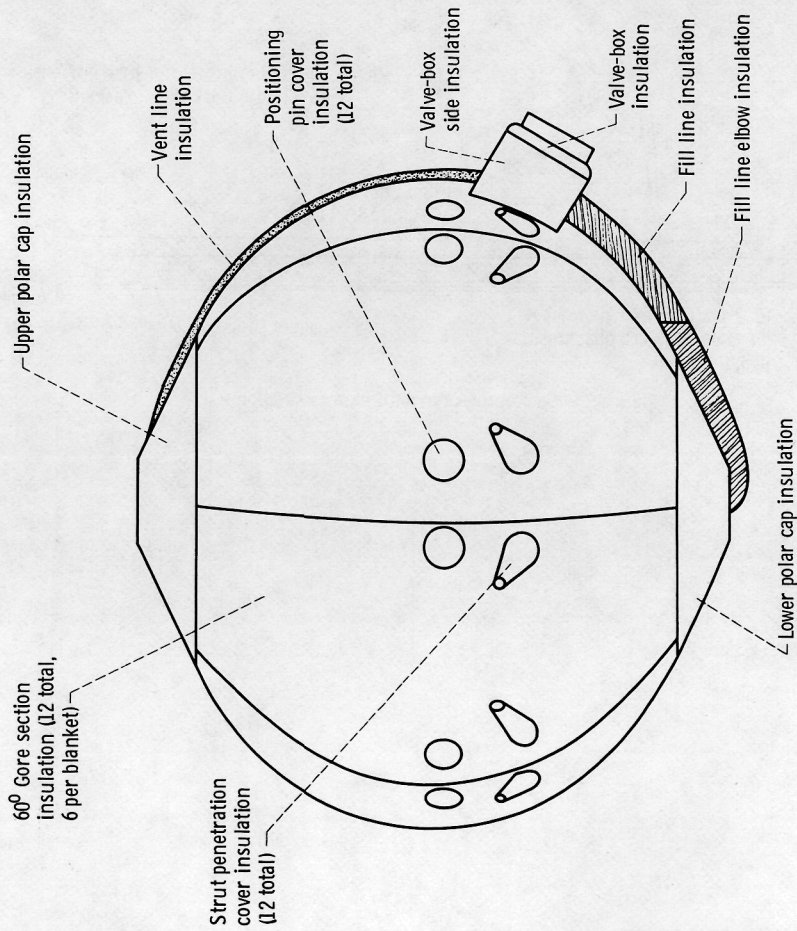
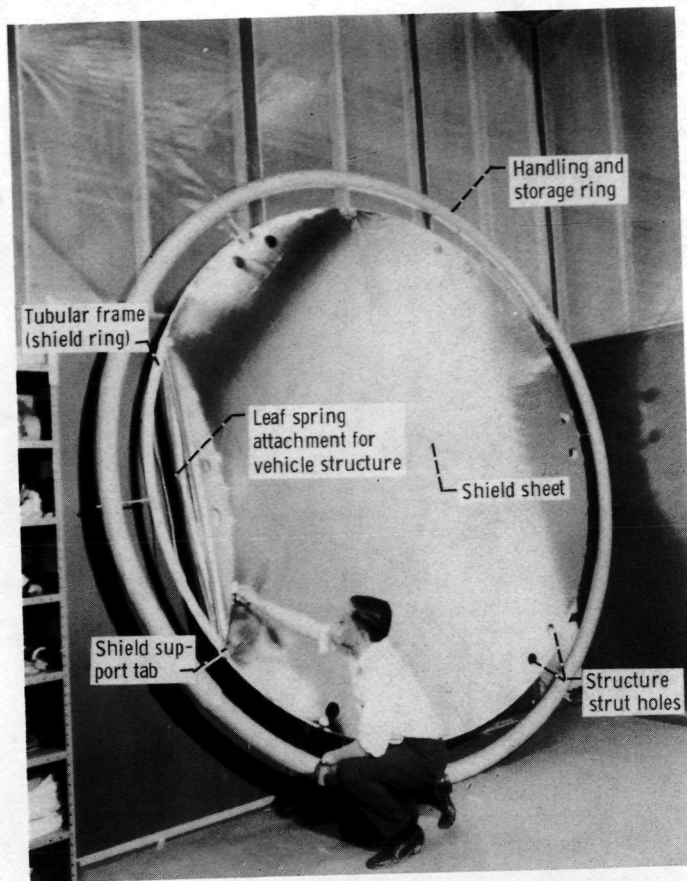
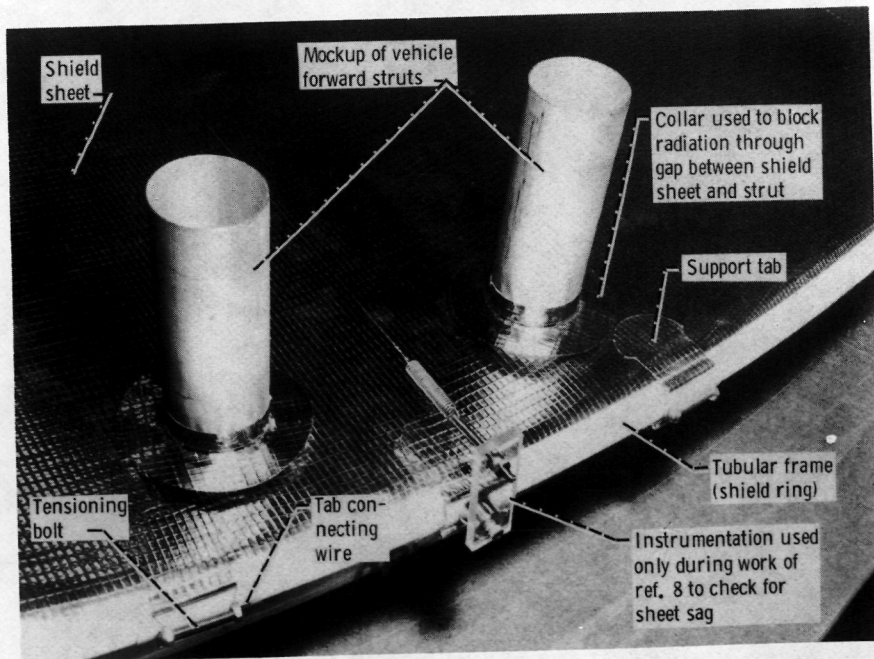


Figure 10. - Schematic of modular insulation system for LH₂ tank.



(a) Overall view of completed unit.



(b) Details of sheet-to-frame connections and structure strut penetrations.
 Figure 12. - Double sheeted shadow shield.

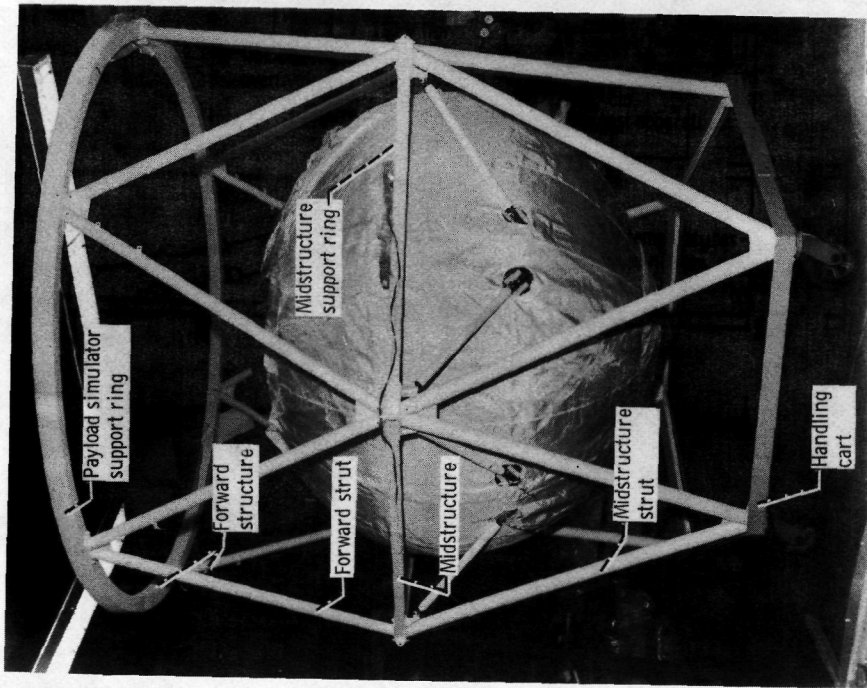
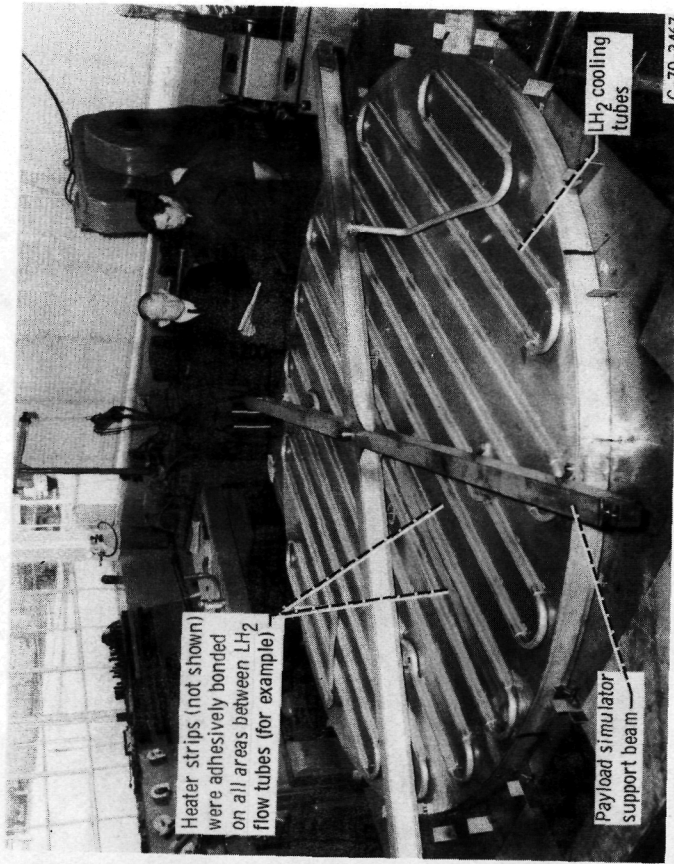


Figure 13. - Open-truss-type vehicle structure with insulated liquid hydrogen tank installed.

C-73-794



C-70-3467

Figure 14. - View of top surface of payload simulator during fabrication.

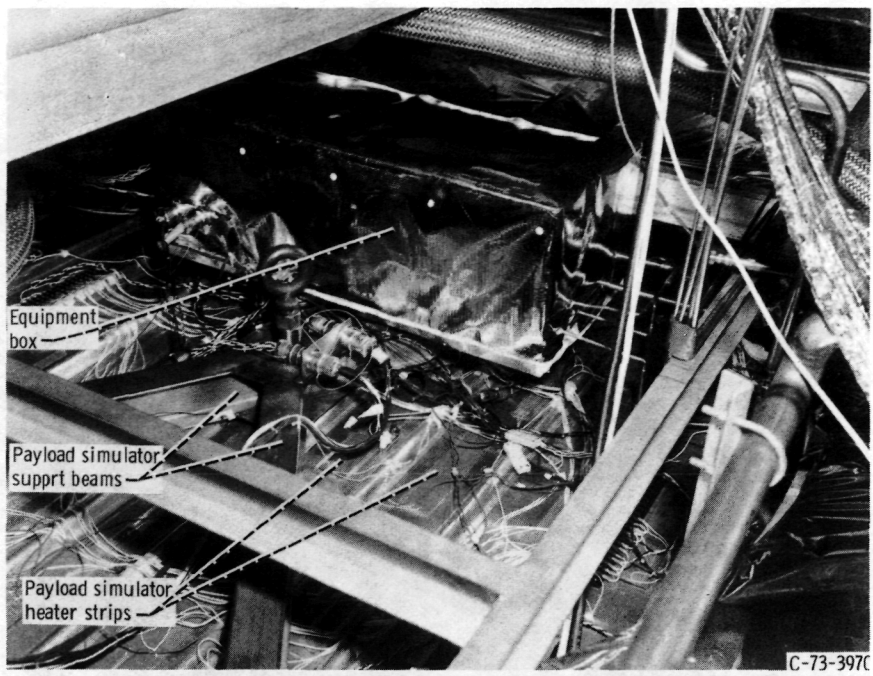


Figure 15. - Insulated equipment box mounted on top of payload simulator.

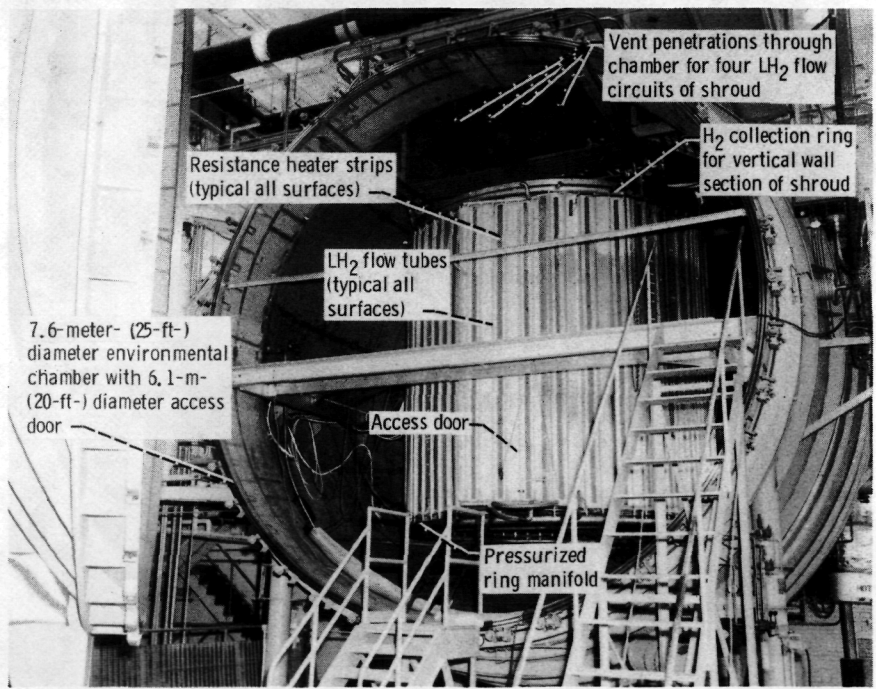


Figure 16. - 7.6-Meter- (13-ft-) diameter shroud mounted within spherical vacuum chamber.

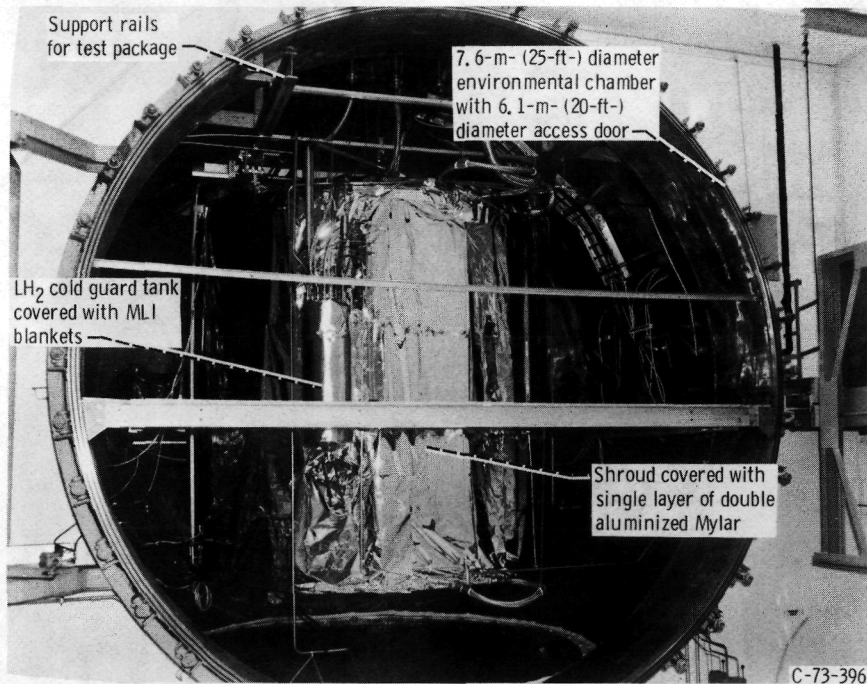


Figure 17. - LH₂ cold guard mounted on shroud.

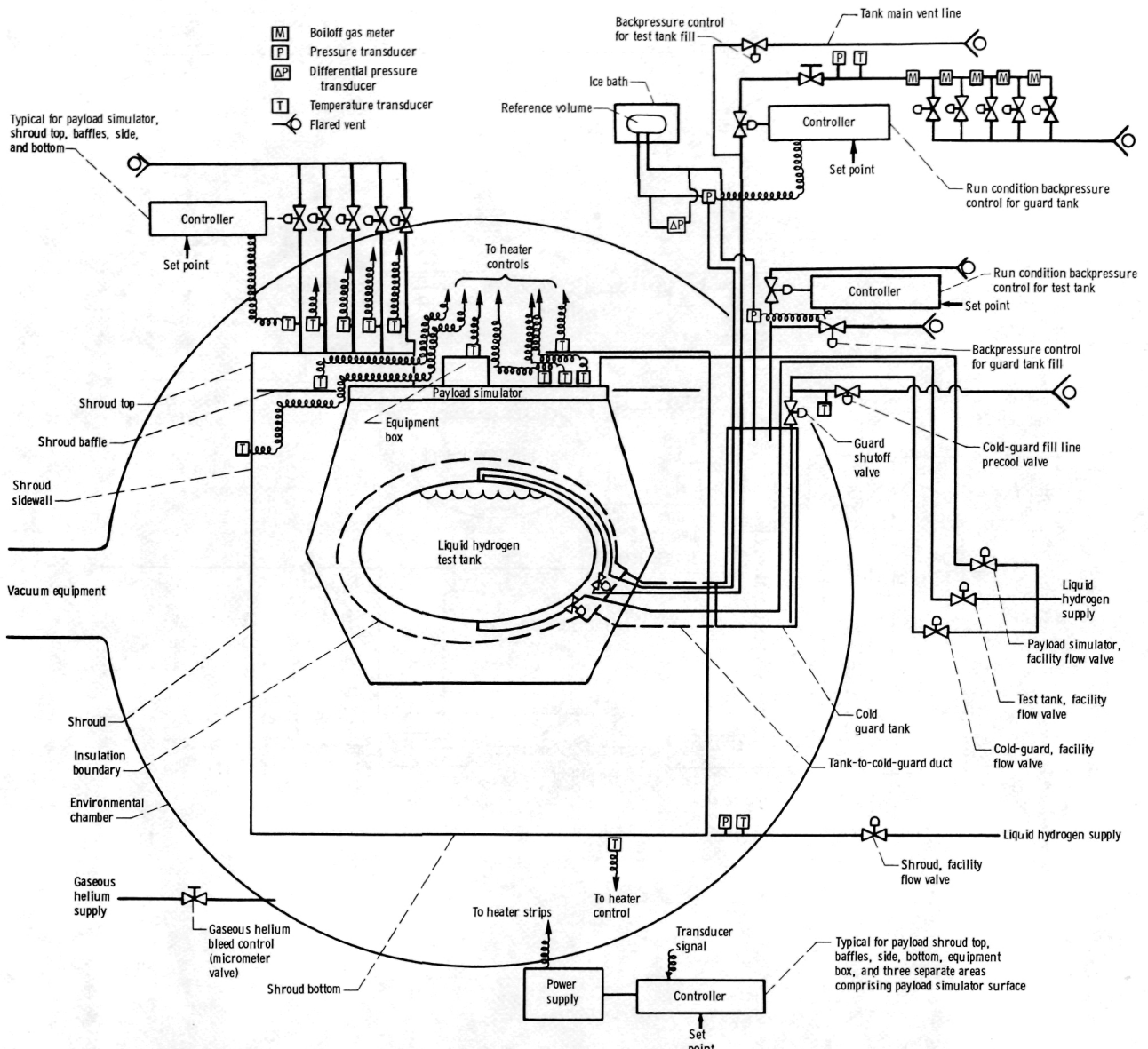


Figure 18. - Schematic of facility plumbing and control circuits.

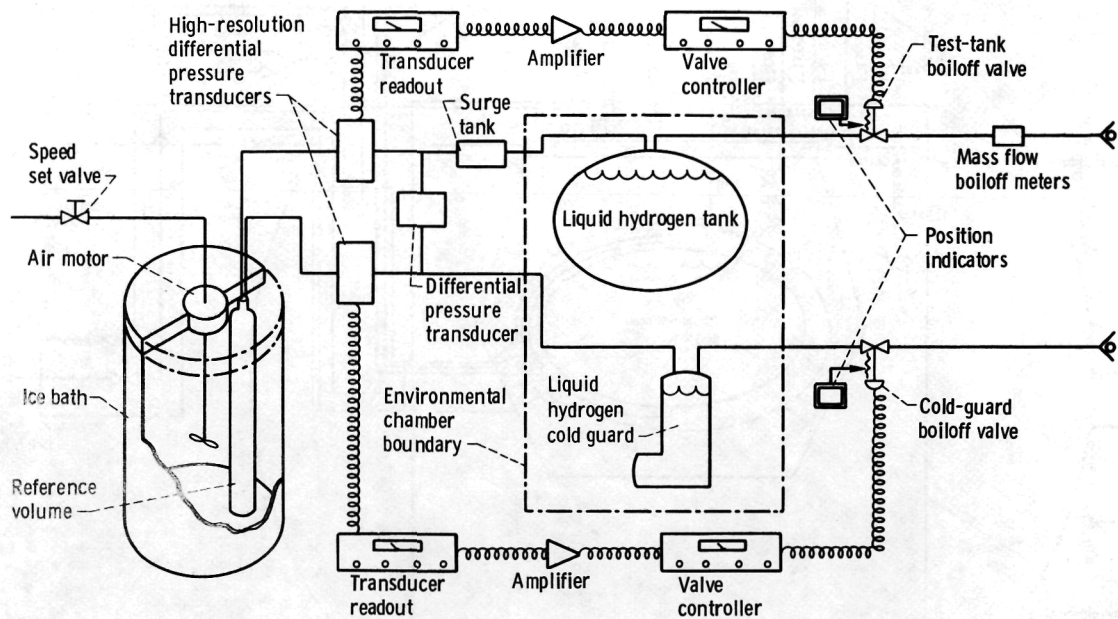
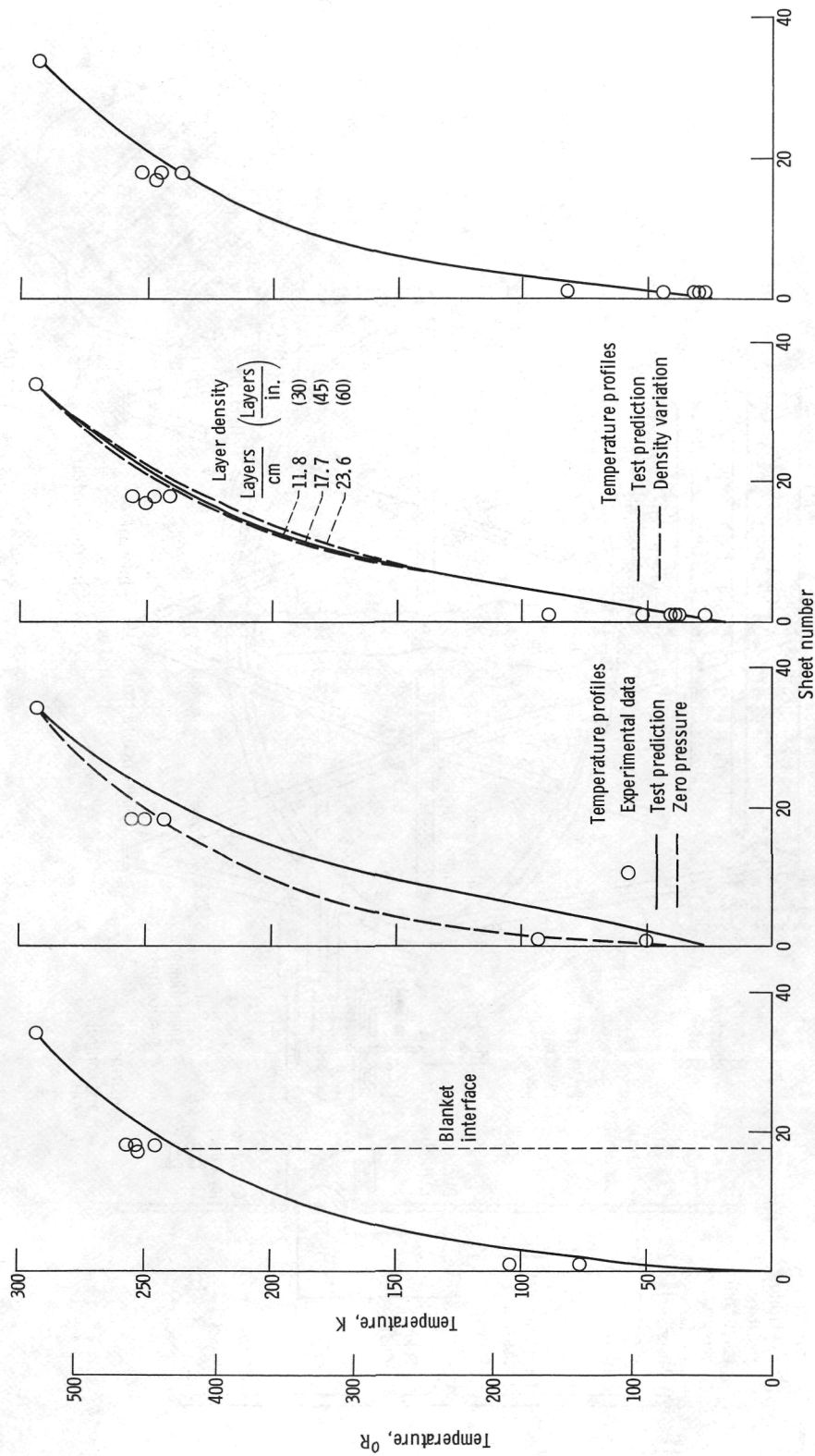


Figure 19. - Block diagram of test tank and cold guard backpressure control system.



(d) Test NE-8.

(c) Test NE-7.

(b) Test NE-5.

(a) Test NE-1.

Figure 21. - Temperature profiles through insulation for Near Earth tests.

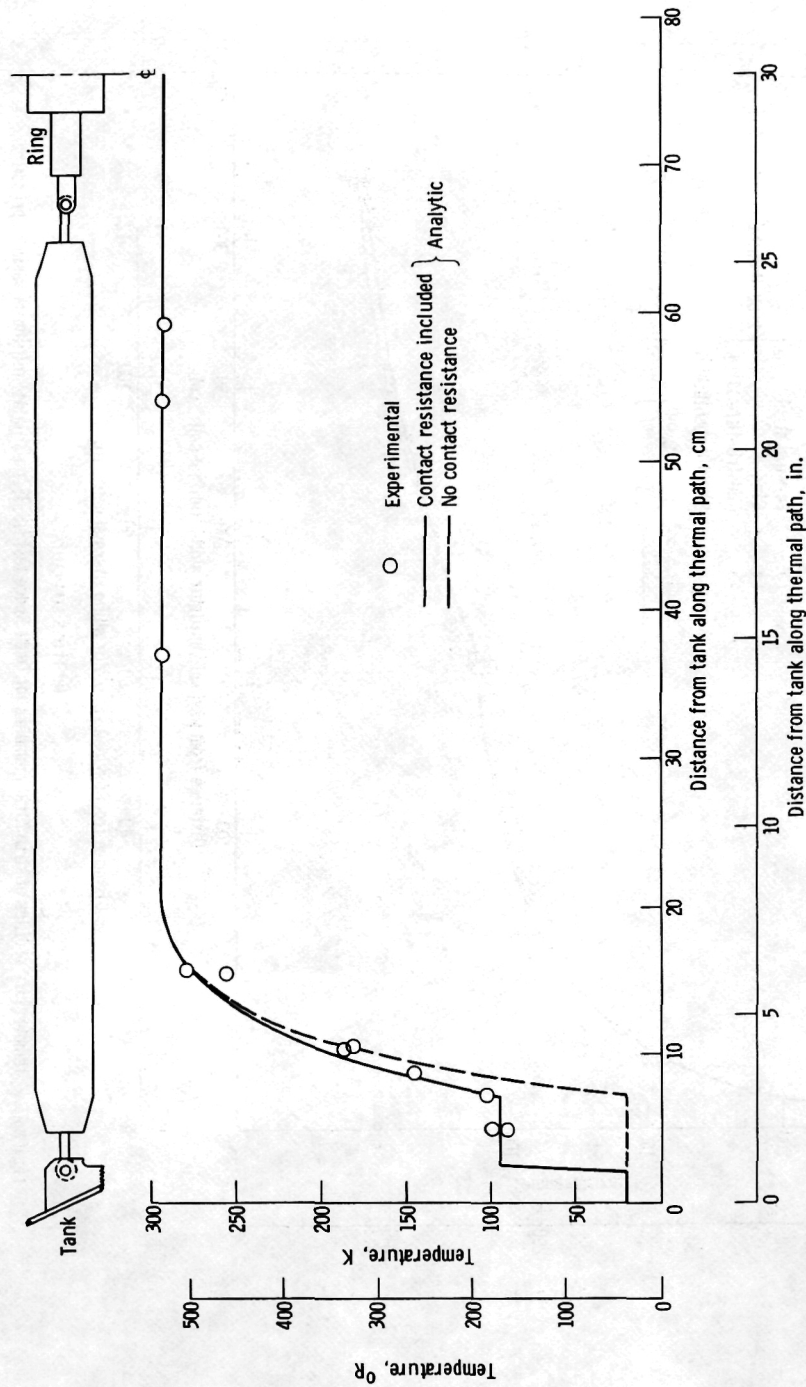
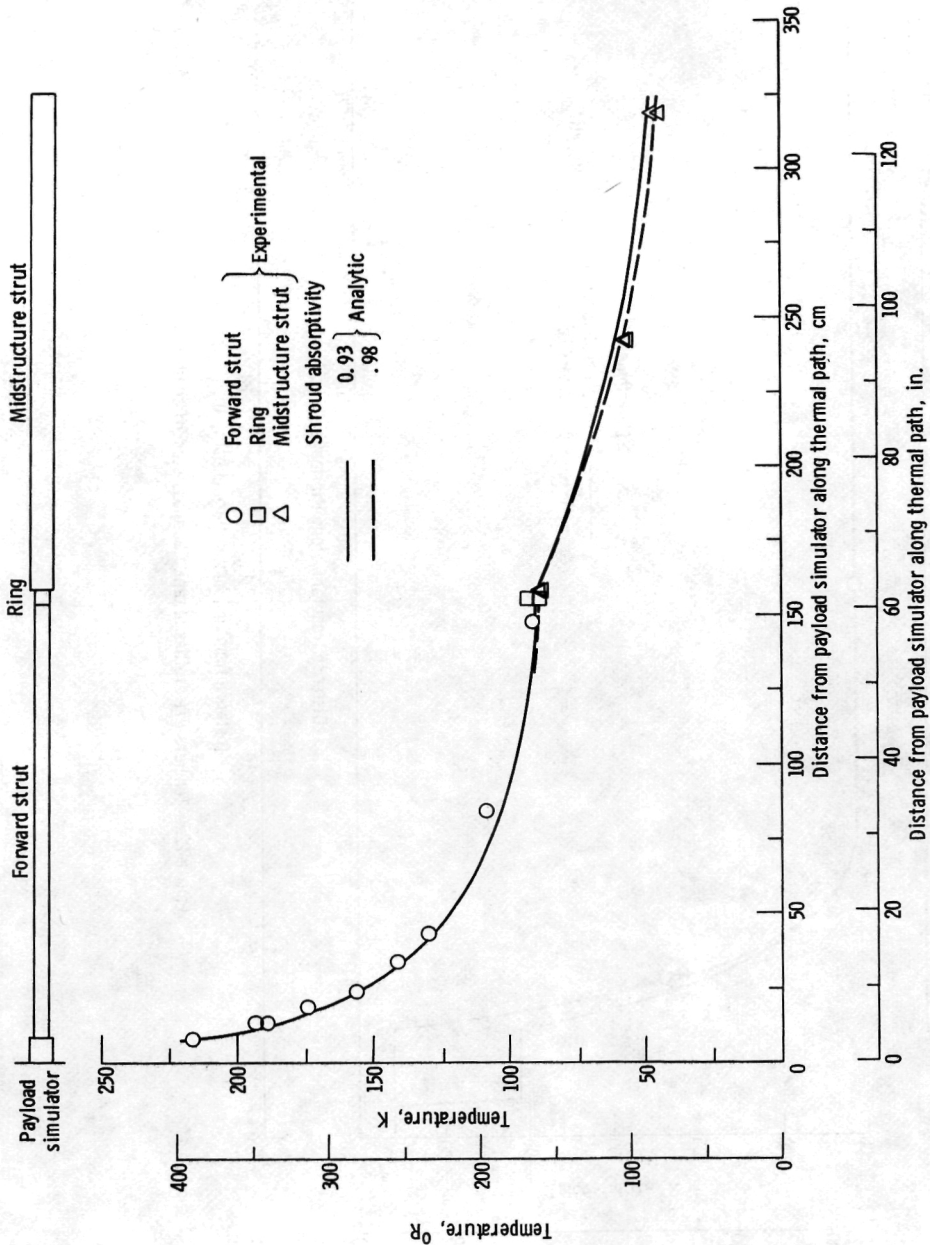
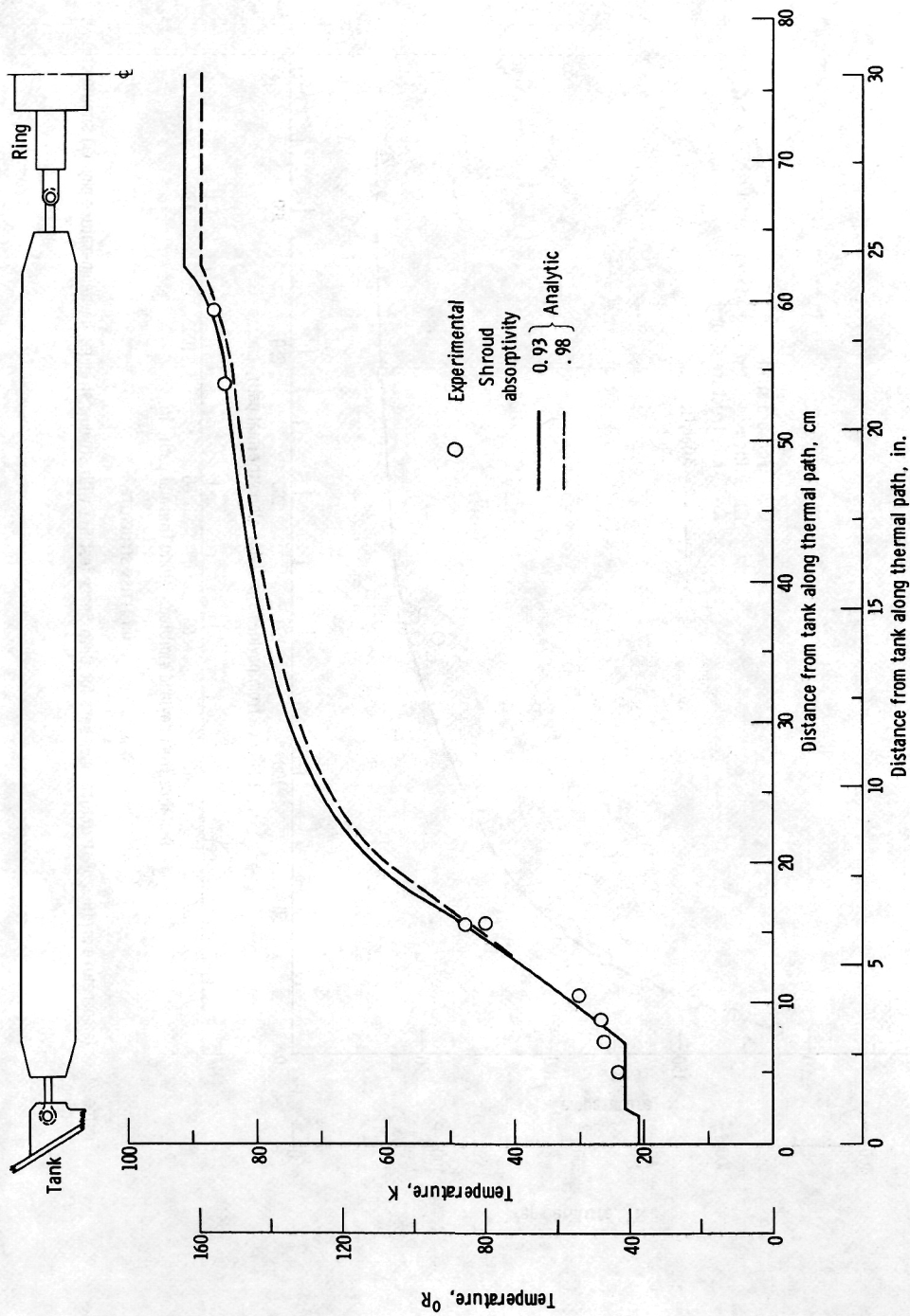


Figure 22. - Temperature profiles of tank fiberglass support strut (test NE-7).



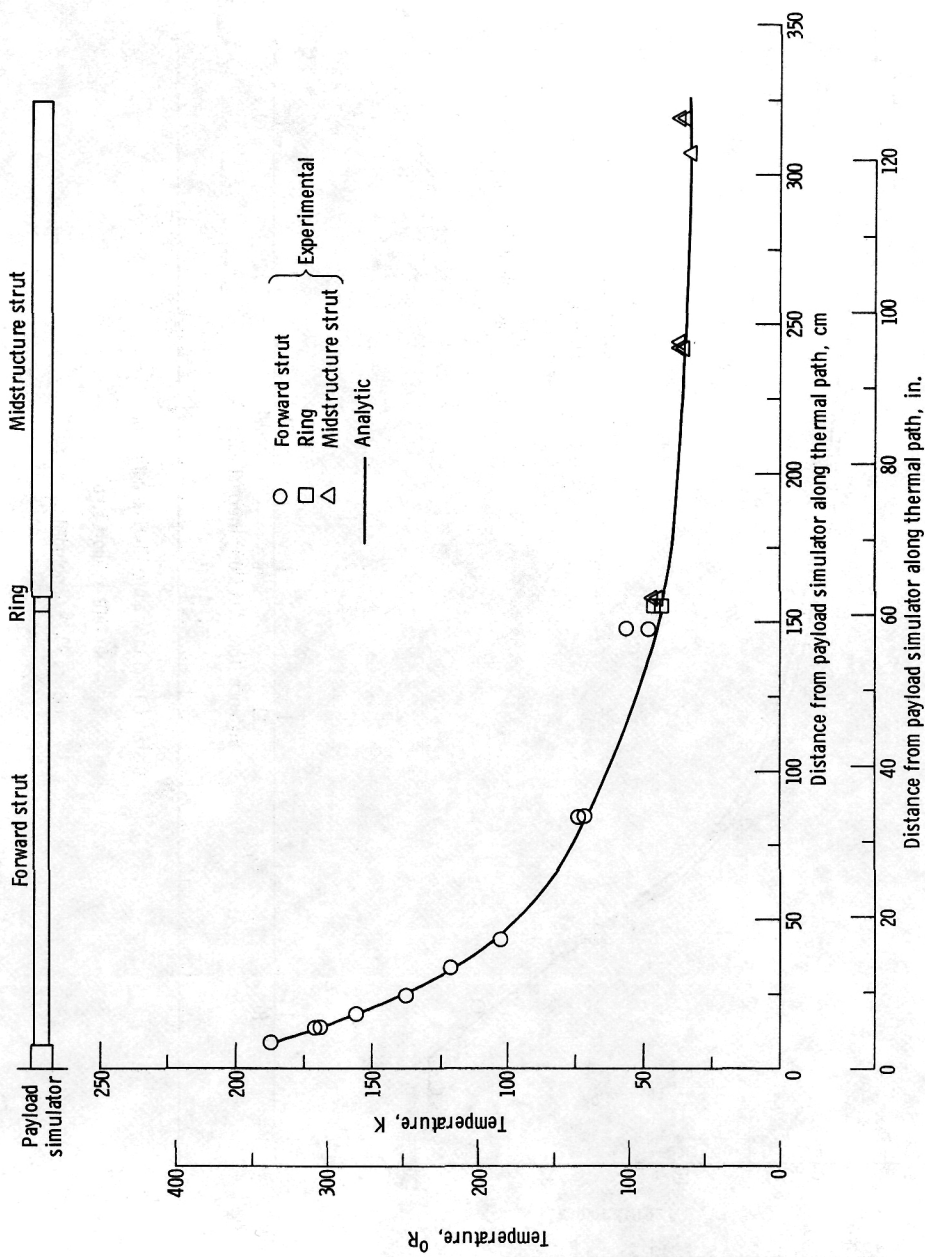
(a) Truss structure.

Figure 23. - Temperature profiles of structural members for Deep Space test NS-1; no shields; minimum vacuum pressure.



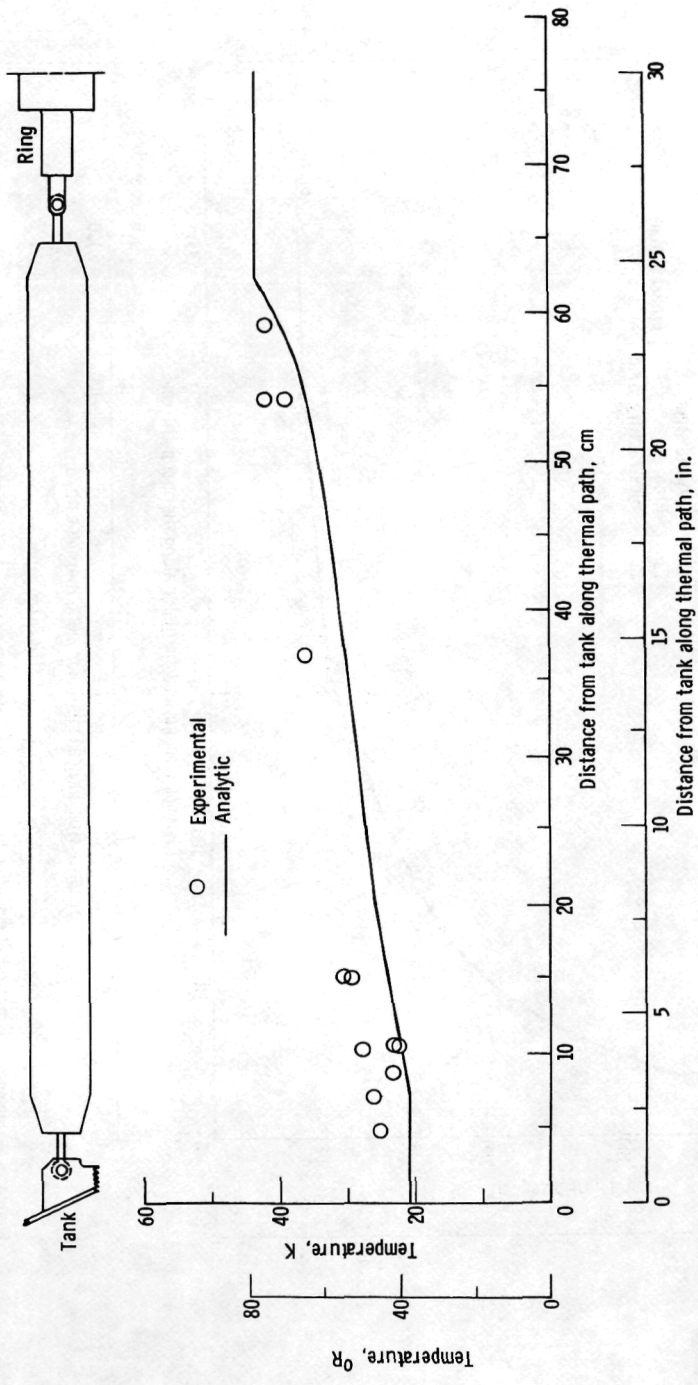
(b) Tank support strut.

Figure 23. - Concluded.



(a) Truss structure.

Figure 24. - Temperature profiles of structural members for Deep Space test S-1 with shadow shields; low temperature payload simulator setting.



(b) Tank support strut.

Figure 24. - Concluded.

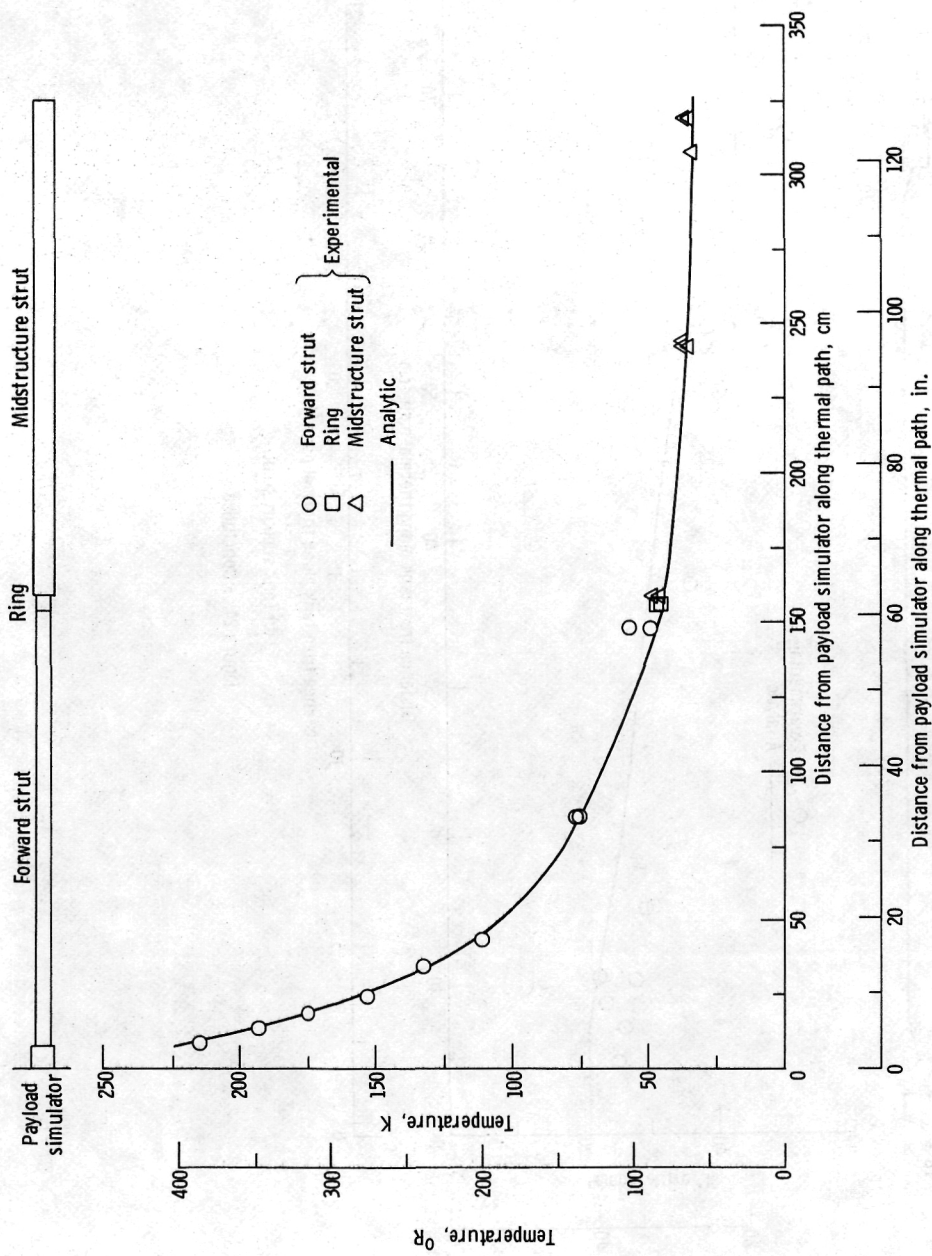
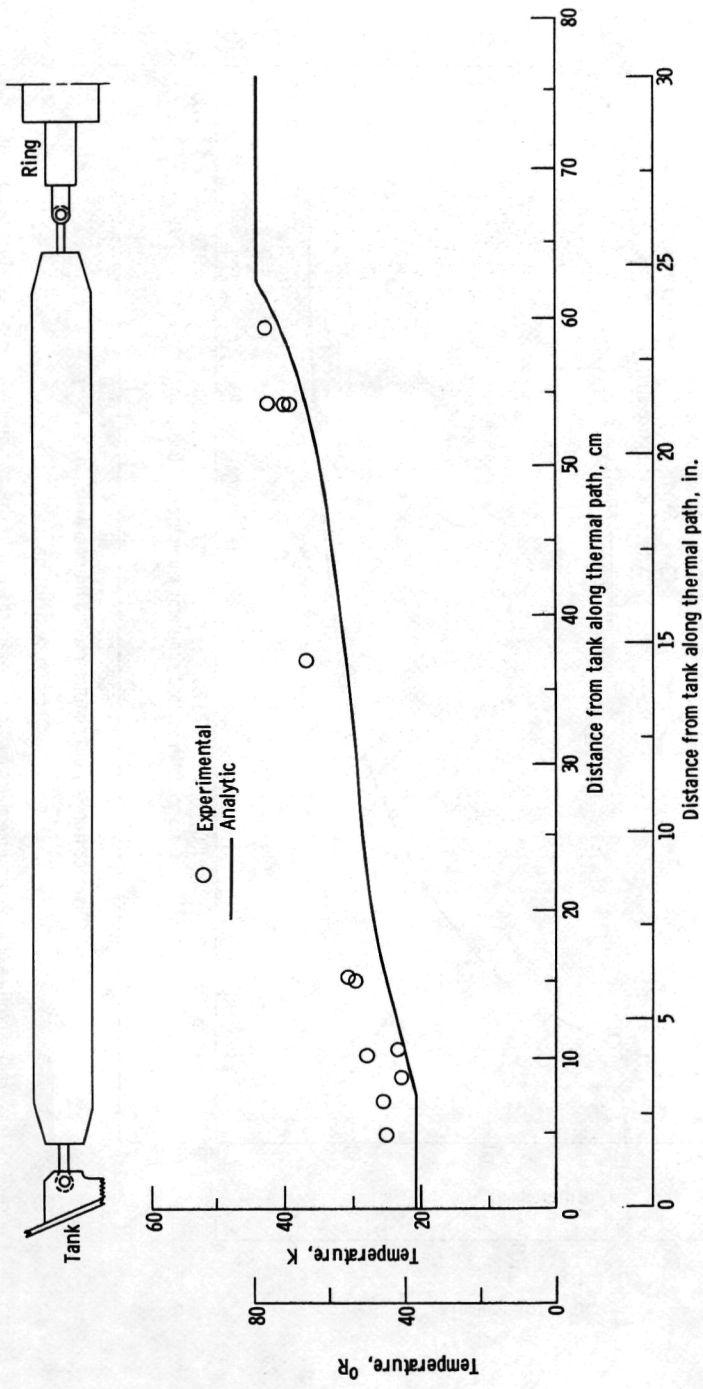
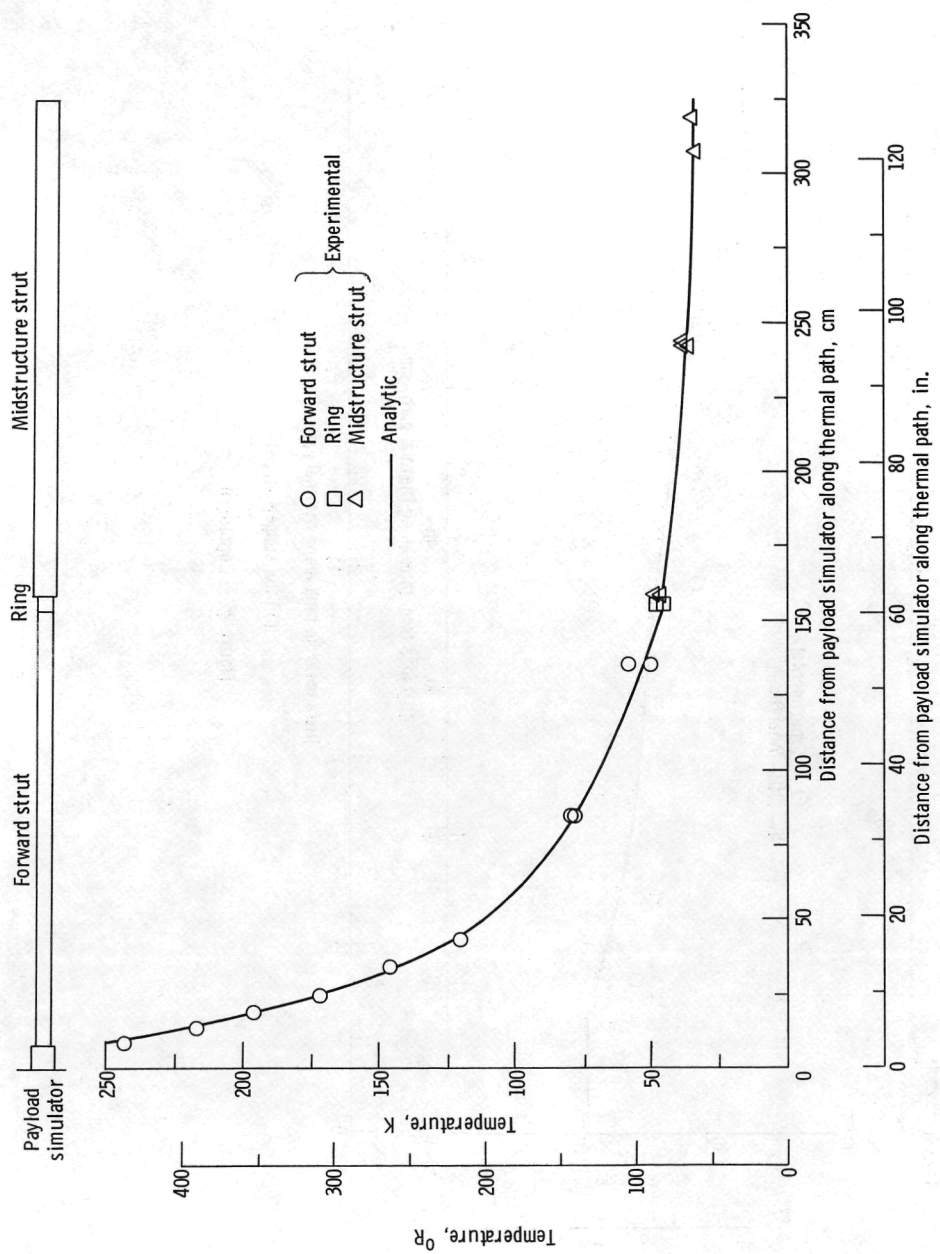


Figure 25. - Temperature profiles of structural members for Deep Space test S-2 with shadow shields; intermediate temperature payload simulator setting.
 (a) Truss structure.



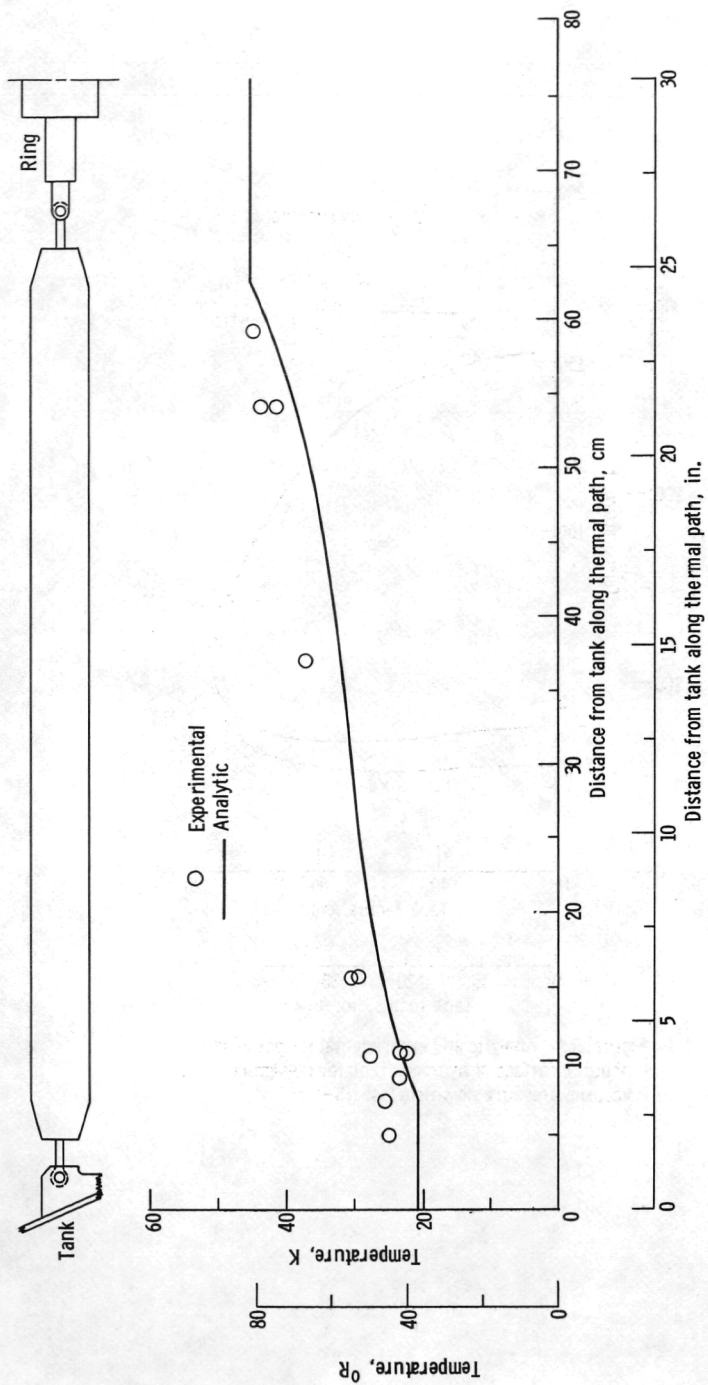
(b) Tank support strut.

Figure 25. - Concluded.



(a) Truss structure.

Figure 26. - Temperature profiles of structural members for Deep Space test S-3 with shadow shields; room temperature payload simulator and minimum vacuum pressure.



(b) Tank support strut.

Figure 26. - Concluded.

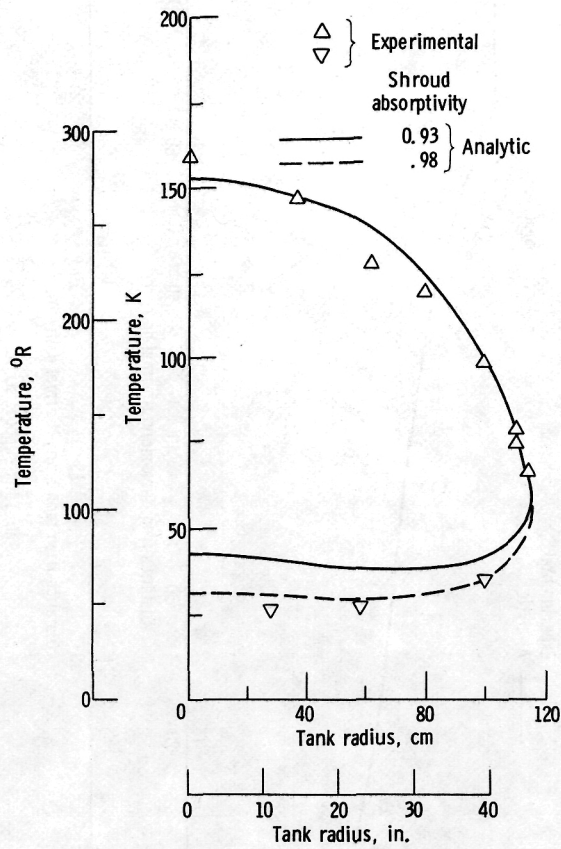
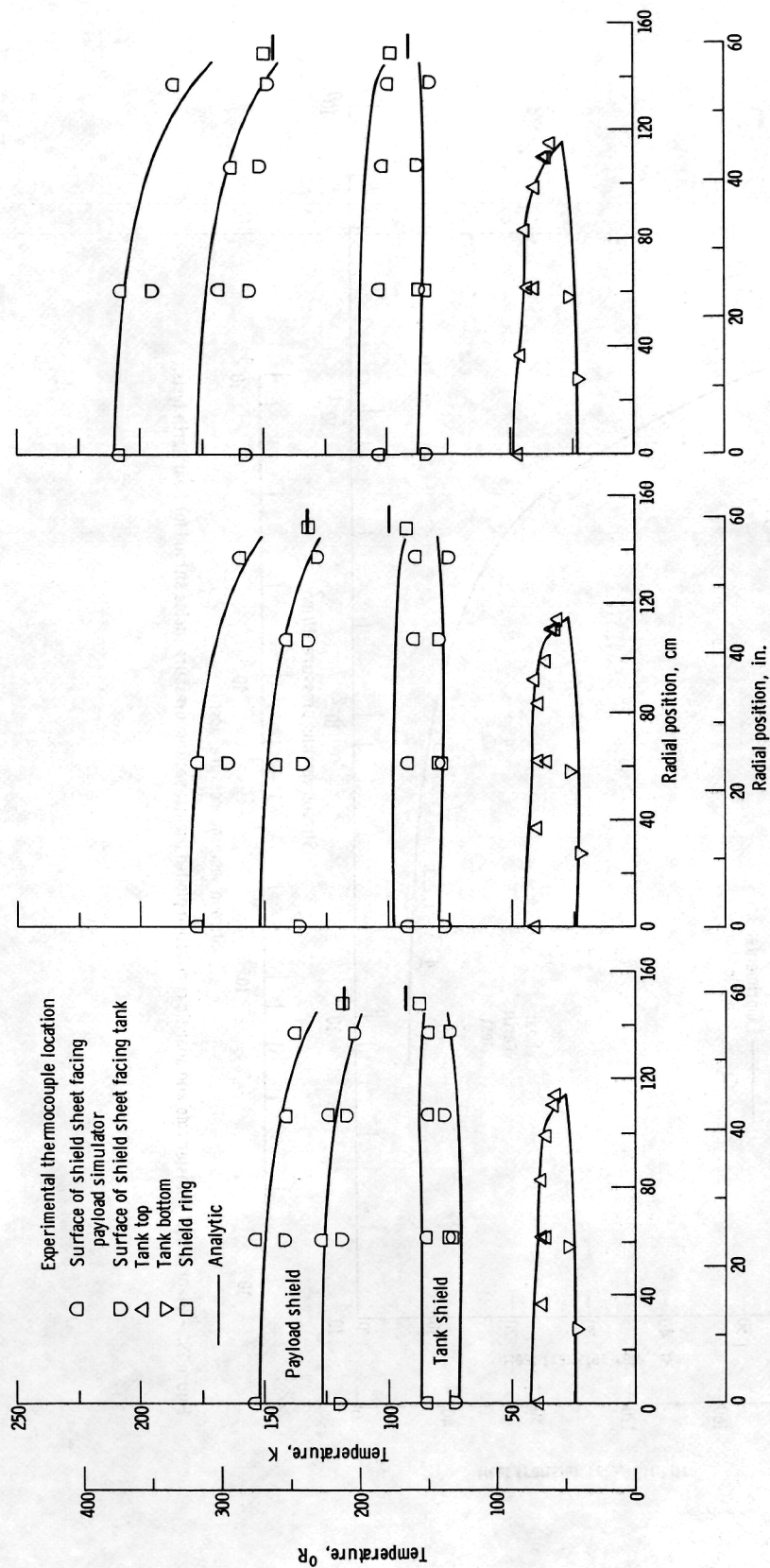


Figure 27. - Analytic and experimental temperatures of outer surface of hydrogen tank for minimum vacuum pressure no shield test NS-1.



(a) Low temperature payload simulator.

(b) Intermediate temperature payload simulator.

(c) Room temperature payload simulator.

Figure 28. - Temperatures of shadow shields and outer surface of hydrogen tank insulation for minimum vacuum pressure tests S-1, S-2, and S-3.

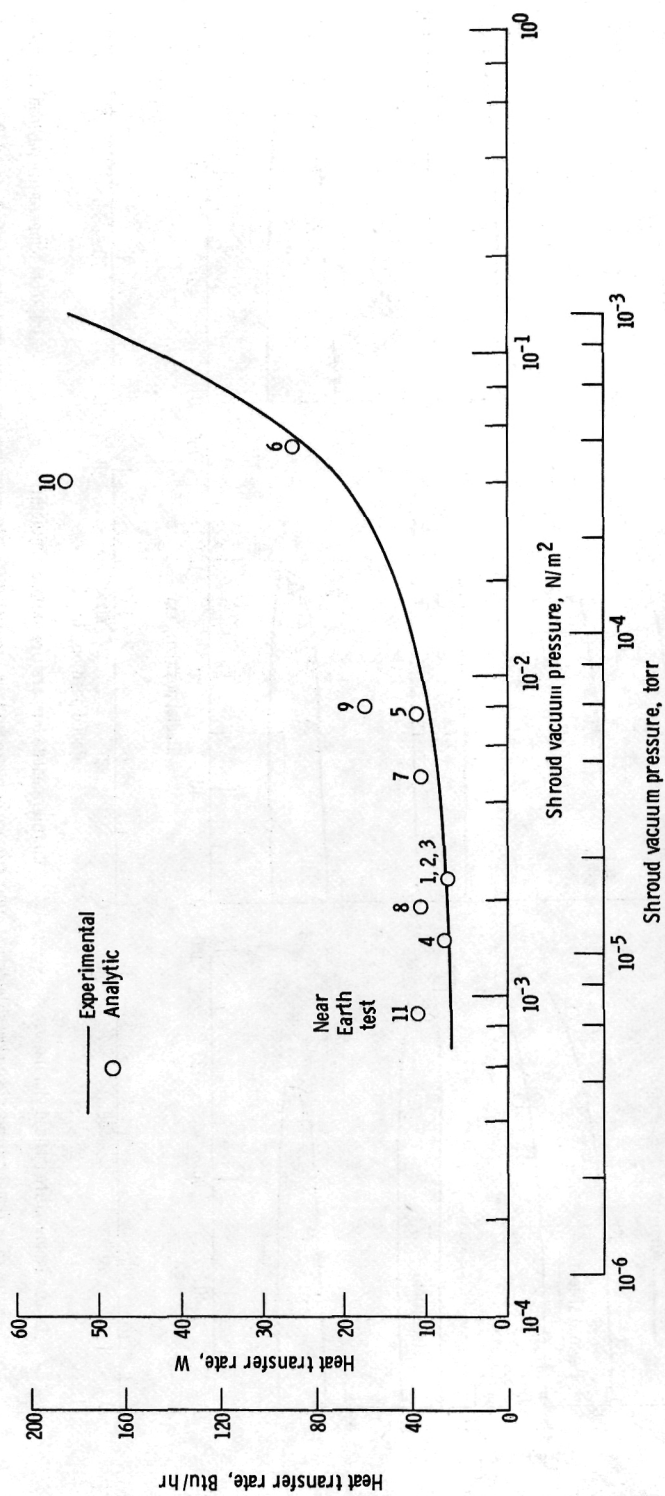


Figure 29. - Blanket heat transfer rate and analytic correlation plotted against vacuum pressure inside shroud for Near Earth tests.

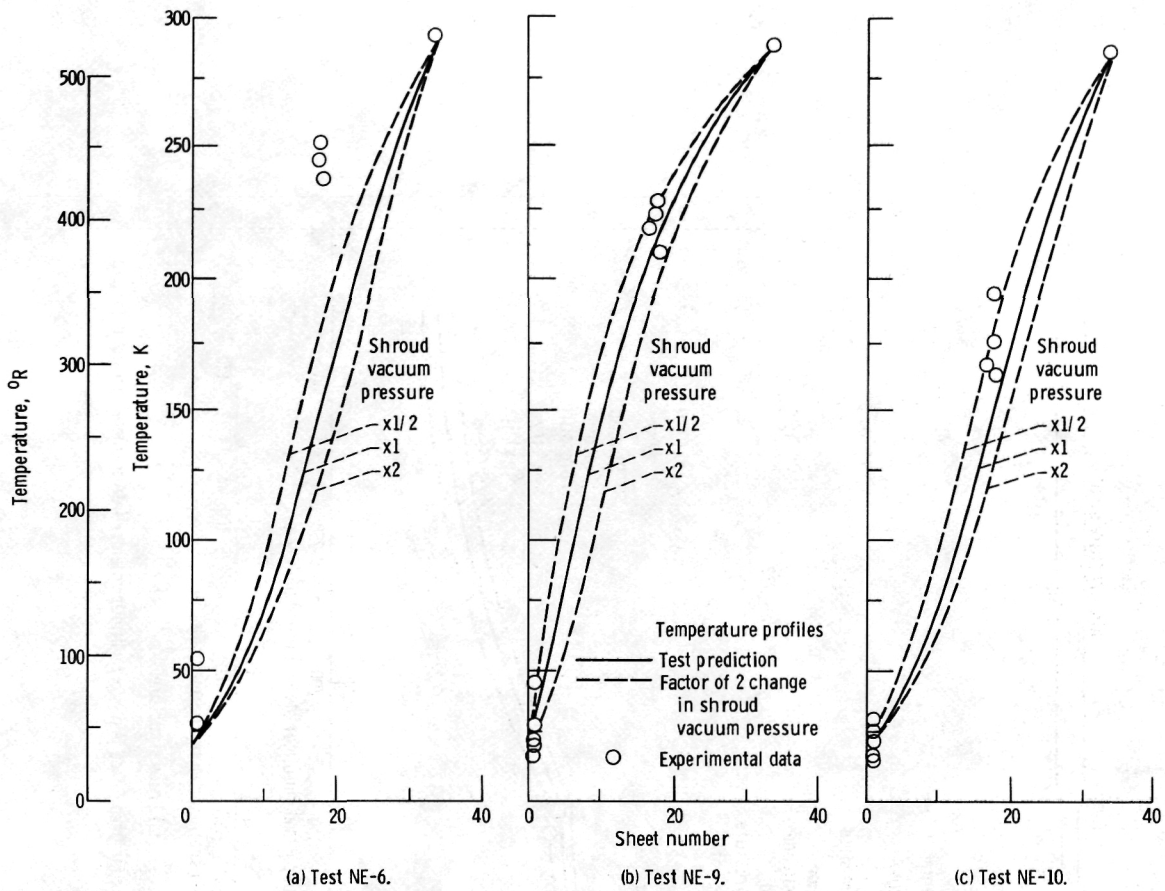


Figure 30. - Effect of vacuum pressure on Near Earth insulation temperatures.

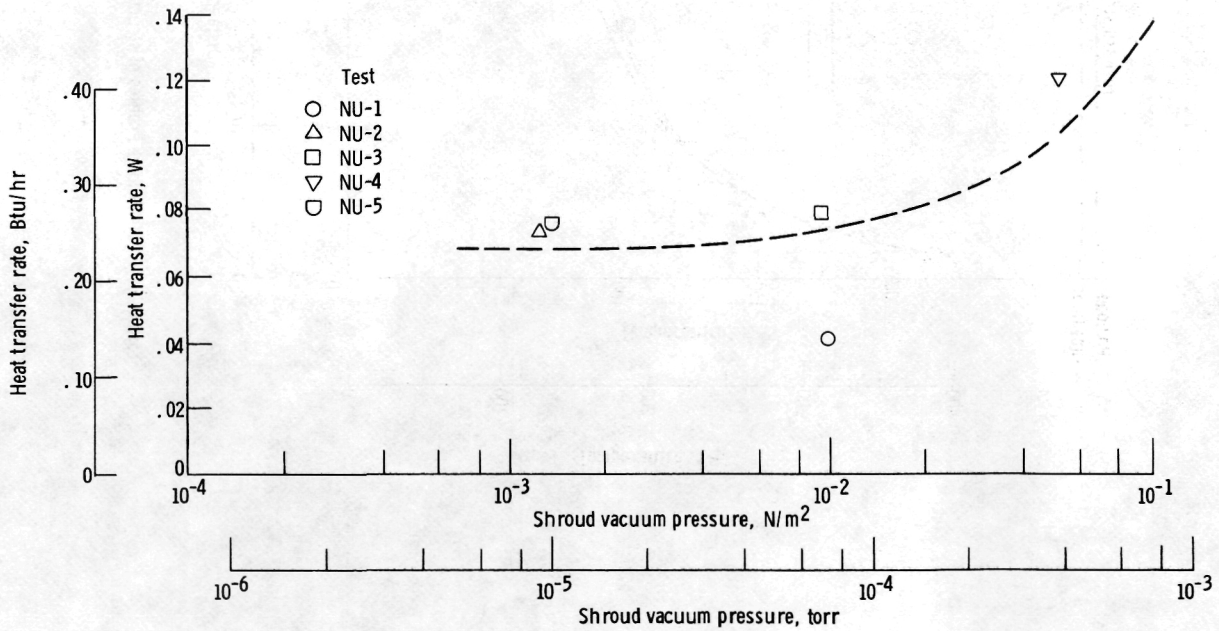
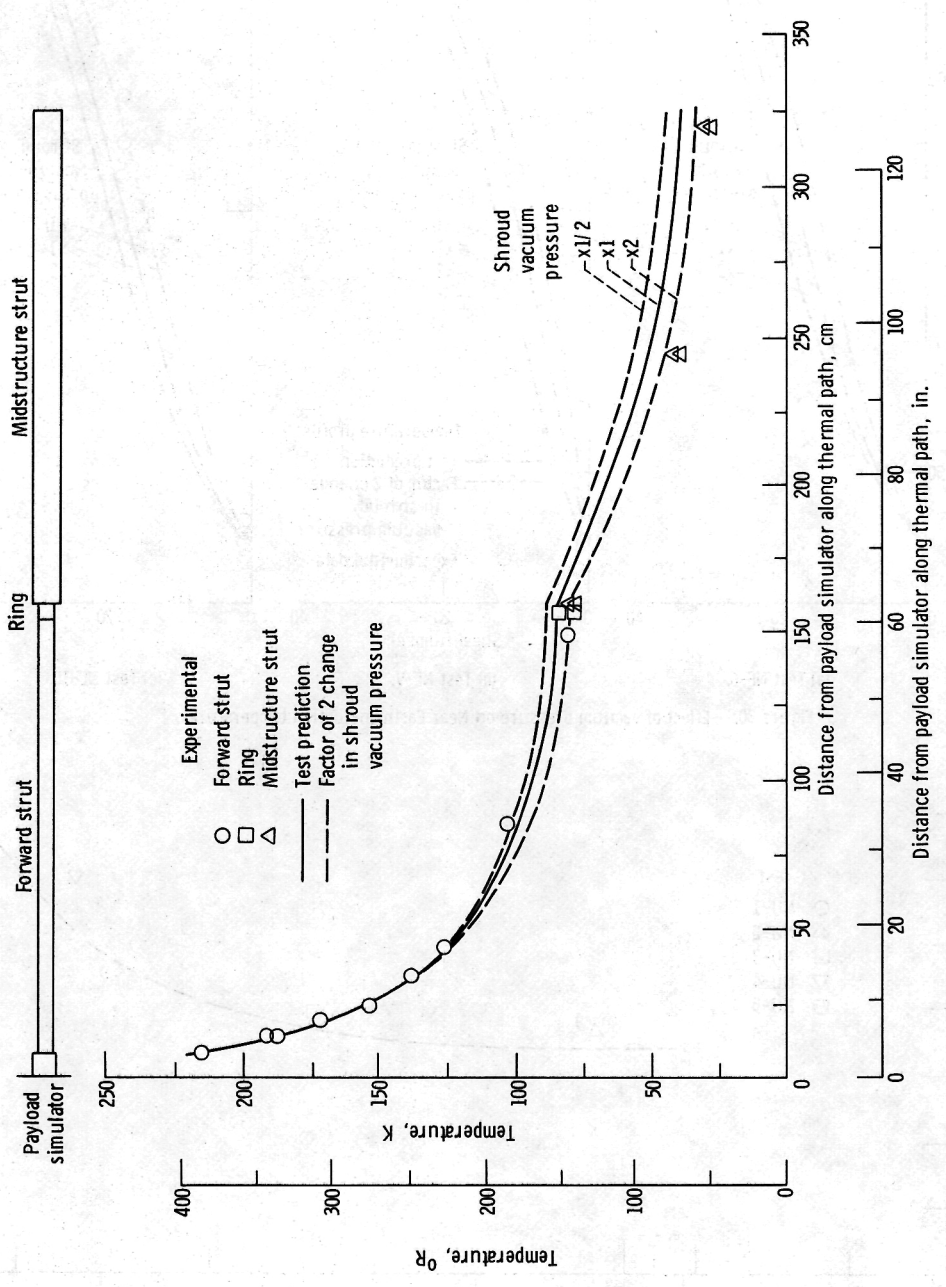
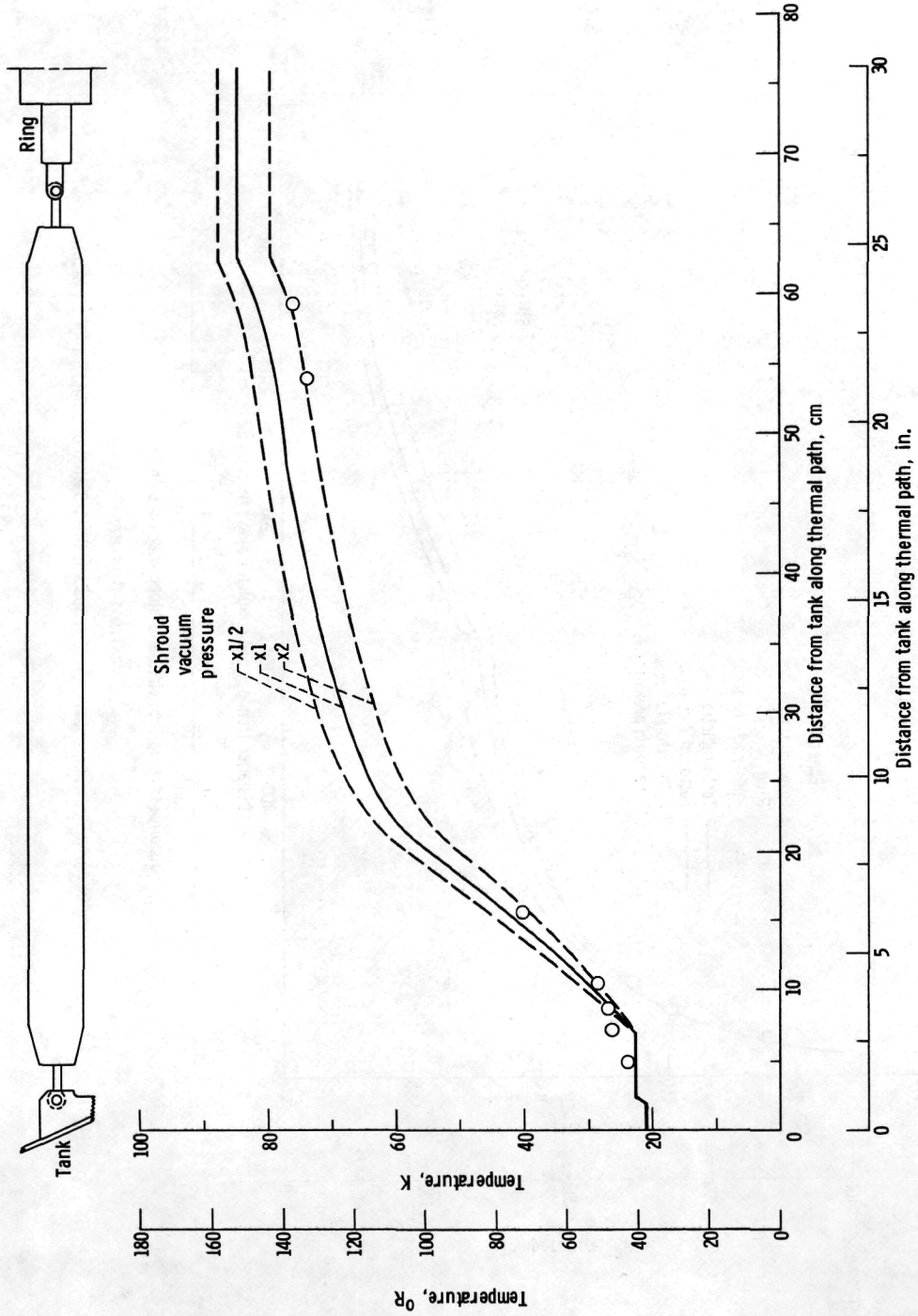


Figure 31. - Measured heat transfer for Null tests as function of vacuum pressure inside shroud.



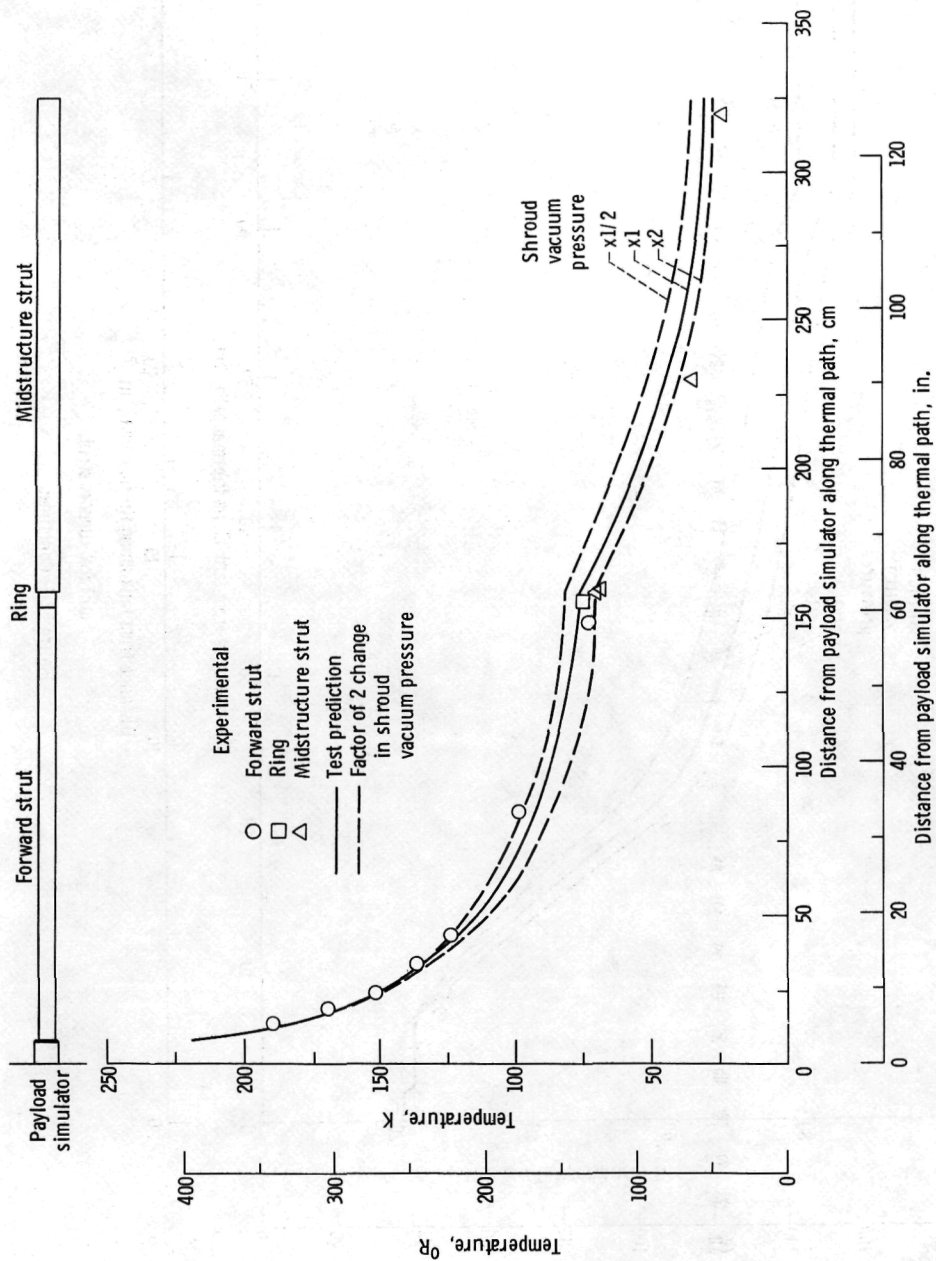
(a) Truss structure.

Figure 32. - Temperature profiles of structural members for Deep Space test NS-2 without shields; intermediate vacuum pressure.



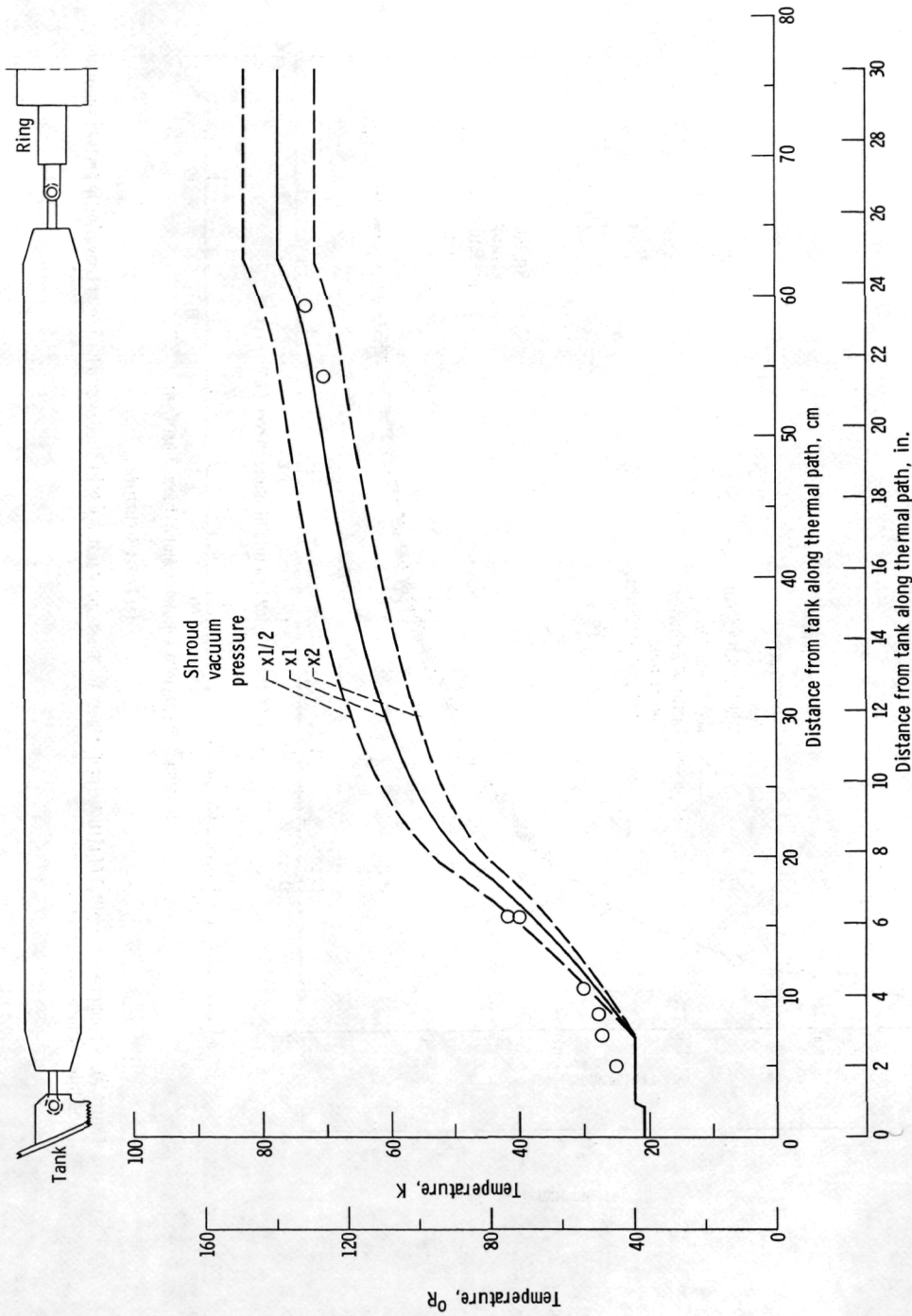
(b) Tank support strut.

Figure 32 - Concluded.



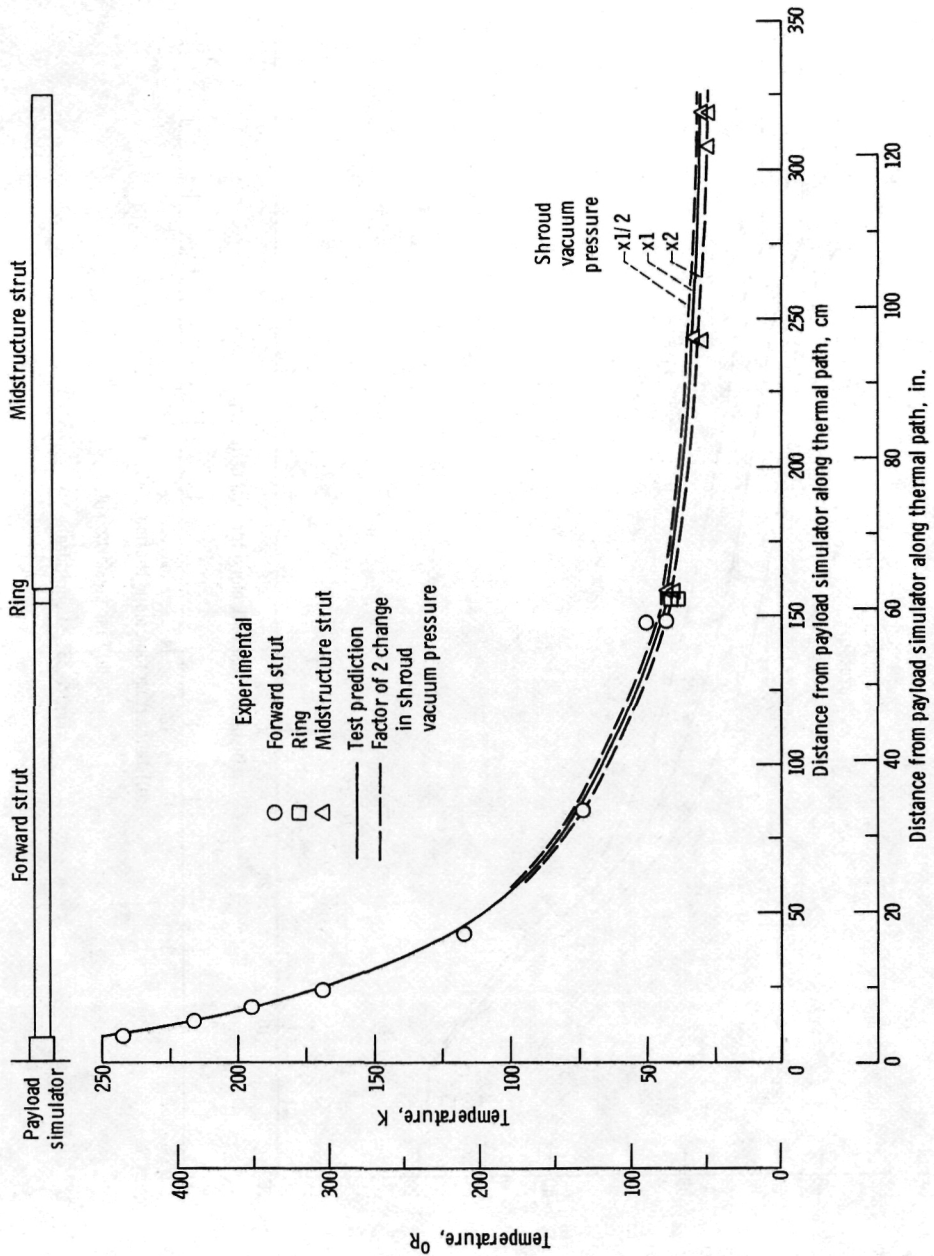
(a) Truss structure.

Figure 33. - Temperature profiles of structural members for Deep Space test NS-3 without shields; highest vacuum pressure.



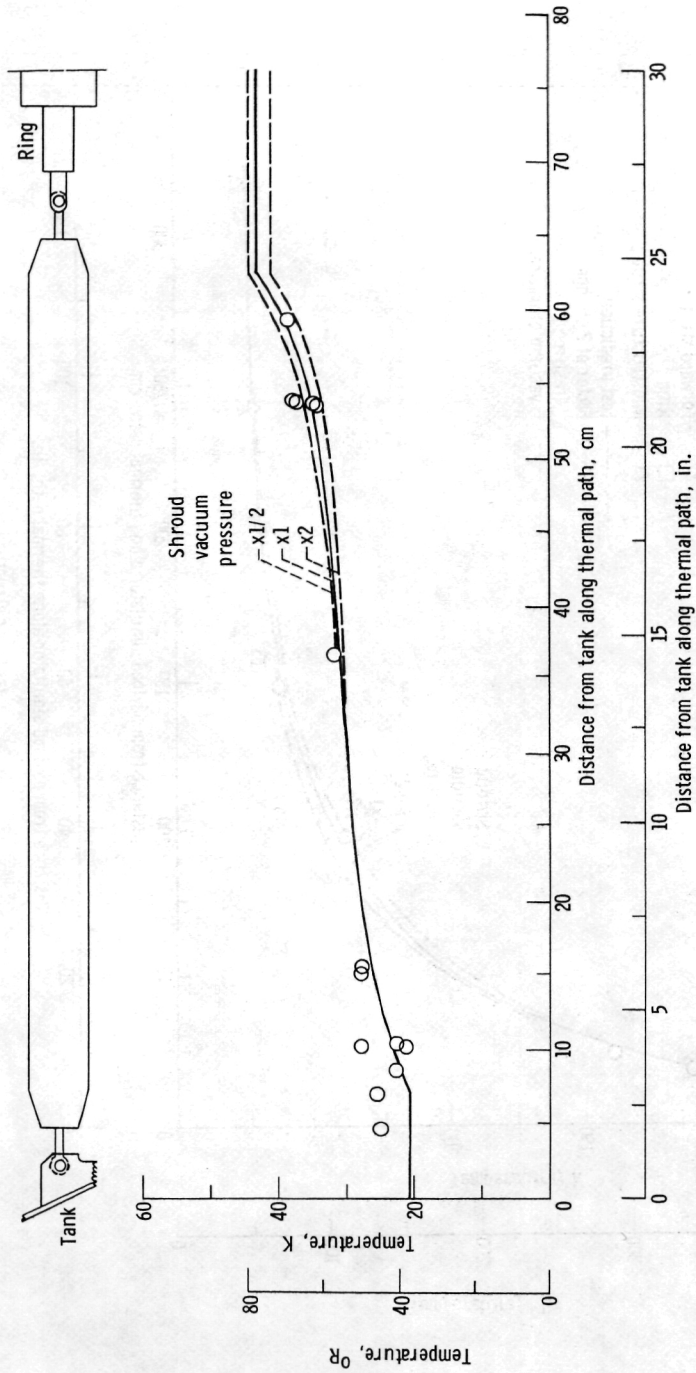
(b) Tank support strut.

Figure 33. - Concluded.



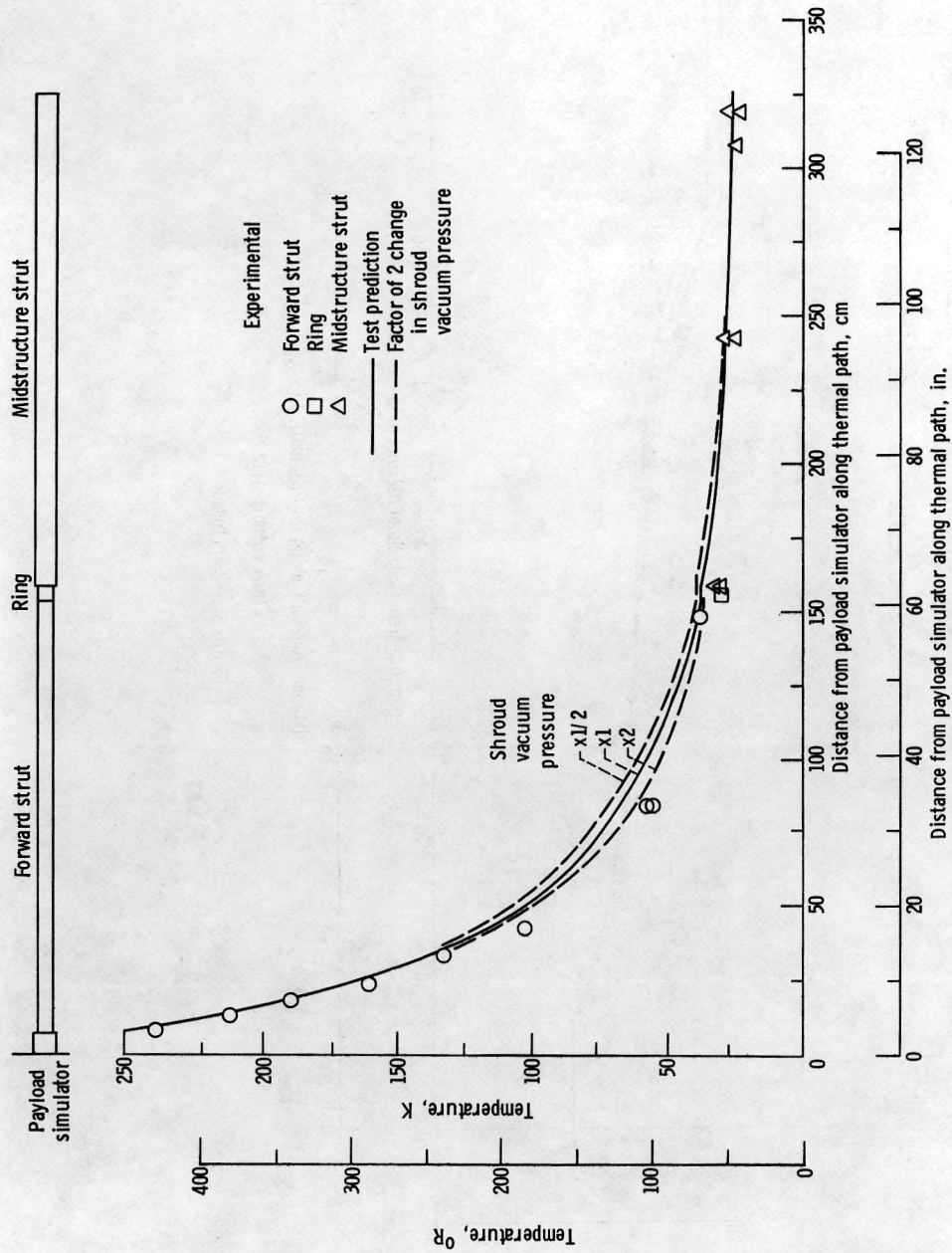
(a) Truss structure.

Figure 34. - Temperature profiles of structural members for Deep Space test S-4 with shadow shields; room temperature payload simulator and intermediate vacuum pressure.



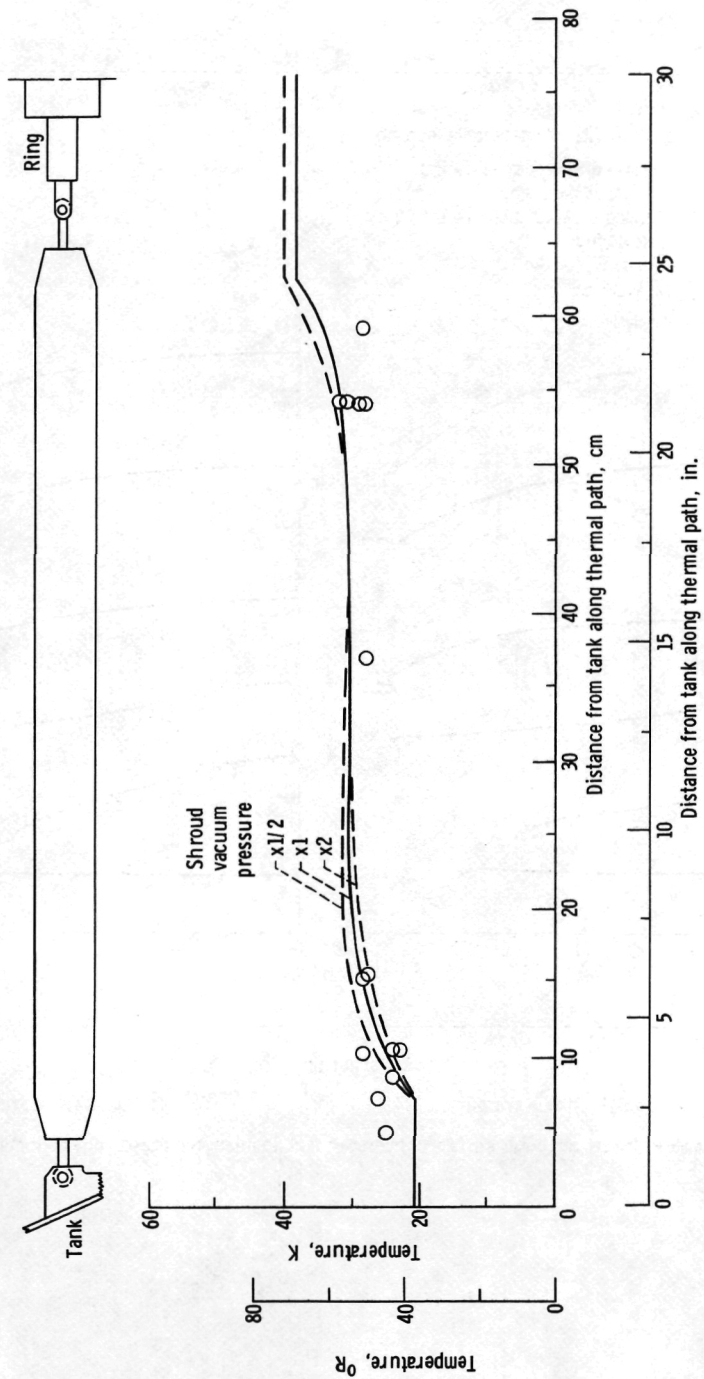
(b) Tank support strut.

Figure 34. - Concluded.



(a) Truss structure.

Figure 35. - Temperature profiles of structural members for Deep Space test S-5 with shadow shields; room temperature payload simulator and highest vacuum pressure.



(b) Tank support strut.

Figure 35. - Concluded.

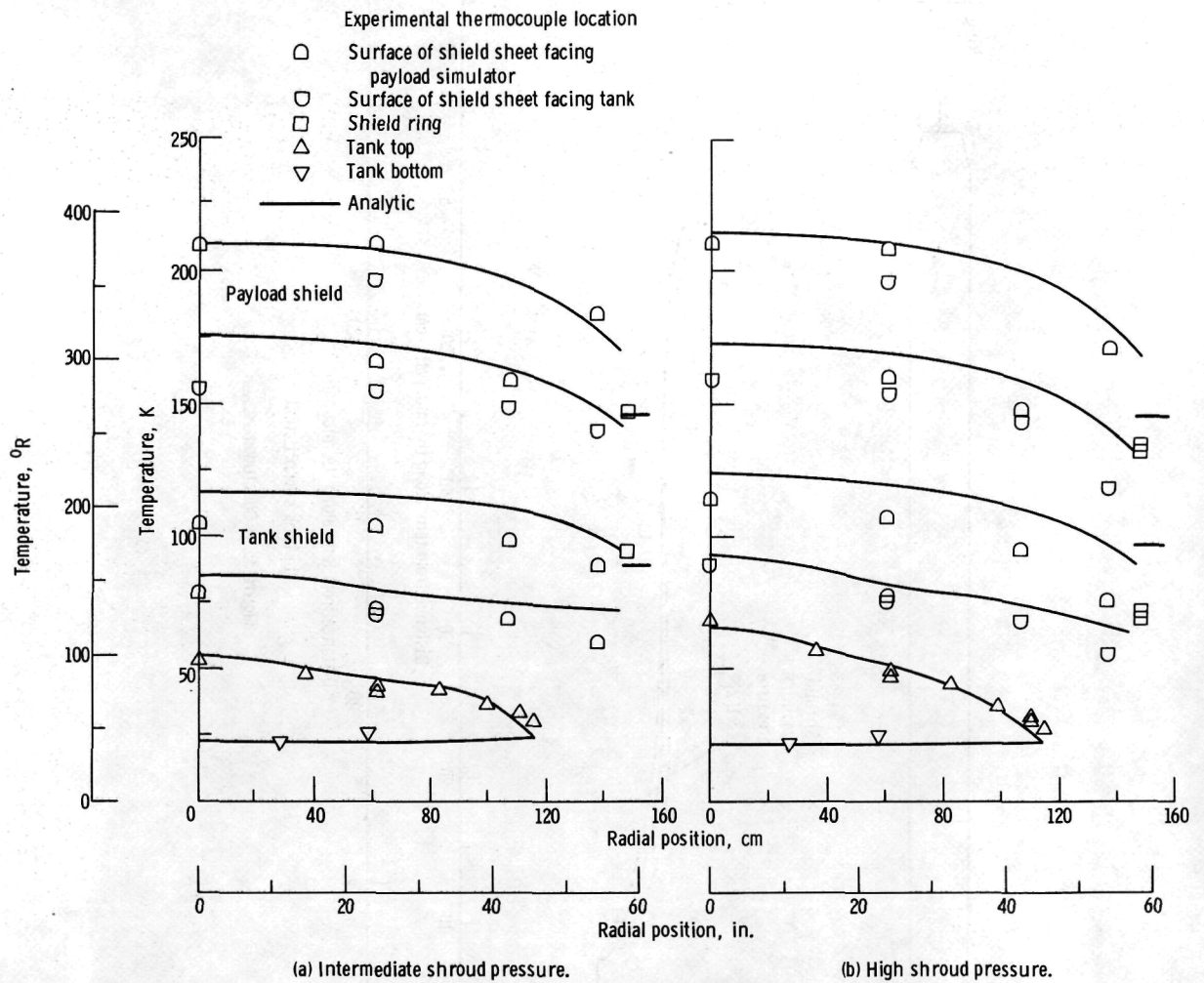


Figure 36. - Temperatures of shadow shields and outer surface of hydrogen tank insulation for tests with helium bleed (tests S-4 and S-5).

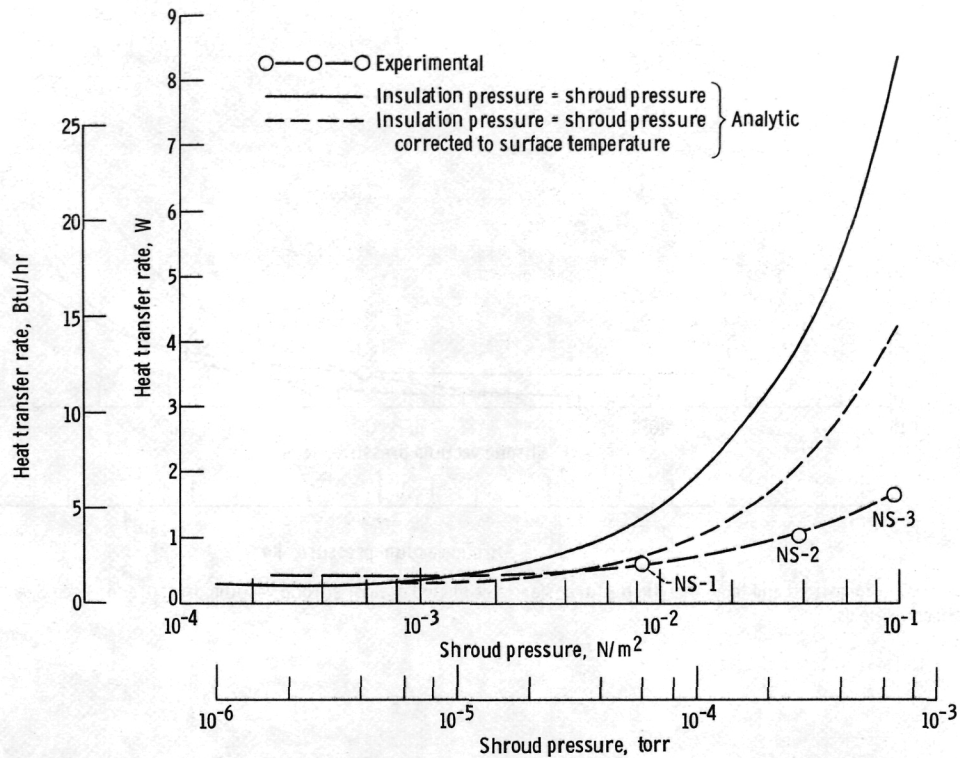


Figure 37. - Experimental and analytic blanket heat transfer rate as function of shroud vacuum pressure for Deep Space tests without shields.

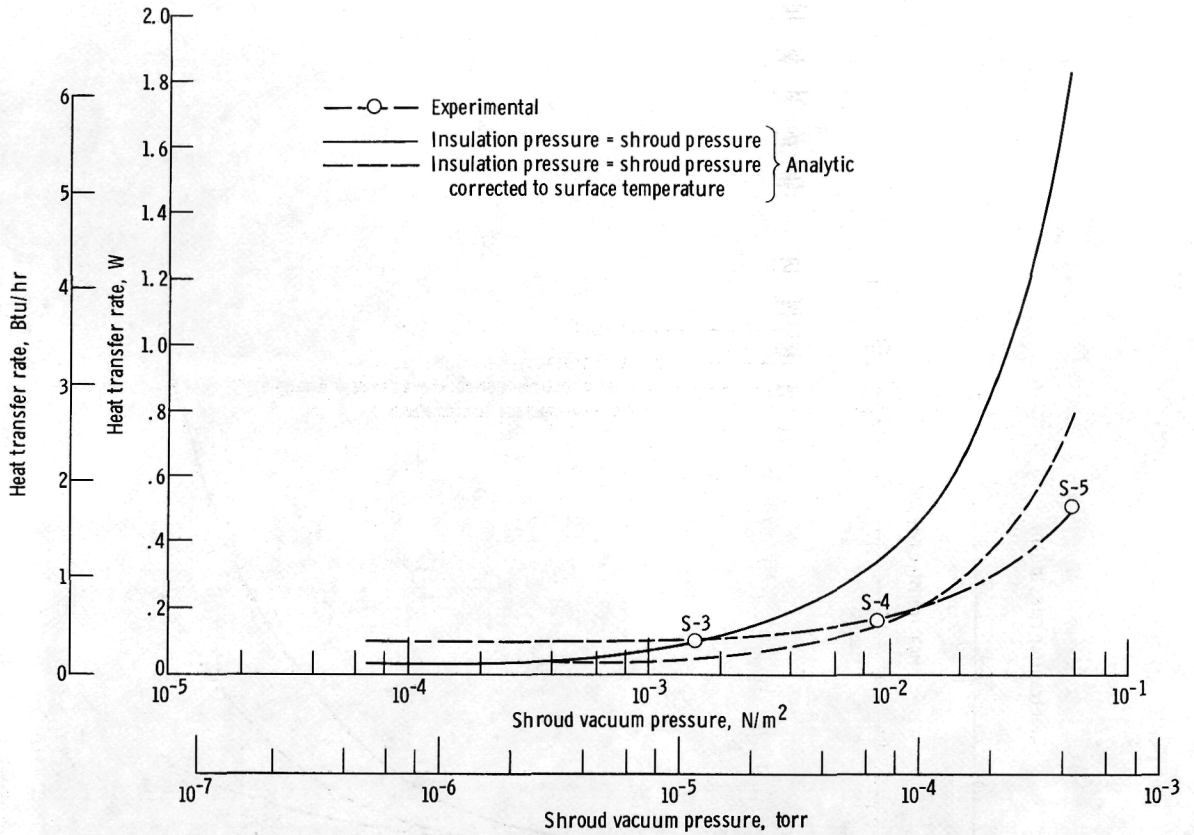


Figure 38. - Measured and total analytic heat transfer rates plotted against shroud vacuum pressure for Deep Space tests with shadow shields.

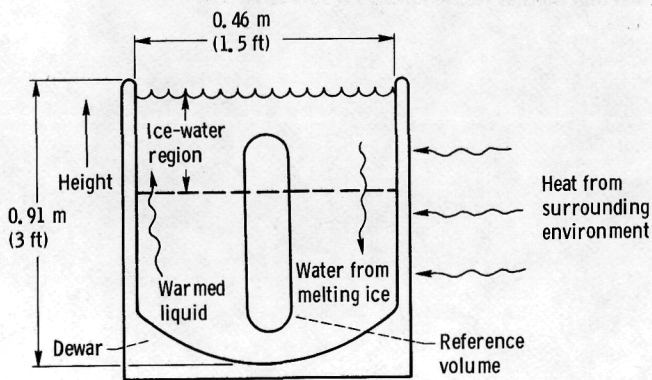


Figure 39. - Expected pattern of convection in ice-water bath.

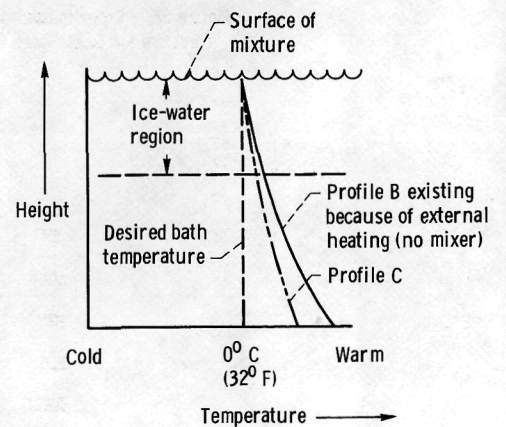


Figure 40. - Possible temperature profiles in ice-water bath.

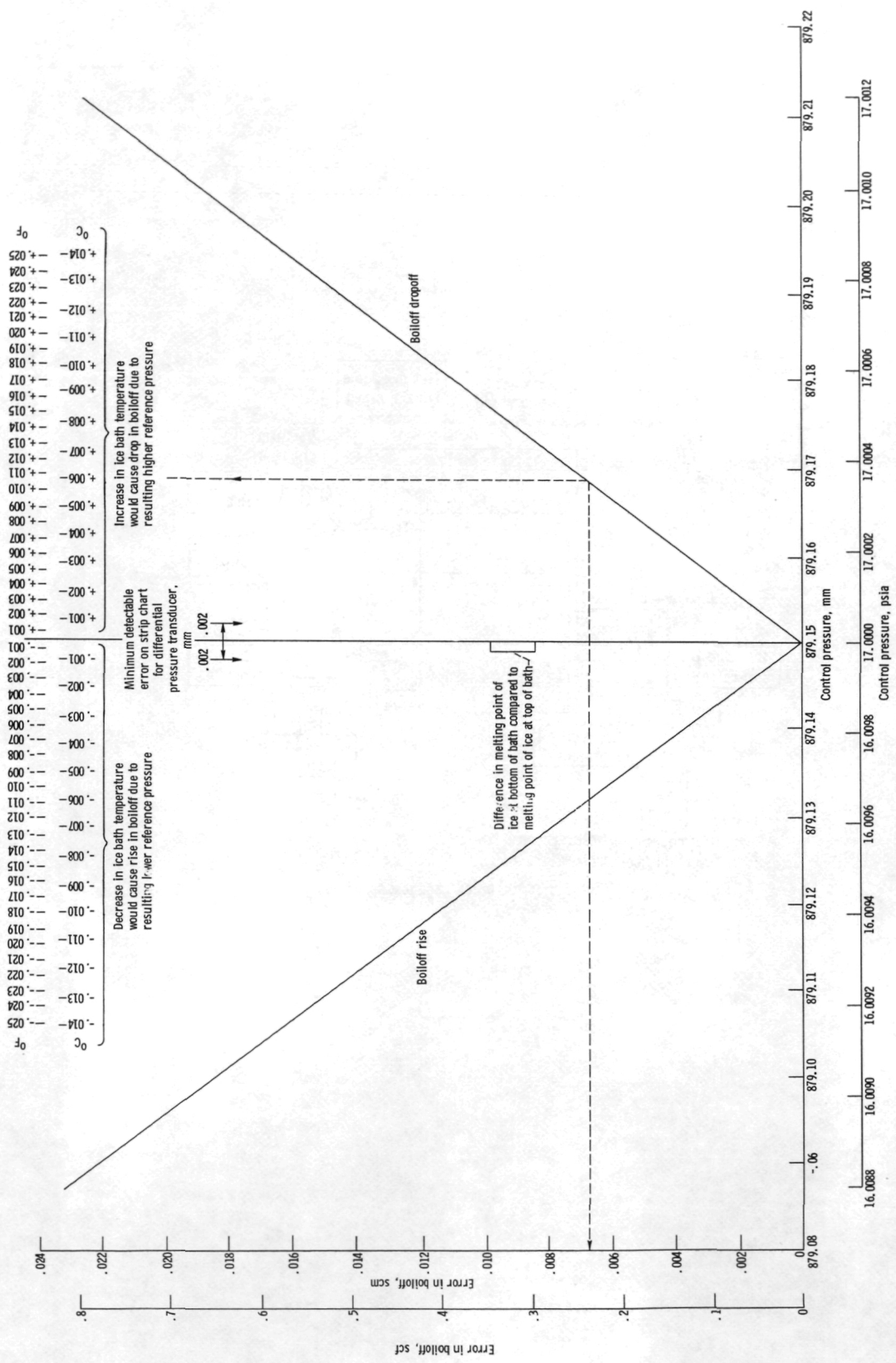


Figure 41. - Volumetric error in quantity of H₂ vent gas as function of control pressure where parameter is ice bath reference temperature. Tank conditions: 5 percent ullage; tank pressure, 11.7 N/cm² abs (17 psia); 325.8 kg (718.2 lb) LH₂. (Possible error in ice bath temperature due to range of barometric pressures encountered during tests with shadow shields was ±0.00010° C (±0.00018° F); this effect cannot be seen on this plot.)

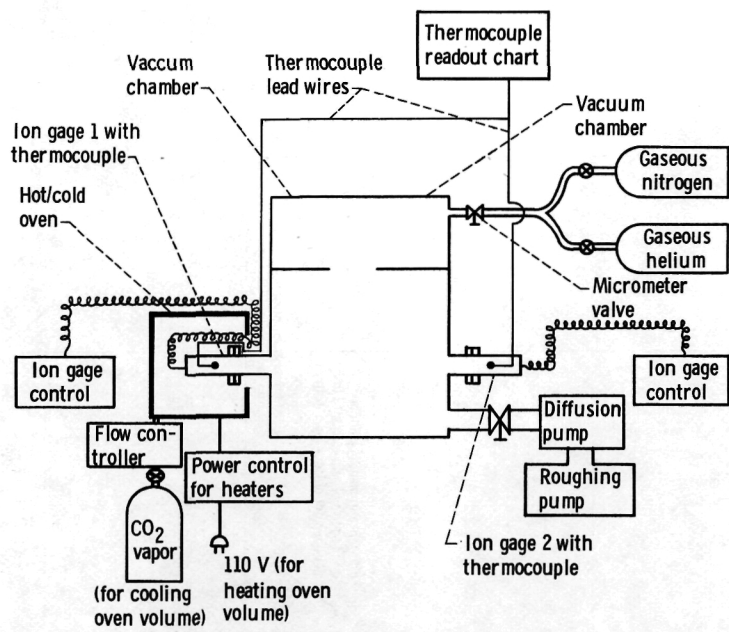


Figure 42. - Schematic of ion gage test apparatus.

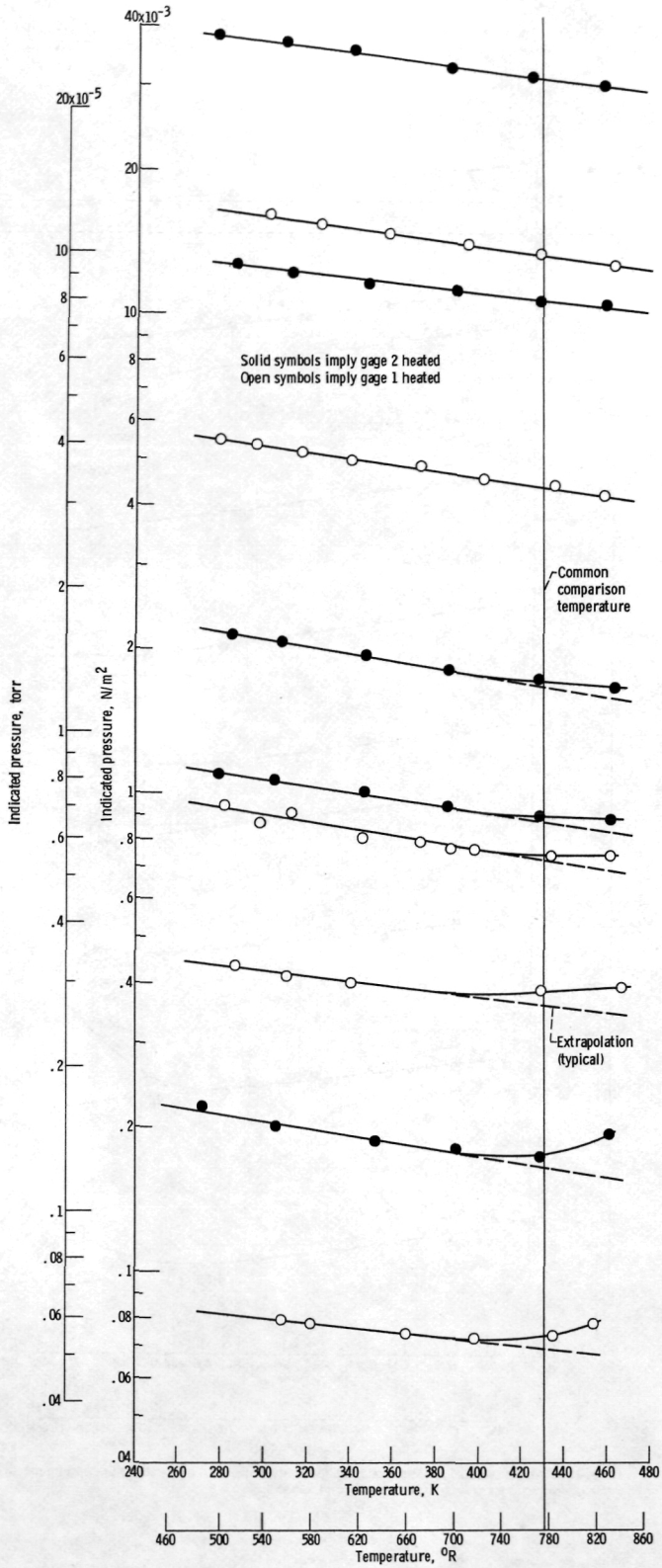


Figure 43. - Indicated vacuum pressure plotted against ion gage tubulation temperature; GN_2 background.

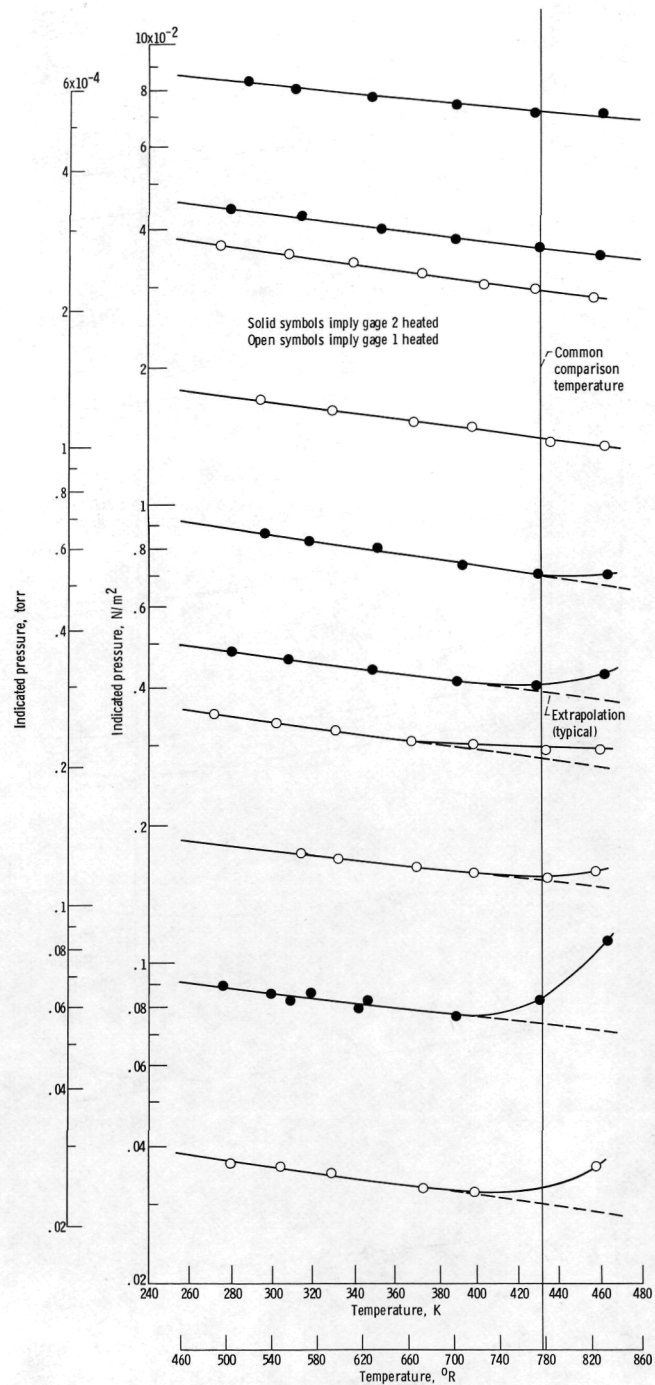


Figure 44. - Indicated vacuum pressure plotted against ion gage tubulation temperature; GHe background. (All data corrected for gaseous helium environment.)

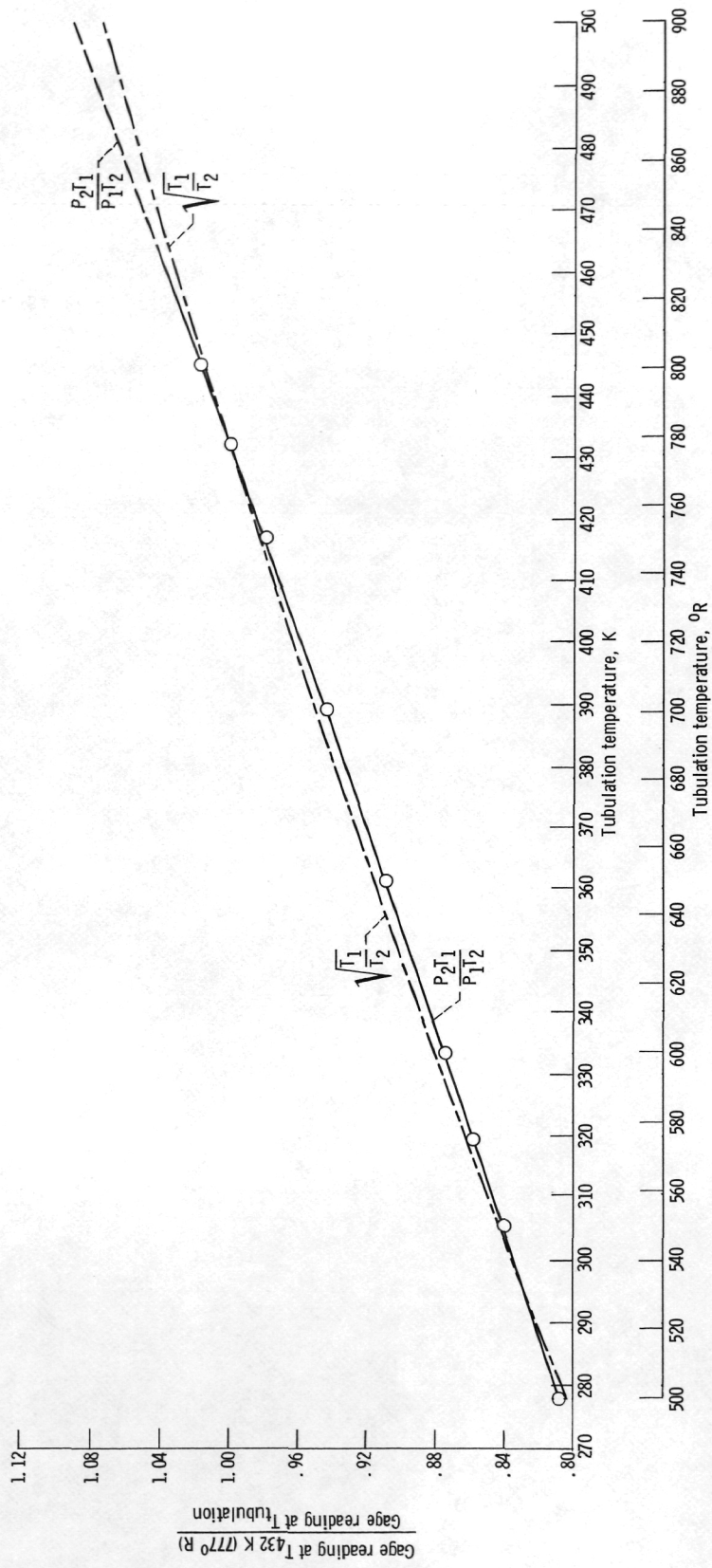


Figure 45. - Ion gage correction factor plotted against ion gage tubulation temperature.



(Section 158
Do Not Return)

"The aeronautical and space activities of the United States shall be conducted so as to contribute . . . to the expansion of human knowledge of phenomena in the atmosphere and space. The Administration shall provide for the widest practicable and appropriate dissemination of information concerning its activities and the results thereof."

—NATIONAL AERONAUTICS AND SPACE ACT OF 1958

NASA SCIENTIFIC AND TECHNICAL PUBLICATIONS

TECHNICAL REPORTS: Scientific and technical information considered important, complete, and a lasting contribution to existing knowledge.

TECHNICAL NOTES: Information less broad in scope but nevertheless of importance as a contribution to existing knowledge.

TECHNICAL MEMORANDUMS: Information receiving limited distribution because of preliminary data, security classification, or other reasons. Also includes conference proceedings with either limited or unlimited distribution.

CONTRACTOR REPORTS: Scientific and technical information generated under a NASA contract or grant and considered an important contribution to existing knowledge.

TECHNICAL TRANSLATIONS: Information published in a foreign language considered to merit NASA distribution in English.

SPECIAL PUBLICATIONS: Information derived from or of value to NASA activities. Publications include final reports of major projects, monographs, data compilations, handbooks, sourcebooks, and special bibliographies.

TECHNOLOGY UTILIZATION PUBLICATIONS: Information on technology used by NASA that may be of particular interest in commercial and other non-aerospace applications. Publications include Tech Briefs, Technology Utilization Reports and Technology Surveys.

Details on the availability of these publications may be obtained from:

SCIENTIFIC AND TECHNICAL INFORMATION OFFICE

**NATIONAL AERONAUTICS AND SPACE ADMINISTRATION
Washington, D.C. 20546**